JOURNAL OF PETROLOGY

Journal of Petrology, 2015, Vol. 56, No. 1, 193–226
doi: 10.1093/petrology/egu075
Original Article

OXFORD

Petrogenesis of the Rifted Southern Victoria Land Lithospheric Mantle, Antarctica, Inferred from Petrography, Geochemistry, Thermobarometry and Oxybarometry of Peridotite and Pyroxenite Xenoliths from the Mount Morning Eruptive Centre

Adam P. Martin[1]*, Richard C. Price[2], Alan F. Cooper[1] and Catherine A. McCammon[3]

[1]Department of Geology, University of Otago, PO Box 56, Dunedin, New Zealand, [2]Science and Engineering, University of Waikato, Hamilton, New Zealand and [3]Bayerisches Geoinstitut, University of Bayreuth, 95440 Bayreuth, Germany

*Corresponding author. Present address: GNS Science, Private Bag 1930, Dunedin, New Zealand. Telephone: (+64) 3 4799683. E-mail: adammartin2000@yahoo.com

Received April 15, 2014; Accepted December 9, 2014

ABSTRACT

The lithospheric mantle beneath West Antarctica has been characterized using petrology, whole-rock and mineral major element geochemistry, whole-rock trace element chemistry and Mössbauer spectroscopy data obtained on a suite of peridotite (lherzolite and harzburgite) and pyroxenite xenoliths from the Mount Morning eruptive centre, Southern Victoria Land. The timing of pyroxenite formation in Victoria Land overlaps with subduction of the Palaeo-Pacific plate beneath the Gondwana margin and pyroxenite is likely to have formed when fluids derived from, or modified by, melting of the subducting, eclogitic, oceanic crustal plate percolated through peridotite of the lithospheric mantle. Subsequent melting of lithospheric pyroxenite veins similar to those represented in the Mount Morning xenolith suite has contributed to the enriched trace element (and isotope) signatures seen in Cenozoic volcanic rocks from Mount Morning, elsewhere in Victoria Land and Zealandia. In general, the harzburgite xenoliths reflect between 20 and 30% melt depletion. Their depleted element budgets are consistent with Archaean cratonization ages and they have mantle-normalized trace element patterns comparable with typical subcontinental lithospheric mantle. The spinel lherzolite mineral data suggest a similar amount of depletion to that recorded in the harzburgites (20–30%), whereas plagioclase lherzolite mineral data suggest $<$15% melt depletion. The lherzolite (spinel and plagioclase) xenolith whole-rocks have compositions indicating $<$20% melt depletion, consistent with Proterozoic to Phanerozoic cratonization ages, and have mantle-normalized trace element patterns comparable with typical depleted mid-ocean ridge mantle. All peridotite xenoliths have undergone a number of melt–rock reaction events. Melting took place mainly in the spinel peridotite stability field, but one plagioclase peridotite group containing high-sodium clinopyroxenes is best modelled by melting in the garnet field. Median oxygen fugacity estimates based on Mössbauer spectroscopy measurements of spinel and pyroxene for spinel-facies conditions in the rifted Antarctic lithosphere are –0·6 Δlog fO_2 at Mount Morning and –1·0 $\pm$ 0·1 (1σ) Δlog fO_2 for all of Victoria Land, relative to the fayalite–magnetite–quartz buffer.

These values are in good agreement with a calculated global median value of –0·9 ± 0·1 (1σ) Δlog fO_2 for mantle spinel-facies rocks from continental rift systems.

Key words: lithospheric mantle; oxygen fugacity; pyroxenite; spinel peridotite; eclogite

INTRODUCTION

The West Antarctic rift system is an example of continental rifting comparable in scale with the southwestern US Basin and Range province or the East African Rift System. In Victoria Land, alkaline magmas of the Cenozoic McMurdo Volcanic Group have erupted discontinuously along the western edge of the rift system between Cape Adare in the north and Mount Early in the south (Fig. 1a and b). Numerous peridotite and pyroxenite xenoliths have been entrained during the ascent of the McMurdo Volcanic Group magmas, allowing direct study of the shallow Antarctic lithospheric mantle. The occurrence of mantle xenoliths in volcanic rocks from Southern Victoria Land has been extensively documented (Prior, 1902, 1907; Thomson, 1916; Smith, 1954; Kyle *et al.*, 1987). In particular, detailed studies have been made of pyroxenite xenoliths from Foster Crater (Fig. 1c), with petrographic, mineral and bulk-rock chemistry and some isotopic data reported in several publications (Gamble & Kyle, 1987; Gamble *et al.*, 1988; McGibbon, 1991). Potassium metasomatism, melt generation and infiltration and dynamic recrystallization processes have been identified in the Foster Crater xenolith suite (Gamble *et al.*, 1988), and the dominant glimmerite and phlogopite-rich clinopyroxenite rock types have been noted as atypical for the region (McGibbon, 1991). McGibbon (1991) obtained a 439·2 ± 14·5 Ma Rb–Sr isochron using whole-rock and mica data from Foster Crater. Some preliminary studies of mineral chemistry or mineral isotopes have been carried out on peridotite xenoliths from other localities within the Erebus volcanic province (e.g. McGibbon, 1991; Warner & Wasilewski, 1995; Cooper *et al.*, 2007). Amphibole has been noted as an integral component of xenoliths at White Island (Cooper *et al.*, 2007), Pipecleaner Glacier (Martin *et al.*, 2014) and Foster Crater (e.g. Gamble *et al.*, 1988) but is uncommon in the Mount Morning xenoliths (Martin *et al.*, 2014). Martin *et al.* (2013) reported whole-rock chemistry and Sr–Nd–Pb isotope data for peridotite and pyroxenite xenoliths and volcanic rocks from Mount Morning, and Martin *et al.* (2014) presented data from plagioclase-bearing spinel lherzolite from three localities across the Erebus volcanic province. Based mainly on the study of the volcanic rocks it has been argued that the Erebus volcanic province mantle is heterogeneous on a sub-kilometre scale, with a depleted mantle component refertilized by a mix of HIMU-like and enriched components (Cooper *et al.*, 2007; Sims *et al.*, 2008; Martin *et al.*, 2013). Peridotite and pyroxenite xenoliths from several localities in the Melbourne volcanic province of Northern Victoria Land have been studied in detail, revealing a complex history of partial melting and metasomatism, resulting in a heterogeneous mantle (Wörner *et al.*, 1989; Zipfel & Wörner, 1992; Wörner & Zipfel, 1996; Wörner, 1999; Coltorti *et al.*, 2004; Perinelli *et al.*, 2006, 2008; Nardini *et al.*, 2009; Armienti & Perinelli, 2010; Melchiorre *et al.*, 2011; Perinelli *et al.*, 2011; Bonadiman *et al.*, 2014). Oxygen fugacity has been calculated for Northern Victoria Land mantle xenoliths using Mössbauer spectroscopic measurements on spinel and is estimated to be between –0·2 and –2·5 Δlog fO_2 (Perinelli *et al.*, 2012; Bonadiman *et al.*, 2014). Recently, evidence has been presented for a component of eclogite in the mantle beneath Northern Victoria Land (Melchiorre *et al.*, 2011). Building on initial work from Mount Morning (Sullivan, 2006; Martin, 2009; Martin *et al.*, 2013), this study reports the petrography, whole-rock and mineral chemistry, geothermobarometry and oxybarometry of a suite of 40 peridotite and pyroxenite xenoliths collected from Mount Morning eruptive centre in the Erebus volcanic province, with the aim of characterizing the mantle lithosphere beneath Mount Morning and discussing lithospheric mantle evolution along the Victoria Land segment of the West Antarctic rift system.

GEOLOGICAL SETTING

Mount Morning is an eruptive centre in McMurdo Sound that has been active since at least 18·7 Ma and probably since *c.* 24 Ma based on distal tephra deposits recovered in drill cores (Martin *et al.*, 2010; Di Roberto *et al.*, 2012; Nyland *et al.*, 2013). It is located within a recently active (post 3·9 Ma) portion of the West Antarctic rift system fault array (Martin & Cooper, 2010) on crust estimated to be around 18 km thick (McGuiness *et al.*, 1985; Bannister *et al.*, 2003). The xenoliths ($\leq$50 cm) are found exclusively in Quaternary age rocks of the strongly alkalic, nepheline-normative Riviera Ridge Lineage (Martin *et al.*, 2013) at Mount Morning and are unweathered, typically free of modal metasomatism and have sharp contacts with the host basalt. The locality of each sample is given in Supplementary Data Appendix 1, together with the typical bulk-rock composition of the host of the mantle xenoliths (supplementary data are available for downloading at http://www.petrology.oxfordjournals.org). The Mount Morning volcanic rock major and trace element and isotopic chemistry was described in detail by Martin *et al.* (2013), who concluded that the eruptive rocks are part of a much wider Cenozoic diffuse alkaline magmatic province (DAMP) that incorporates Victoria Land, Marie Byrd Land, Zealandia and parts of eastern Australia

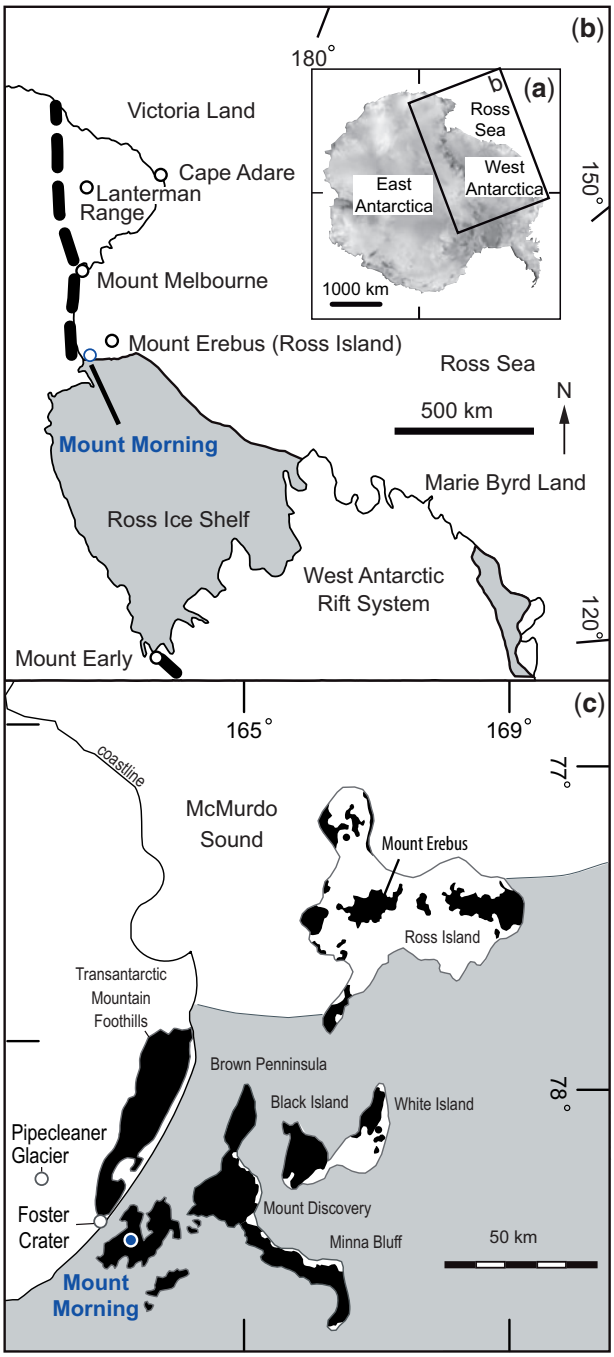

Fig. 1. Location map of Mount Morning and key locations referenced in this study. (a) Map of Antarctica. (b) Map of Victoria Land. The bold dashed line approximates the position of the Transantarctic Mountains. Northern Victoria Land includes Mount Melbourne and Cape Adare. Southern Victoria Land includes Mount Erebus and Mount Morning. (c) Map of Erebus volcanic province rocks (black fill) in Southern Victoria Land (Kyle, 1990*a*; Cox *et al.*, 2012). Grey shading denotes the approximate extent of multi-year ice.

(Finn *et al.*, 2005). Rocks of the McMurdo Volcanic Group may be subdivided into the volcanic provinces of Erebus (Southern Victoria Land) and Melbourne and Hallett (Northern Victoria Land; Kyle, 1990*b*). Rifting commenced in the Victoria Land region *c.* 95 Myr ago (Ritzwoller *et al.*, 2001) and the Antarctic plate has remained effectively stationary since *c.* 80 Ma (Grindley *et al.*, 1981). The Transantarctic Mountains lie to the east of, and form part of the basement to, Mount Morning (Martin, 2009; Cox *et al.*, 2012; Martin *et al.*, 2015). Basement lithologies within the Transantarctic Mountains comprise Neoproterozoic to Cambrian Ross Orogen metasedimentary rocks that are cross-cut by arc-related Neoproterozoic to Ordovician plutonic rocks associated with subduction along the Gondwana margin (Borg & DePaolo, 1991; Allibone & Wysoczanski, 2002).

ANALYTICAL METHODS

Whole-rock chemistry

Bulk-rock samples were analysed by X-ray fluorescence (XRF) at the University of Otago, New Zealand, on a Philips PW2400 XRF spectrometer, following analytical procedures modified from Norrish & Chappell (1977) and using the SuperQ qualitative software control program (3rd edition). Samples were crushed using a TEMA swing mill fitted with a WC head. Contamination of trace elements during the crushing process is restricted to W and Co (Martin *et al.*, 2013). The lower limit of detection is better than 0·004 wt % for Al_2O_3. Loss on ignition was determined at 1100°C. For trace element measurements, 100 mg of sample were digested with a HF–HNO_3 mixture in a high-pressure bomb at 185°C for 24 h. Solutions were evaporated, then redissolved in HCl for 24 h, dried down and refluxed twice with concentrated HNO_3, then dissolved overnight in sealed vessels with 3N HNO_3. Solutions were transferred to transparent polycarbonate tubes, diluted with water and centrifuged, then inspected for undissolved fluorides. An aliquot of the solution was further diluted with a 1·8% HNO_3 solution (containing an internal standard mixture) to give a total dilution factor of between 1300 and 1800. Samples were analysed by inductively coupled plasma source mass spectrometry (ICP-MS) at the School of Earth Sciences, University of Melbourne on an Agilent 7700x. The instrument was tuned to give Ce oxide levels of $<1\%$. Four replicates of 100 scans per replicate were measured for each isotope. Dwell times were 10 ms, except for Be, Nb, Zr, Mo, Cd, In, Sb, Hf, Ta, W, Tl, Bi, Th and U, which were 30 ms. Long sample wash-out times of 6 min with solutions of 0·5% Triton X-100, 0·025% HF in 5% HNO_3 and 2% HNO_3 and long sample uptake times of 120 s were used. Digests of USGS standards PCC-1, DTS-1 and BIR-1 were run as unknowns to check the long-term accuracy and reproducibility (the standard data are given in the Supplementary Data Appendix 1). BIR-1 was used as a drift monitor and the calibration standards were analysed at the end of the run. Analytical and drift correction procedures have been comprehensively described by Eggins *et al.* (1997). The method uses a natural rock standard for calibration, internal drift correction using multi-internal standards (in this case ^{6}Li, Rh, Re and

^{235}U), external drift monitors and aggressive washout procedures. Differences from the Eggins *et al.* (1997) method are as follows: (1) ^{84}Sr, ^{147}Sm, Tm, In and Bi were not used as internal standards; (2) two digestions of the USGS standard W-2 were used for instrument calibration (the standard data are given in the Supplementary Data Appendix 1). The preferred concentrations used for W-2 were derived by analysing it against synthetic standards and a literature survey of isotope dilution analyses (Kamber *et al.*, 2003, 2005; Babechuk *et al.*, 2010). Because only a single calibration standard is used, data can be easily normalized to other sets of preferred values for standards.

Mineral chemistry

Major element mineral chemistry was determined using two JEOL microprobes, both operated with accelerating voltage 15 kV, current 1 μA, and beam diameter 20 μm. A JEOL JXA-8200 was utilized at the Bayerisches Geoinstitut, Bayreuth, Germany, and a JEOL JXA-8600 at the University of Otago, Dunedin, New Zealand. For both instruments, the analyses were performed in either wavelength-dispersive mode or energy-dispersive mode. A standard ZAF correction was applied to all data.

Mössbauer spectroscopy

The $Fe^{3+}/\sum Fe$ measurements were obtained by ^{57}Fe Mössbauer spectroscopy at the Bayerisches Geoinstitut on mineral separates of spinel, clinopyroxene and orthopyroxene hand-picked under a binocular microscope. Pyroxene crystals were crushed in an agate mortar and mounted in an acrylic holder with a 12 mm diameter and analysed using a conventional Mössbauer source (nominal 1·85 GBq ^{57}Co source in a 6 μm Rh matrix). Single crystals of spinel were chosen that were free of alteration and accessory minerals and then analysed using a point source (nominal 370 MBq ^{57}Co high specific activity source in a 12 μm Rh matrix). Dimensionless absorber thicknesses were between four and six (10–15 mg Fe cm^{-2}). Grains were mounted between pieces of cellophane tape and masked with 25 μm thick Ta foil drilled with a 500 μm hole. Mössbauer spectra were recorded at room temperature (293 K) in transmission mode on a constant acceleration Mössbauer spectrometer. The velocity scale was calibrated relative to 25 μm α-Fe foil using the positions certified for National Bureau of Standards (now called the National Institute of Standards and Technology) standard reference material no. 1541; line widths of 0·36 mm s^{-1} (point source) and 0·28 mm s^{-1} (conventional source) for the outer lines of α-Fe were obtained. Mirror image spectra were collected over 512 channels with a velocity range of ±5 mm s^{-1}. The spectra were fitted with the NORMOS software package (distributed by Wissenschaftliche Elektronik GmbH, Germany). A more in-depth description of the point source method has been given by McCammon *et al.* (1991) and McCammon (1994).

RESULTS

The mineral mode and texture of the Mount Morning mantle xenoliths are reported in Table 1 and shown in Figs 2 and 3. Whole-rock and mineral chemistry data (major and trace elements) are reported in Tables 2–4 and Supplementary Data Appendix 1. Geothermobarometry and oxygen fugacity results are reported in Table 5 and the Mössbauer spectroscopy hyperfine parameters are reported in Table 6.

Sample description and petrography

Mantle xenolith-bearing igneous rocks are very common at Mount Morning. In some cases, xenoliths form a significant component (≤7%) of the outcrop (Martin, 2009; Fig. 3a). The xenolith suite has been divided into Group I peridotite and Group II pyroxenite subtypes (Fig. 2; Table 1), with the Group II pyroxenites further subdivided into Cr-diopside series and Al-augite series (Wilshire & Shervais, 1975; Frey & Prinz, 1978). The peridotite xenoliths include a range of spinel peridotite (dunite, harzburgite, lherzolite) xenoliths and plagioclase-bearing spinel lherzolite (plagioclase lherzolite hereafter) xenoliths. The latter have been described in detail by Martin *et al.* (2014). All classifications are based upon modal mineralogy determined by counting 300 points in thin section (Martin, 2009; Fig. 2). The pyroxenite (*sensu lato* after Upton *et al.*, 2011) xenoliths include wehrlite, olivine clinopyroxenite, clinopyroxenite and rare phlogopite-bearing clinopyroxenite of the Al-augite series, and plagioclase-bearing websterite and olivine websterite, websterite and orthopyroxenite subtypes of the Cr-diopside series. An example of a composite xenolith, containing a pyroxenite band within a peridotite host, was also included (OU78 711, Fig. 3b). Garnet is never observed in the Mount Morning mantle xenoliths. Typically, peridotite abundance dominates over pyroxenite abundance (4:1; Martin, 2009), with lherzolite the most common peridotite subtype. Wehrlite and olivine clinopyroxenite xenoliths are the most common pyroxenite subtypes at Mount Morning, followed closely by websterite and olivine websterite subtypes. Clinopyroxenite was collected from only a single locality; of those collected only a single specimen was found to be phlogopite-bearing. A summary of the percentage of rock types collected is shown in Supplementary Data Fig. A1. For comparison, a norite crustal xenolith (OU78 688) collected from Mount Morning and described by Martin *et al.* (2013) is also discussed in the text and data for this sample are included in figures.

The texture of the Cr-diopside series pyroxenite xenoliths is metamorphic (Harte, 1977); uniform, equant and granuloblastic (Table 1). The Al-augite series pyroxenite xenoliths have igneous textures (Pike & Schwarzman, 1977) and are either equigranular or coarsely porphyritic. The peridotite xenoliths have metamorphic textures with tabular granuloblastic and porphyroclastic textures being most common and

Table 1. Mineral mode and texture of Mount Morning xenoliths

Specimen no.	Field ID	Rock name	Xenolith type	Series	Texture	Ol	Cpx	Opx	Sp	Pl
OU78443	23707	Dunite	I	—	E.G.	86	3	7	4	—
OU78448	23719	Dunite	I	—	C.	93	3	3	1	—
OU78473	LZL01	Harz	I	—	T. G.	73	4	22	1	—
OU78477	LZL05	Harz	I	—	P.	77	3	19	1	—
OU78479	LZL07	Harz	I	—	P.	75	3	21	1	—
OU78481	LZL09	Harz	I	—	T.G.	71	4	23	2	—
OU78515	LL03	Harz	I	—	T.G.	78	1	20	1	—
OU78518	LL07	Harz	I	—	T.G.	79	1	19	1	—
OU78522	LL11	Harz	I	—	T.G.	74	4	22	0·2	—
OU78523	LL12	Harz	I	—	T.G.	73	4	23	0·1	—
OU78527	LL16	Harz	I	—	T.G.	75	4	21	0·1	—
OU78441	23702	Lz	I	—	E.G.	52	12	33	3	—
OU78476	LZL04	Lz	I	—	T.G.	47	13	34	6	—
OU78482	LZL10	Lz	I	—	P.	65	8	24	3	—
OU78513	LL01	Lz	I	—	T.G.	66	7	25	2	—
OU78514	LL02	Lz	I	—	T.G.	59	9	31	1	—
OU78516	LL04	Lz	I	—	T.G.	63	10	25	2	—
OU78517	LL05	Lz	I	—	T.G.	67	9	23	1	—
OU78521	LL10	Lz	I	—	T.G.	57	11	32	0·1	—
OU78524	LL13	Lz	I	—	T.G.	57	11	32	1	—
OU78525	LL14	Lz	I	—	T.G.	59	9	32	0·1	—
OU78703	LZM01	Lz	I	—	P.	63	6	28	3	
OU78475	LZL03	Pl Lz	I	—	P.	67	10	14	1	8
OU78478	LZL06	Pl Lz	I	—	T.G.	60	12	23	2	3
OU78480	LZL08	Pl Lz	I	—	P.	72	7	17	1	3
OU78519	LL08	Pl Lz	I	—	T.G.	69	6	21	1	3
OU78520	LL09	Pl Lz	I	—	T.G.	72	8	11	1	8
OU78526	LL15	Pl Lz	I	—	T.G.	62	12	22	3	1
OU78474	LZL02	Ortho	II	Cr-diopside	E.G.	5	3	91	1	—
OU78702	LZ01	Pl Web	II	Cr-diopside	E.G.	17	27	48	2	6
OU78465	CD06	Pl Web	II	Cr-diopside	E.G.	—	48	39	10	3
OU78461	CD02	Web	II	Cr-diopside	E.G.	3	70	26	1	—
OU78462	CD03	Web	II	Cr-diopside	E.G.	2	87	11	0·0	—
OU78483	WZ01	Wehr	II	Al-augite	E.	53	44	3	—	—
OU78484	WZ02	Wehr	II	Al-augite	E.	56	40	4	—	—
OU78487	WZ08	Ol Pyrox	II	Al-augite	E.	35	62	3	—	—
OU78488	WZ14	Ol Pyrox	II	Al-augite	E.	28	69	3	—	—
OU78691	435B-I	Clino	II	Al-augite	C.P.	2	94	4	—	—
OU78692	435B-II	Clino	II	Al-augite	C.P.	3	95	2	—	—
OU78693	435B-III	Phl Clino	II	Al-augite	C.P.	2	96	2	—	—

Ol, olivine; Cpx, clinopyroxene; Opx, orthopyroxene; Sp, spinel; Harz, harzburgite; Lz, lherzolite; Pl Lz, plagioclase-bearing spinel lherzolite; Ortho, orthopyroxenite; Pl Web, plagioclase websterite; Web, websterite; Wehr, wehrlite; Ol Pyrox, olivine pyroxenite; Clino, clinopyroxenite; Phl Clino, phlogopite clinopyroxenite; E.G., equant granuloblastic; C., coarse; T.G., tabular granuloblastic; P., porphyroclastic; E., equigranular; C.P., coarsely porphyritic. Mineral mode was determined by counting 300 points in each thin section (Martin, 2009).

examples of coarse or equant granuloblastic textures being rare (Table 1). For each rock type, hand-specimen photographs and representative thin-section fields of view are shown in Supplementary Data Fig. A2; additional rock and mineral texture photographs are shown in Fig. A3.

Peridotite

Dunite. Dunites are yellow–green in hand specimen ($\leq$40 cm) and dominated by modal olivine. Orthopyroxene is rare to absent and clinopyroxene is rare. Spinel is observed in both specimens (OU78 443 and 448). The two specimens represent end-member textures, with OU78 448 having a coarse texture and specimen OU78 443 having an equant granuloblastic texture. In thin section olivine porphyroclasts $\leq$5 mm in diameter are set in a matrix of neoblasts typically 0·5 mm across. Olivine is in many cases deformed by weak kink bands. Fluid inclusion trails are common in porphyroclasts and the trails, which are a maximum of 0·05 mm across, are defined by a population of much smaller inclusions (Fig. 3c). Orthopyroxene occurs rarely as weakly kink-banded porphyroclasts $\leq$4 mm in diameter with neoblasts $\sim$0·50 mm in diameter. Clinopyroxene porphyroclasts are on average finer grained than the porphyroclasts of olivine, or the rare orthopyroxene, typically being between 2 and 3 mm, and they do not have kink bands or petrographically resolvable exsolution lamellae. Clinopyroxene neoblasts are $\leq$0·5 mm across. Spinel occurs as porphyroclasts up to 1 mm in diameter that are commonly observed overprinting the junction of several olivine grains.

Harzburgite. Harzburgite specimens, which are bright green in hand specimen, typically display a strongly deformed, tabular, granuloblastic texture with

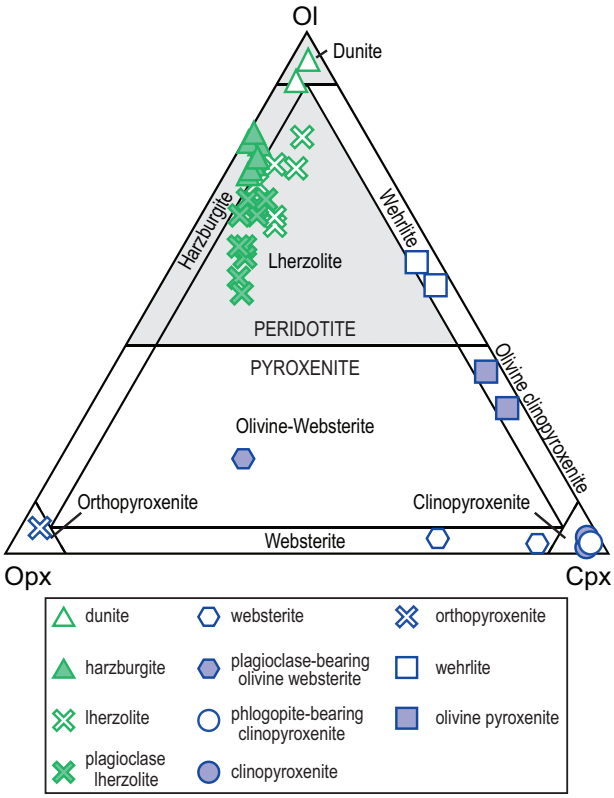

Fig. 2. Olivine–pyroxene ternary diagram plotting mineral mode from Table 1 for the mantle xenoliths.

olivine > orthopyroxene, <5% clinopyroxene and accessory spinel. Feldspar is never observed. In thin section olivine porphyroclasts are ≤4 mm and neoblasts are ~0·5 mm across. Strain features (such as kink banding) are either weakly displayed or absent and exsolution lamellae are not observed. Clinopyroxene occurs as both rare porphyroclasts (~2 mm) and more common neoblasts (0·5 mm); the porphyroclasts may display weak kink bands. In thin section, orthopyroxene is common as coarse porphyroclasts (≤6 mm), which show strongly developed kink banding and in the more highly deformed rocks are in places dislocated along fractures (Fig. 3d). The fractures are normal to the overall foliation of the rock, which is defined by subparallel alignment of the long axes of minerals. Exsolution lamellae of clinopyroxene (≤0·05 mm wide) are common in the orthopyroxene porphyroclasts (Fig. 3e). Orthopyroxene also occurs as neoblasts typically 0·5 mm in diameter and spinel is a common, if minor, phase with porphyroclasts being ≤2 mm across.

Lherzolite. In hand specimen lherzolites are bright green and free of weathering and alteration. Textures are either tabular granuloblastic or porphyroclastic, with only a single specimen (OU78 441) displaying an equant granuloblastic texture. In thin section olivine is observed as porphyroclasts (≤5 mm) and neoblasts (~0·5 mm) with the former frequently containing kink bands and inclusion trails <0·01 mm wide. Clinopyroxene occurs most commonly as neoblasts and more rarely as porphyroclasts. The latter are typically finer grained (2–3 mm across) than the olivine or orthopyroxene porphyroclasts. Rare clinopyroxene porphyroclasts are kink banded and exsolution lamellae of secondary clinopyroxene are observed in places. Clinopyroxene neoblasts occur in two forms: one forming triple-point junctions with surrounding grains, and the other infilling cracks in adjacent grains. Orthopyroxene is observed as porphyroclasts (≤5 mm) and as neoblasts (~0·5 mm). Orthopyroxene porphyroclasts commonly display weakly to strongly developed kink bands and are present in even the most strongly deformed rocks where other types of porphyroclast do not occur. Spinel occurs as porphyroclasts ≤4 mm in diameter; these are associated with granuloblastic-textured rocks in particular. Otherwise spinel may occur as anhedral or vermicular porphyroclasts (≤0·05 mm) in less deformed rocks. Where spinel occurs as porphyroclasts, it can also form rare oikocrysts, typically 3 mm in diameter, that poikiloblastically enclose chadocrysts of clinopyroxene (0·5 mm; Fig. 3f).

Plagioclase lherzolite. In several xenoliths from Mount Morning plagioclase coexists with the olivine + clinopyroxene + orthopyroxene + spinel. Plagioclase was identified only in thin section, and hand specimens of plagioclase lherzolite look identical to spinel lherzolite and display a similar range of textures. Plagioclase lherzolites are amongst the largest xenoliths collected from Mount Morning (up to 50 cm in diameter). In thin section plagioclase is observed only as neoblasts ≤0·3 mm, has a lath-like, or anhedral to subhedral habit, and is typically associated with spinel (Supplementary Data Fig. A3a and b). Triple-point junctions between plagioclase and the other minerals are typical, with both multiple and simple twinning observed. Olivine occurs as porphyroclasts (≤3 mm) and neoblasts (~0·2 mm). Clinopyroxene occurs as rare porphyroclasts up to 2 mm across and commonly as neoblasts, 0·2 mm in diameter. Undulose extinction, kink banding and fluid inclusion trails can be observed in the clinopyroxene porphyroclasts. Orthopyroxene occurs as porphyroclasts (≤4 mm) and neoblasts (~0·2 mm), with kink bands commonly present in the former. In thin section, spinel typically occurs as porphyroclasts (≤3 mm) and rarely as oikocrysts poikiloblastically enclosing chadocrysts of clinopyroxene. In the porphyroclastic textured xenoliths spinel porphyroclasts have a subrounded habit. In the more highly deformed, tabular granuloblastic xenoliths, the spinel porphyroclasts have in some cases a holly-leaf habit (Supplementary Data Fig. A3c) and are aligned subparallel to the other grains in the xenolith. Spinel is also observed as neoblasts up to 0·2 mm in diameter and rare carbonate grains are observed (Martin *et al.*, 2014).

Pyroxenite, Cr-diopside series

Websterite. The websterite xenoliths are dominated by clinopyroxene with subordinate orthopyroxene and

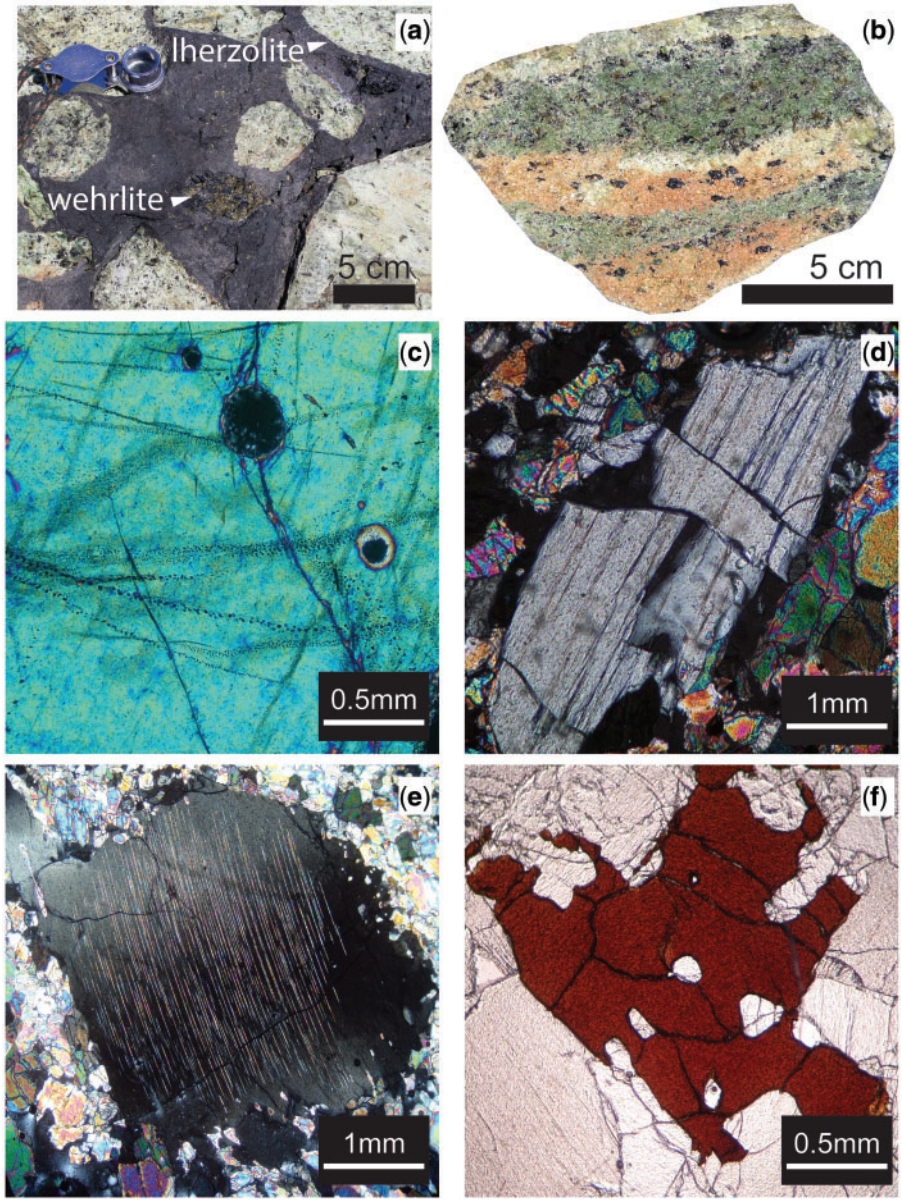

Fig. 3. Mantle xenolith petrography. (a) Photograph of peridotite and one wehrlite xenolith in outcrop. (b) Composite xenolith with a vein of websterite (dark green) in a host peridotite. (c) Fluid inclusion trails within olivine crystal in dunite. (d) Orthopyroxene crystal in harzburgite dislocated along fracture planes. (e) Exsolution lamellae of clinopyroxene within orthopyroxene in a harzburgite. (f) Spinel oikocrysts poikiloblastically enclosing chadocrysts of clinopyroxene in a lherzolite.

modally minor amounts of spinel. In hand specimen the clinopyroxene gives the rock an iridescent green colour. In thin section, clinopyroxene is observed as porphyroclasts ($\leq$2 mm) and neoblasts ($\leq$0·5 mm) and some porphyroclasts display weak kink banding or undulose extinction. Orthopyroxene occurs as porphyroclasts ($\leq$3 mm on the long axis) and as neoblasts ($\sim$0·5 mm), with the former commonly displaying undulose extinction, weakly to moderately developed kink banding and exsolution lamellae of clinopyroxene. Spinel is a modally minor phase ($<<$1%) occurring as small crystals ($<$0·1 mm) along grain boundaries.

Orthopyroxenite. Hand specimens ($\leq$200 mm) of orthopyroxenite are yellow–green in colour and contain, in addition to orthopyroxene, modally small amounts of olivine (5%), clinopyroxene (1–3%) and spinel ($<$1 %). In thin section, orthopyroxene is observed as porphyroclasts with undulose extinction, of $\leq$5 mm, and as neoblasts, typically 0·5 mm in diameter. Exsolution lamellae of clinopyroxene are common in the orthopyroxene porphyroclasts and the grains are full of inclusions that give them a 'dirty' appearance in plane-polarized light. Clinopyroxene neoblasts, between 0·3 and 0·5 mm in diameter, form interstitially between the orthopyroxene porphyroclasts, and spinel neoblasts up to 1 mm across are observed in thin section and hand specimen. There are triple-point junctions, and sharp curvi-planar boundaries between all phases.

Table 2. Whole-rock chemistry of Mount Morning peridotite xenoliths

Field no.:	23707	23719	LZL01	LZL05	LZL07	LZL09	LL03	LL07	LL11	LL12	LL16	23702	LZL04	LZL10	LL01
OU no.:	78443	78448	78473	78477	78479	78481	78515	78518	78522	78523	78527	78441	78476	78482	78513
Mg#:	87·6	90·9	91·4	91·3	91·8	90·9	91·8	91·8	91·6	91·5	91·7	89·7	89·5	90·1	90·9
Cr#:	8·3	46·0	7·1	12·6	14·3	10·7	19·8	22·6	14·4	14·0	13·4	5·5	5·5	0·2	11·0
wt %															
SiO_2	40·14	41·51	44·49	43·87	44·00	44·11	44·04	43·76	44·09	44·23	43·74	44·90	45·12	44·15	44·49
TiO_2	0·17	0·02	0·02	0·02	0·02	0·04	0·02	0·02	0·02	0·02	0·02	0·12	0·11	0·07	0·04
Al_2O_3	0·91	0·34	1·17	1·05	1·08	1·63	0·59	0·59	1·17	1·22	1·17	3·30	3·45	2·12	1·76
FeO^T	11·45	8·50	7·50	7·68	7·26	7·91	7·37	7·33	7·32	7·43	7·24	7·95	7·84	8·24	7·67
MnO	0·16	0·13	0·12	0·12	0·11	0·12	0·12	0·12	0·12	0·12	0·12	0·13	0·13	0·13	0·12
MgO	45·23	47·85	44·60	45·46	45·64	44·16	46·41	46·37	44·70	44·79	45·13	38·81	37·61	41·90	42·05
CaO	0·99	0·68	1·06	0·92	1·04	1·13	0·48	0·50	1·16	1·03	1·00	3·08	3·32	2·34	1·68
Na_2O	0·01	0·09	0·02	0·00	0·05	0·05	0·05	0·01	0·04	0·08	0·06	0·26	0·46	0·14	0·07
K_2O	0·05	0·02	0·02	0·01	0·01	0·02	0·02	0·02	0·04	0·02	0·03	0·03	0·07	0·06	0·05
P_2O_5	0·04	0·01	0·01	0·01	0·01	0·01	0·01	0·01	0·01	0·01	0·01	0·01	0·01	0·01	0·01
Cr_2O_3	0·13	0·43	0·13	0·23	0·27	0·29	0·22	0·26	0·29	0·30	0·27	0·29	0·30	0·01	0·32
NiO	0·23	0·23	0·01	0·01	0·24	0·25	0·01	0·25	0·25	0·24	0·23	0·20	0·02	0·00	0·23
LOI %	–0·50	–0·40	–0·09	–0·30	–0·34	–0·32	–0·24	–0·19	–0·06	–0·12	0·36	0·26	0·58	–0·15	0·52
Total	99·0	99·4	99·1	99·1	99·4	99·4	99·1	99·1	99·1	99·4	99·4	99·3	99·0	99·0	99·0
ppb															
Li	n.d.	3238	1357	1773	n.d.	1676	1378	1413	1469	1304	1396	1899	1690	1625	1461
Be	n.d.	2·60	13·2	12·8	n.d.	15·7	14·5	20·8	10·0	5·50	9·50	25·4	27·0	18·3	9·60
Sc	6505	3912	9307	7522	8179	9673	6805	6812	8188	8841	8606	13571	15844	12488	10814
Ti	n.d.	64872	89686	87222	n.d.	219423	54125	66391	97260	83843	89237	376850	670169	359576	180307
V	27885	19878	39321	29690	34101	39646	24563	25800	37283	38527	35821	68663	75528	54224	47903
Cr	1265812	4375568	3080131	2665074	2765466	2269376	2357110	2576743	2887910	3471630	2946031	3176976	2667297	2350528	3046979
Co	158495	155928	134317	137644	126212	137897	129731	133767	127243	123869	122829	121338	117597	135377	138923
Ni	2440088	2152334	2219494	2264170	2441500	2232563	2343632	2391144	2223408	2193088	2230944	1865312	1766198	2028061	2049347
Cu	n.d.	3095	9916	7368	n.d.	10687	6994	7413	10733	18024	14749	14856	29763	15399	14064
Zn	n.d.	51624	45780	45948	n.d.	45108	42322	43690	43701	46373	44515	47646	45192	47369	44611
Ga	1743	589	1018	920	1007	1217	444	475	927	1026	868	2237	2883	1852	1387
Rb	1109	366	283	161	211	162	177	194	563	248	567	129	1286	304	755
Sr	34962	2182	1391	2963	1317	3767	1603	1604	1966	816	2515	8200	9337	5725	2959
Y	1307	138	308	367	350	865	184	202	358	289	320	1676	3425	1826	717·1
Zr	9632	181	1204	1090	689	2532	823	922	775	1490	1184	2864	6164	3522	3009
Nb	2550	36·0	257	128	105	171	266	387	201	298	258	128	505	192	92·5
Cd	n.d.	35·1	13·8	11·3	n.d.	14·3	9·60	9·30	11·7	12·3	13·9	24·1	30·7	21·6	16·2
In	n.d.	3·30	5·40	4·80	n.d.	7·00	3·00	3·20	5·00	4·80	4·50	10·0	13·0	10·6	6·30
Sn	n.d.	53·6	130	64·3	n.d.	42·0	BDL	43·4	10·7	13·9	24·7	4·60	93·1	75·9	26·6
Sb	n.d.	4·50	9·00	1·10	n.d.	8·20	1·60	1·70	7·20	7·40	13·4	0·10	20·7	5·50	5·20
Cs	n.d.	2·70	1·80	1·50	n.d.	0·90	2·10	1·60	4·40	1·80	3·80	1·90	5·60	1·90	4·90
Ba	14632	961	851	138	40·0	132	288	207	392	112	286	450	259	150	218
La	1813	40·1	108	48·3	44·8	72·5	34·0	39·5	37·6	27·7	98·1	561	75·6	69·4	75·8
Ce	3104	95·7	214	117	95·1	210	70·3	81·7	100	73·9	190	1750	301	254	223
Pr	443	14·5	24·3	19·1	27·2	32·5	11·9	13·3	16·7	8·40	21·8	267	69·8	49·3	34·1
Nd	1810	67·4	91·6	103	109	162	77·4	85·3	90·9	39·4	88·6	1096	471	296	166
Sm	374	19·3	18·7	32·0	38·6	55·2	34·5	37·2	31·6	13·4	23·8	215	232	125	48·7
Eu	121	5·90	5·90	12·1	18·4	22·4	13·2	14·2	10·9	4·70	8·10	73·8	98·9	51·3	17·4
Gd	335	21·5	23·9	42·8	48·5	86·9	47·3	51·8	42·0	21·3	30·3	231	392	204	67·5
Tb	51·5	3·60	5·20	7·90	15·8	17·8	7·40	8·20	7·90	4·60	6·10	40·8	78·4	40·1	13·8
Dy	264	23·3	40·2	54·5	62·2	133	37·8	41·7	54·3	38·4	45·6	273	554	287	102
Ho	52·5	5·20	11·4	13·5	20·2	32·5	6·80	7·50	13·6	10·4	11·7	63·3	129	68·8	26·6
Er	145	16·0	40·7	44·6	55·8	103	16·7	18·7	43·2	38·3	40·0	191	389	211	88·9
Tm	21·0	2·70	7·50	7·50	14·6	17·0	2·40	2·70	7·20	6·90	7·00	29·5	60·3	34·0	14·9
Yb	116	19·5	58·3	55·8	59·8	121	17·5	18·6	53·7	53·9	52·9	199	394	231	109
Lu	19·4	3·50	10·5	9·50	17·3	20·0	3·10	3·40	9·20	9·80	9·60	31·5	61·2	37·6	18·2
Hf	200	5·30	19·4	20·0	15·3	50·1	13·0	16·1	17·4	21·4	21·0	77·2	164	82·4	74·5
Ta	200	147	163	142	168	152	105	122	121	87·2	75·8	127	126	160	239
W	n.d.	218686	228647	235484	n.d.	240839	161342	190031	178182	136308	112300	191536	192939	254826	359702
Tl	n.d.	1·80	0·40	0·30	n.d.	0·20	0·40	0·20	0·70	0·20	0·70	2·40	1·30	0·40	1·40
Pb	201	28·4	45·6	22·0	57·7	29·0	36·4	29·0	58·7	23·0	78·2	85·3	119	43·1	67·7
Bi	n.d.	0·70	0·60	0·20	n.d.	0·40	0·50	0·30	0·70	0·90	0·90	2·20	2·10	0·70	1·30
Th	202	3·30	17·4	6·00	13·8	11·0	8·50	10·9	7·20	9·50	10·8	18·5	77·3	3·80	9·20
U	61·5	2·10	20·1	13·7	12·9	11·8	27·8	22·2	23·6	10·8	11·4	9·40	69·3	28·4	20·8

(continued)

Table 2. Continued

Field no.:	LL02	LL04	LL05	LL10	LL13	LL14	LZM01	LZL03	LZL06	LZL08	LL08	LL09	LL15
OU no.:	78514	78516	78517	78521	78524	78525	78703	78475	78478	78480	78519	78520	78526
Mg#:	90·2	89·7	90·9	89·9	89·8	90·2	88·9	89·7	89·7	89·9	90·5	89·7	89·7
Cr#:	6·8	5·0	6·6	6·2	5·8	8·1	—	5·5	5·0	7·0	9·6	6·1	5·4
wt %													
SiO_2	44·96	44·72	44·15	44·88	44·78	44·81	43·88	45·20	44·97	43·83	44·96	44·49	44·66
TiO_2	0·09	0·12	0·09	0·08	0·11	0·06	0·06	0·13	0·12	0·08	0·02	0·11	0·12
Al_2O_3	2·69	3·43	2·37	2·91	3·03	2·35	2·10	3·49	3·36	2·43	2·03	3·23	3·32
FeO^T	7·83	7·86	7·55	7·93	8·02	7·81	9·39	7·79	7·80	8·31	7·68	7·95	8·00
MnO	0·13	0·13	0·12	0·13	0·13	0·13	0·13	0·13	0·13	0·13	0·12	0·13	0·13
MgO	40·43	38·25	42·15	39·48	39·45	40·34	42·16	38·00	38·24	41·37	41·05	38·99	39·02
CaO	2·37	3·14	2·29	2·70	2·62	2·19	1·84	3·20	3·23	1·98	1·97	2·80	2·98
Na_2O	0·29	0·27	0·26	0·10	0·17	0·02	0·07	0·17	0·16	0·06	0·10	0·19	0·22
K_2O	0·07	0·04	0·11	0·04	0·05	0·10	0·02	0·05	0·05	0·03	0·06	0·07	0·04
P_2O_5	0·01	0·01	0·02	0·01	0·02	0·01	0·01	0·01	0·01	0·01	0·01	0·01	0·01
Cr_2O_3	0·29	0·27	0·25	0·28	0·28	0·31	—	0·30	0·27	0·27	0·31	0·30	0·28
NiO	0·22	0·20	0·23	0·21	0·21	0·22	—	0·24	0·20	0·01	0·23	0·21	0·20
LOI %	0·49	0·57	0·08	0·27	0·29	0·95	–0·08	0·33	0·51	0·71	0·58	0·56	0·32
Total	99·9	99·0	99·7	99·0	99·2	99·3	99·6	99·0	99·0	99·2	99·1	99·0	99·3
ppb													
Li	1769	1821	2683	1692	1801	1811	1674	1730	1806	1863	1647	1811	1738
Be	17·4	9·60	38·3	5·60	27·9	13·4	18·6	22·2	22·6	15·5	5·80	23·0	17·7
Sc	12986	15087	12280	14225	13755	12316	11252	15603	15272	11807	11443	14173	14731
Ti	532438	664993	551628	465521	620928	294635	329580	755265	712609	485017	78998	642569	700895
V	62320	77187	57015	67661	68397	57957	49825	80558	77511	55324	51950	74126	73900
Cr	2964382	2777016	2233959	2894264	2776010	2915254	2425515	2698707	2974016	2430119	2793885	2844323	2774802
Co	120889	115842	127790	117647	114660	127020	115857	119723	118418	125488	129195	126421	118977
Ni	1981787	1899002	2038676	1895749	1894941	2045040	2121382	1849798	1895762	2027842	2092663	1941239	1882194
Cu	21242	28576	18501	20324	29604	20503	13714	32285	26469	20436	15797	28107	23770
Zn	48177	50953	47963	49119	48557	48919	47895	46244	48852	47407	45529	48864	48668
Ga	2454	3085	2267	2588	2775	1813	1790	3049	3027	2083	1445	2831	3034
Rb	1280	393	1031	710	604	1744	292	1416	781	1972	1083	887	772
Sr	6728	5758	8574	3214	13293	3565	6972	9698	18634	7524	1102	11982	11467
Y	2267	2984	2335	2236	2576	1353	2281	3420	3126	1850	520	2733	2995
Zr	4527	3316	4809	1520	6431	2667	29734	5645	5725	4640	1125	5485	4600
Nb	282	21·2	240	50·8	664	198	165	637	285	426	117	358	107
Cd	25·0	28·2	31·9	23·4	27·0	20·1	19·2	28·9	26·4	23·5	16·6	25·7	26·7
In	10·7	13·1	11·1	11·5	11·9	8·40	9·30	13·8	12·4	10·3	6·90	12·0	12·8
Sn	57·4	109	43·8	9·80	68·6	62·6	231	64·7	78·8	33·6	2·50	40·7	70·3
Sb	26·5	4·50	5·40	2·40	37·1	29·0	33·4	17·3	16·9	8·10	5·80	25·5	14·6
Cs	6·70	1·50	3·30	2·40	4·60	10·5	1·80	2·70	8·70	3·80	6·00	8·50	5·00
Ba	221	147	977	114	1453	3648	273	222	325	174	189	572	89·9
La	69·6	31·5	258	28·9	250	125	126	113	114	95·9	37·8	163	46·3
Ce	282	209	618	122	667	282	257	444	434	335	79·2	521	281
Pr	60·7	57·6	92·1	31·6	107	42·4	48·3	90·7	89·9	61·1	9·90	95·3	70·8
Nd	386	414	482	241	567	222	284	557	550	346	40·1	544	476
Sm	171	208	182	134	212	88·5	115	249	240	141	11·4	219	223
Eu	72·0	89·6	73·5	57·8	86·3	35·8	47·8	105	99·9	57·9	4·80	89·7	94·1
Gd	277	354	279	246	319	150	185	412	384	224	26·5	339	368
Tb	53·5	69·7	53·9	49·6	61·1	29·8	36·3	80·7	74·2	43·5	7·00	65·7	71·7
Dy	369	490	376	353	423	218	260	568	516	303	64·6	453	500
Ho	86·5	115	88·1	84·5	97·4	52·5	62·5	132	120	71·5	18·8	105	115
Er	260	341	267	257	292	159	190	387	354	214	67·9	309	344
Tm	39·7	52·4	42·0	40·1	45·3	25·6	31·2	60·1	55·1	34·2	12·6	47·7	53·5
Yb	260	344	279	269	302	174	213	394	364	227	97·2	316	349
Lu	41·2	53·5	44·9	42·6	46·8	28·1	34·4	59·9	56·0	35·8	16·6	49·4	54·6
Hf	118	126	126	75·1	153	70·6	663	158	162	115	15·5	149	150
Ta	109	91·8	191	103	81·3	139	4·50	143	100	93·6	156	182	114
W	163701	141837	267061	152041	110368	158215	n.d.	168821	121989	115578	183136	200556	138159
Tl	0·50	1·40	2·60	0·70	0·70	1·10	0·40	0·80	1·40	1·50	0·90	1·10	0·50
Pb	110	107	91·6	61·1	89·7	126	76·9	122	64·3	96·8	56·6	110	49·5
Bi	0·90	1·10	1·10	1·30	1·40	0·80	0·50	1·10	1·60	1·10	0·50	1·10	0·90
Th	6·00	2·00	82·7	2·00	17·9	21·1	6·80	4·90	7·00	3·90	8·70	9·40	1·30
U	50·1	14·6	56·2	7·00	98·2	40·2	34·0	46·3	48·6	16·2	29·5	31·4	26·9

OU no., Otago University catalogue number; Mg# = 100 Mg/(Mg + Fe); Cr# = 100Cr/(Cr + Al); T, total. LOI %, loss on ignition; n.d., not determined.

Table 3. Whole-rock chemistry of Mount Morning pyroxenite xenoliths

Field no.:	LZL02	LZ01	CD06	CD02	CD03	WZ01	WZ02	WZ08	WZ14	435B-I	435B-II	435B-III
OU no.:	78474	78702	78465	78461	78462	78483	78484	78487	78488	78691	78692	78693
Mg#:	88·9	90·1	90·1	90·3	90·1	77·1	78·5	78·2	78·2	89·5	74·9	90·4
Cr#:	1·8	—	5·6	16·7	12·8	2·9	2·7	2·5	1·5	0·1	1·2	0·0
wt %												
SiO_2	53·84	51·13	48·41	53·64	53·10	43·24	44·89	44·62	45·44	52·06	46·26	48·74
TiO_2	0·11	0·20	0·10	0·11	0·15	1·26	1·46	1·58	1·57	0·35	1·99	0·61
Al_2O_3	2·62	5·75	10·73	2·33	2·52	5·35	6·30	6·66	6·69	3·87	9·30	8·98
FeO^T	7·40	5·92	4·59	4·18	3·73	12·81	9·52	9·61	9·00	3·41	8·03	2·72
MnO	0·14	0·11	0·12	0·12	0·11	0·20	0·16	0·16	0·15	0·06	0·15	0·05
MgO	33·22	29·23	23·33	21·89	19·23	24·19	20·48	19·35	18·14	16·35	13·41	14·30
CaO	1·61	6·43	10·86	15·64	18·97	12·04	16·56	16·58	17·62	24·83	19·88	25·27
Na_2O	0·04	0·32	0·62	0·29	0·45	0·45	0·37	0·39	0·39	0·20	1·05	0·24
K_2O	0·05	0·01	0·02	0·02	0·04	0·06	0·03	0·04	0·03	0·03	0·07	0·03
P_2O_5	0·01	0·01	0·01	0·01	0·01	0·05	0·03	0·03	0·03	0·02	0·06	0·04
Cr_2O_3	0·07	—	0·95	0·71	0·55	0·24	0·26	0·25	0·16	0·01	0·16	0·20
NiO	0·01	—	0·07	0·06	0·04	0·24	0·01	0·01	0·04	0·01	0·01	0·00
LOI %	–0·12	–0·07	0·02	0·10	0·16	–0·28	–0·28	–0·27	–0·21	–0·54	–0·49	–0·50
Total	99·0	99·0	99·8	99·1	99·1	99·8	99·8	99·0	99·0	100·6	99·9	100·7
ppb												
Li	2110	1308	1263	3642	4390	1664	1468	1309	1302	n.d.	2593	292
Be	46·4	50·9	75·0	46·1	62·0	226·7	203·6	225	220	n.d.	367·4	1449
Sc	12680	26674	45953	26908	29008	51038	71037	72859	74061	10128	67849	2418
Ti	656335	1221595	548887	649099	890606	7984053	9309811	10016941	9817242	n.d.	12500262	3991332
V	64881	137682	141700	119009	124620	231869	287953	294223	303840	67350	336456	69558
Cr	4053661	6263866	10505437	6814468	6722782	827783	1614050	690528	1489633	55945	2024283	3613
Co	88723	61070	79892	75857	55021	124341	97971	97138	79056	37279	49029	23566
Ni	921481	1073550	743154	523342	395785	490439	341981	265242	321550	101200	128643	4576
Cu	4649	56234	17311	16316	14656	165655	80680	40978	117889	n.d.	9476	2455
Zn	50795	43783	45249	21723	19091	68345	45698	43962	39175	n.d.	35798	29727
Ga	3369	4203	4696	2765	3027	8854	9945	10398	10412	6443	13772	13341
Rb	1042	785	227	395	689	1169	648	681	545	208	1274	99·0
Sr	4342	26562	38394	39145	61121	69152	80586	81111	82281	76668	173391	108211
Y	964	8083	3352	3021	4237	11592	13668	14376	14487	15092	18274	21309
Zr	4150	168428	5051	4397	6740	64826	63073	68778	67282	66457	79651	240904
Nb	867	362	146	721	1201	4363	1876	2239	1793	2336	3874	10407
Cd	25·8	35·2	34·4	159	57·3	100	86·2	84·4	103	n.d.	92·2	92·6
In	11·4	16·4	13·7	13·3	14·5	59·1	67·7	69·6	70·7	n.d.	79·4	76·8
Sn	36·1	305	83·4	184	182	889	1092	867	962	n.d.	1452	4236
Sb	3·00	6·30	6·20	6·50	4·30	6·70	6·00	6·90	10·4	n.d.	8·00	1·80
Cs	12·5	4·40	1·80	4·20	8·10	17·6	6·00	6·00	5·30	n.d.	10·9	8·00
Ba	3942	1032	380	2721	5244	13798	6635	8401	5667	641	15189	34901
La	384	327	246	577	1013	4342	3922	4198	4088	7271	8048	11855
Ce	681	1021	998	1595	2758	12767	13045	13780	13670	23243	23509	34457
Pr	76·8	191	209	272	465	2101	2298	2416	2415	3419	3821	4962
Nd	310	1137	1220	1467	2428	10484	11867	12501	12566	14253	18965	20469
Sm	88·5	501	383	481	743	2928	3428	3619	3643	3168	5059	4494
Eu	30·2	227	167	148	226	983	1160	1224	1229	557	1755	807
Gd	116	807	499	555	818	3090	3633	3845	3868	2854	5149	4019
Tb	22·1	152	89·3	91·0	132	461	544	574	577	478	744	635
Dy	158	1015	587	568	804	2551	3013	3181	3190	2777	4048	3744
Ho	37·3	223	131	121	167	477	563	590	595	556	749	767
Er	116	624	371	328	448	1165	1362	1431	1446	1603	1797	2147
Tm	19·5	93·1	56·3	47·1	63·6	154	180	186	190	249	233	328
Yb	141	581	366	290	390	898	1031	1070	1092	1511	1335	2097
Lu	22·4	87·7	55·5	41·1	54·5	122	139	146	148	237	178	304
Hf	97·7	3839	129	130	195	2205	2383	2657	2558	1744	2791	5763
Ta	181	16·4	10·9	39·5	65·7	251	183	210	301	354	362	1998
W	171507	n.d.	186022	251450	147465	126107	180635	192975	139010	n.d.	74090	122944
Tl	1·60	0·90	0·30	3·70	1·60	3·30	1·20	0·70	1·00	n.d.	1·70	1·00
Pb	67·7	391	94·8	184	225	526	255	268	362	859	126	153
Bi	1·00	2·50	1·20	3·60	4·30	15·6	5·20	5·70	8·70	n.d.	1·90	2·30
Th	94·5	42·5	15·5	53·9	137	270	154	179	154	1899	380	5728
U	48·0	127·3	10·6	29·9	39·0	85·7	53·7	63·6	53·5	205	103	849

OU no., Otago University catalogue number; Mg# = 100 Mg/(Mg + Fe); Cr# = 100Cr/(Cr + Al); T, total; LOI %, loss on ignition; n.d., not determined.

Table 4. Representative mineral chemistry (values in wt %) from Mount Morning mantle xenoliths

Rock type	OU no.	Field ID	Mg#	SiO_2	TiO_2	Al_2O_3	FeO^T	MnO	MgO	CaO	Na_2O	K_2O	Cr_2O_3	NiO
Clinopyroxene														
Hz	78473	LZL01	91·3	53·63	b.d.	2·91	2·36	b.d.	16·82	23·00	0·45	b.d.	0·63	b.d.
Hz	78477	LZL05	91·0	53·70	b.d.	4·38	2·38	b.d.	16·11	20·97	1·30	b.d.	1·25	b.d.
Hz	78515	LL03	91·2	52·74	b.d.	4·18	2·75	b.d.	16·06	22·41	1·00	b.d.	0·77	b.d.
Sp Lz	78441	237 02	88·3	47·53	2·82	6·67	3·26	b.d.	14·70	23·95	0·56	b.d.	1·06	b.d.
Sp Lz	78703	LZM 01	92·0	52·76	b.d.	3·21	2·66	b.d.	17·08	21·94	0·75	b.d.	1·00	b.d.
Pl Sp	78475	LZL03	91·2	52·29	0·64	6·21	2·61	b.d.	15·32	20·46	2·07	b.d.	0·96	b.d.
Pyroxenite	78702	LZ01	90·1	53·04	0·42	5·74	2·34	b.d.	15·35	21·23	1·42	b.d.	0·89	b.d.
Pyroxenite	78465	CD06	91·4	51·60	0·29	6·39	2·63	b.d.	15·67	21·82	1·05	0·06	0·77	b.d.
Pyroxenite	78461	CD02	91·2	53·26	b.d.	2·16	2·89	b.d.	16·73	22·24	0·56	b.d.	1·08	—
Pyroxenite	78484	WZ02	72·9	48·22	2·87	5·13	8·47	0·24	12·80	22·28	0·34	b.d.	b.d.	b.d.
Pyroxenite	78693	435B-III	92·1	49·58	0·77	7·60	2·17	b.d.	14·55	25·96	0·17	b.d.	b.d.	b.d.
Pyroxenite	78711	CB02	66·2	50·86	0·42	2·09	11·89	b.d.	13·04	20·59	0·34	0·06	0·25	b.d.
Orthopyroxene														
Hz	78473	LZL01	91·2	56·11	b.d.	2·60	5·54	b.d.	33·86	0·69	b.d.	b.d.	0·37	b.d.
Hz	78477	LZL05	90·3	57·01	b.d.	2·71	5·31	b.d.	33·82	0·73	0·11	b.d.	0·38	b.d.
Hz	78515	LL03	91·0	56·09	b.d.	3·45	5·91	b.d.	33·76	0·72	b.d.	b.d.	0·41	b.d.
Sp Lz	78441	237 02	90·5	56·28	b.d.	3·07	6·30	b.d.	33·74	0·68	b.d.	b.d.	0·52	b.d.
Sp Lz	78703	LZM 01	92·2	56·86	b.d.	2·24	5·73	b.d.	34·71	0·68	b.d.	b.d.	0·33	b.d.
Pl Lz	78475	LZL03	88·2	55·63	0·38	3·99	7·23	0·63	32·37	0·31	b.d.	0·14	b.d.	b.d.
Pyroxenite	78702	LZ01	90·5	56·49	b.d.	3·45	5·91	b.d.	33·66	0·62	0·10	b.d.	0·34	b.d.
Pyroxenite	78465	CD06	93·2	55·21	b.d.	3·68	6·31	0·23	33·82	0·71	b.d.	0·07	0·41	b.d.
Pyroxenite	78461	CD02	90·0	56·05	b.d.	1·65	7·24	0·18	33·26	0·72	b.d.	b.d.	0·49	—
Pyroxenite	78711	CB02	90·9	55·49	b.d.	3·76	6·54	b.d.	33·14	0·87	b.d.	0·08	0·44	b.d.
Olivine														
Hz	78473	LZL01	91·0	40·58	b.d.	b.d.	8·74	b.d.	49·79	0·06	b.d.	b.d.	b.d.	0·39
Hz	78477	LZL05	90·9	40·89	b.d.	b.d.	8·91	b.d.	49·94	0·07	b.d.	b.d.	b.d.	0·39
Hz	78515	LL03	90·1	40·14	b.d.	b.d.	9·87	b.d.	50·21	b.d.	b.d.	b.d.	b.d.	0·45
Sp Lz	78441	237 02	90·5	41·21	b.d.	b.d.	9·21	0·20	49·03	0·20	b.d.	b.d.	b.d.	0·28
Sp Lz	78703	LZM 01	91·1	39·78	b.d.	b.d.	8·90	b.d.	50·80	b.d.	b.d.	b.d.	b.d.	0·43
Pl Lz	78475	LZL03	89·6	40·97	b.d.	0·12	10·16	b.d.	47·50	b.d.	b.d.	b.d.	b.d.	0·26
Pyroxenite	78702	LZ01	90·5	41·28	b.d.	b.d.	9·33	b.d.	49·74	0·09	b.d.	b.d.	b.d.	0·40
Pyroxenite	78484	WZ02	79·9	39·66	b.d.	0·11	18·08	0·26	42·23	0·23	b.d.	b.d.	b.d.	b.d.
Pyroxenite	78711	CB02	71·6	38·53	b.d.	b.d.	24·05	0·48	36·93	0·39	b.d.	0·05	b.d.	b.d.
Pyroxenite	78711	CB02	90·0	41·54	b.d.	b.d.	7·88	b.d.	49·78	0·23	b.d.	0·07	b.d.	0·30

Continued

Table 4 Continued

Rock type	OU no.	Field ID	Mg#	SiO_2	TiO_2	Al_2O_3	FeO^T	MnO	MgO	CaO	Na_2O	K_2O	Cr_2O_3	NiO
Spinel														
Hz	78473	LZL01	75·2	b.d.	b.d.	38·74	12·68	b.d.	18·12	b.d.	b.d.	b.d.	29·43	0·29
Hz	78477	LZL05	74·6	b.d.	b.d.	40·71	11·47	b.d.	18·81	b.d.	b.d.	b.d.	28·43	b.d.
Hz	78515	LL03	80·9	b.d.	b.d.	48·51	10·01	b.d.	20·38	b.d.	b.d.	b.d.	20·55	0·33
Sp Lz	78441	237 02	70·3	b.d.	1·46	28·89	18·52	0·28	16·97	b.d.	b.d.	b.d.	33·58	b.d.
Sp Lz	78703	LZM 01	74·8	b.d.	b.d.	37·73	13·10	b.d.	17·93	b.d.	b.d.	b.d.	29·76	b.d.
Pl Lz	78475	LZL03	86·5	0·30	b.d.	51·15	11·63	0·37	20·26	b.d.	1·18	b.d.	13·92	0·33
Pyroxenite	78702	LZ01	80·3	b.d.	b.d.	51·55	10·47	b.d.	20·72	b.d.	b.d.	b.d.	16·91	0·40
Pyroxenite	78465	CD06	82·6	b.d.	b.d.	59·20	10·51	b.d.	21·85	b.d.	b.d.	b.d.	8·05	0·47
Pyroxenite	78461	CD02	59·0	b.d.	0·27	21·60	19·75	0·62	12·15	0·13	b.d.	b.d.	44·29	b.d.
Pyroxenite	78484	WZ02	12·5	0·11	22·31	1·94	69·29	0·91	3·73	0·08	b.d.	b.d.	b.d.	b.d.
Pyroxenite	78693	435B-III	95·0	b.d.	b.d.	61·22	11·80	b.d.	26·22	0·11	b.d.	b.d.	b.d.	b.d.
Pyroxenite	78711	CB02	80·0	b.d.	b.d.	53·76	11·66	b.d.	20·52	b.d.	b.d.	b.d.	13·96	0·32
Pyroxenite	78711	CB02	23·1	0·10	17·73	9·21	57·06	0·63	6·71	b.d.	b.d.	b.d.	6·54	0·27
Norite	78686	435A-I	85·2	b.d.	0·0	64·4	8·0	0·1	26·0	b.d.	b.d.	b.d.	0·2	0·3
Norite	78686	435A-I	3·1	0·1	1·8	24·2	67·6	0·2	1·2	0·1	b.d.	0·0	0·1	0·1
Feldspar			An.											
Pl Lz	78475	LZL03	38·457	58·38	b.d.	26·76	b.d.	b.d.	0·47	8·04	7·11	b.d.	b.d.	b.d.
Pl Lz	78475	LZL03	39·941	57·68	b.d.	26·92	b.d.	b.d.	0·57	8·40	6·98	b.d.	b.d.	b.d.
Pl Lz	78526	LL15	39·591	58·05	b.d.	26·97	b.d.	b.d.	0·56	8·29	6·99	b.d.	b.d.	b.d.
Pl Lz	78478	LZL06	38·972	58·23	b.d.	26·87	b.d.	b.d.	0·52	8·17	7·07	b.d.	b.d.	b.d.
Pyroxenite	78702	LZ01	38·306	59·39	b.d.	25·20	0·13	b.d.	b.d.	8·07	7·14	0·06	b.d.	b.d.
Pyroxenite	78465	CD06	50·935	55·05	b.d.	27·92	0·22	b.d.	b.d.	10·63	5·54	0·18	b.d.	b.d.

All mineral chemistry analyses are given in the Supplementary Data Appendix 1. T, total; Hz, harzburgite; Sp Lz, spinel lherzolite; Pl Lz, plagioclase lherzolite; OU no., Otago University catalogue number; An, anorthite content. b.d., below detection limit. Pyroxenite rock types are shown in Table 1.

Table 5. Geothermobarometry and oxygen fugacity

	Specimen. no.	Field ID	Rock type	P (kbar)[1]	T_3 (°C)[2]	Δlog fO_2 Wood[3]	Ballhaus[4]	O'Neill	Luth & Wall[5] Canil[6]
Peridotite	OU78473	LZL01	Harzburgite	5·5	882	0·2	–0·2	–0·5	3·6
Peridotite	OU78477	LZL05	Harzburgite	9·3	967	–0·4	–0·7	–1·1	–2·4
Peridotite	OU78515	LL03	Harzburgite	6·1	875	0·0	–0·6	–0·5	—
Peridotite	OU78441	237 02	Lherzolite	3·0	796	1·0	0·8	0·1	0·6
Peridotite	OU78703	LZM 01	Lherzolite	6·4	934	0·2	–0·2	–0·3	–1·0
Peridotite	OU78475	LZL03	Pl lherzolite	11·0	925	—	—	—	—
Peridotite	OU78480	LZL08	Pl lherzolite	8·3	951	—	—	—	—
Peridotite	OU78526	LL15	Pl lherzolite	10·1	921	—	—	—	—
Peridotite	OU78478	LZL06	Pl lherzolite	9·7	973	—	—	—	—
Pyroxenite	OU78702	LZ01	Pl websterite	9·4	932	–0·5	–1·0	–1·1	–0·9
Pyroxenite	OU78465	CD06	Pl websterite	8·0	941	—	—	—	—
Pyroxenite	OU78461	CD02	Websterite	4·8	912	—	—	—	—
Peridotite	OU78711	CB–wall	Harzburgite	6·2	943	—	—	—	—
Pyroxenite	OU78711	CB–vein	Websterite	10·9	1068	—	—	—	—

[1]Barometer of Putirka (2008).
[2]Thermometer based upon clinopyroxene with Mg# > 0·75 from Putirka (2008; Thermometer 3 in text) using pressure calculated in column 1.
[3]Olivine–orthopyroxene–spinel oxygen barometer of Wood *et al.* (1990) using column 1 barometer and column 2 thermometer.
[4]Olivine–orthopyroxene–spinel oxygen barometer of Ballhaus *et al.* (1991) using column 1 barometer and column 2 thermometer.
[5]Olivine–orthopyroxene–spinel oxygen barometer of O'Neill & Wall (1987) updated by H. S. C. O'Neill (personal communication).
[6]Olivine–orthopyroxene–clinopyroxene oxygen barometer of Luth & Canil (1993) using column 1 barometer and column 2 thermometer.

Plagioclase-bearing pyroxenites. Two of the Mount Morning pyroxenites are plagioclase-bearing. One is a plagioclase-bearing olivine websterite (OU78 702) and the other a plagioclase-bearing websterite (OU78 465). In hand specimen the plagioclase–olivine websterite looks very similar to peridotite, whereas the plagioclase websterite is dominated by iridescent green clinopyroxene. Significant amounts of spinel (10%) and plagioclase (3%) are present in the plagioclase websterite. In thin section, plagioclase is observed as equidimensional neoblasts (~0·2 mm) adjacent to spinel porphyroclasts and multiple twinning is commonly present. Plagioclase neoblasts form triple-point junctions with other minerals. Clinopyroxene is observed as porphyroclasts (≤2 mm) and neoblasts (≤0·2 mm). Orthopyroxene porphyroclasts are coarser (≤3 mm) and more common than the clinopyroxene porphyroclasts and they display exsolution lamellae and rare kink banding. Orthopyroxene neoblasts are ~0·2 mm in diameter. Spinel occurs as both porphyroclasts (≤4 mm) and neoblasts (≤2 mm) and the former may poikiloblastically enclose chadocrysts of other phases. Olivine (in the plagioclase–olivine websterite) occurs as both porphyroclasts (≤3 mm), which are in rare cases kink banded, and as neoblasts (~0·2 mm).

Composite xenolith. Pyroxenites crosscutting peridotite wall-rock have been observed in tectonically emplaced ultramafic bodies (massifs and ophiolites) and in xenolith suites worldwide (Irving, 1980; Nielson & Wilshire, 1993; Braun & Kelemen, 2002). Rare, compositionally banded xenoliths have also been collected from Mount Morning, with websterite veins up to 10 mm wide, crosscutting the peridotite host-rock (Fig. 3b).

Pyroxenite, Al-augite series

Clinopyroxenite. This rock type, which is dark green in hand specimen, consists of >90% clinopyroxene, with orthopyroxene and spinel occurring as additional phases in some, but not all, samples. Xenoliths of this type are ≤100 mm in diameter and commonly have an igneous texture. In thin section, clinopyroxene is ≤4 mm across. Indications of deformation within clinopyroxene are variable, with some grains being undeformed and others showing undulose extinction or very weakly developed kink banding. Fluid inclusion trails, up to 0·1 mm across, are common in clinopyroxene. Orthopyroxene is a modally minor phase (<1% or absent) that occurs as phenocrysts up to 3 mm in diameter. Spinel is observed as euhedral crystals in the groundmass and as phenocrysts, varying in diameter between 0·1 and 2 mm.

Phlogopite-bearing clinopyroxenite. One specimen of phlogopite-bearing clinopyroxenite has been collected from Mount Morning. It had a maximum dimension of 20 mm and, in hand specimen, an appearance identical to clinopyroxenite. Phlogopite is a modally minor phase (≪1 %) observed as primary crystallized, tabular crystals ≤0·3 mm long. Clinopyroxene is equigranular (0·1 mm) with triple-point junctions between grains and common fluid inclusions. Spinel is observed in the groundmass and as phenocrysts varying in diameter between 0·1 and ≤2 mm. Rare apatite grains (≤0·1 mm) also occur in this specimen.

Wehrlite and olivine clinopyroxenite. This xenolith type has a distinctive black and yellow mottled appearance in hand specimen and an igneous texture. Samples range in size up to 40 mm. In thin section clinopyroxene

Table 6. Hyperfine parameters and $Fe^{3+}/\sum Fe$ from Mössbauer spectroscopy

Specimen no.	Field ID	Fe^{2+} (I)			Fe^{2+} (II)			Fe^{2+}				Fe^{3+}			$Fe^{3+}/\sum Fe$	χ^2
		IS	QS	FWHH	IS	QS	FWHH	IS	QS	FWHH	Area %	IS	QS	FWHH		
Spinel																
OU78441	237 02	0·81 (1)	1·53 (4)	0·76 (5)	0·66 (3)	0·66 (4)	0·88 (2)	—	—	—	2	0·20 (2)	0·67 (5)	0·37 (5)	0·222	1·05
OU78703	LZM01	0·77 (1)	2·01 (4)	0·41 (5)	0·78 (9)	1·18 (5)	0·60 (5)	—	—	—	54	0·21 (1)	0·59 (4)	0·35 (5)	0·183	0·88
OU78473	LZL 01	0·76 (7)	1·96 (3)	0·43 (4)	0·79 (6)	1·19 (4)	0·60 (4)	—	—	—	52	0·22 (8)	0·59 (1)	0·31 (2)	0·200	1·15
OU78477	LZL 05	0·76 (2)	2·03 (6)	0·40 (10)	0·78 (2)	1·27 (5)	0·62 (5)	—	—	—	63	0·18 (1)	0·66 (3)	0·30 (3)	0·179	1·01
OU78515	LL03	0·76 (3)	2·42 (5)	0·16 (9)	0·82 (1)	1·36 (4)	0·66 (7)	—	—	—	72	0·21 (2)	0·62 (3)	0·29 (5)	0·223	1·08
OU78702	LZ01	0·76 (9)	1·97 (3)	0·40 (4)	0·78 (1)	1·19 (5)	0·63 (7)	—	—	—	57	0·23 (2)	0·62 (4)	0·34 (4)	0·153	0·99
Orthopyroxene																
OU78441	237 02	—	—	—	—	—	—	—	—	—	—	—	—	—	—	—
OU78703	LZM01	1·03 (2)	2·97 (3)	0·26 (7)	1·04 (8)	2·15 (2)	0·38 (5)	—	—	—	79	0·41 (2)	0·53 (3)	0·20 (3)	0·022	2·28
OU78473	LZL 01	1·03 (3)	2·97 (6)	0·36 (4)	1·04 (8)	2·15 (3)	0·36 (4)	—	—	—	82	0·41 (2)	0·54 (4)	0·22 (3)	0·021	1·48
OU78477	LZL 05	1·03 (3)	2·95 (8)	0·28 (1)	1·04 (1)	2·15 (3)	0·35 (7)	—	—	—	80	0·39 (3)	0·53 (8)	0·30 (6)	0·036	1·51
OU78515	LL03	1·02 (5)	2·89 (1)	0·28 (2)	1·03 (10)	2·14 (2)	0·34 (4)	—	—	—	87	0·40 (2)	0·59 (6)	0·27 (6)	0·021	1·47
OU78702	LZ01	1·02 (6)	2·93 (1)	0·22 (2)	1·04 (8)	2·16 (2)	0·38 (4)	—	—	—	91	0·41 (2)	0·58 (4)	0·22 (5)	0·020	1·66
Clinopyroxene																
OU78441	237 02	1·04 (4)	3·06 (2)	0·17 (5)	1·04 (4)	2·80 (5)	0·26 (5)	1·03 (4)	2·08 (2)	0·50 (2)	81	0·48 (3)	0·47 (4)	0·46 (9)	0·093	1·17
OU78703	LZM01	1·04 (2)	3·06 (2)	0·22 (2)	1·03 (2)	2·86 (4)	0·26 (3)	1·03 (6)	2·09 (1)	0·46 (2)	63	0·25 (3)	0·40 (8)	0·71 (8)	0·136	0·97
OU78473	LZL 01	1·04 (1)	3·16 (8)	0·21 (1)	1·03 (10)	2·90 (1)	0·29 (3)	1·05 (3)	2·08 (1)	0·45 (2)	76	0·12 (1)	0·43 (4)	0·39 (4)	0·041	1·60
OU78477	LZL 05	1·04 (2)	3·09 (1)	0·21 (1)	1·03 (1)	2·89 (2)	0·25 (1)	1·04 (4)	2·10 (9)	0·43 (2)	66	0·22 (2)	0·16 (23)	0·76 (1)	0·089	1·13
OU78515	LL03	—	—	—	—	—	—	—	—	—	—	—	—	—	—	—
OU78702	LZ01	1·05 (2)	2·28 (10)	0·40 (1)	1·04 (4)	2·97 (1)	0·28 (2)	1·03 (1)	1·96 (7)	0·44 (5)	58	0·20 (6)	0·47 (2)	0·85 (1)	0·191	1·14

IS, isomer shift, error ± 0·01; QS, quadrupole splitting, error ± 0·02; FWHH, half width, error ± 0·02; A, area; $Fe^{3+}/\sum Fe$ error ± 0·01; χ^2, reduced chi-squared. Error at 1SD is given in parentheses.

phenocrysts (≤5 mm) commonly have fluid inclusion trails and, in some cases, weakly developed kink bands. Some clinopyroxene grains form oikocrysts poikilitically enclosing chadocrysts of olivine. Olivine occurs as phenocrysts (≤5 mm) and chadocrysts. Spinel is an accessory phase (1–2%) with grain sizes that are significantly less (0·4 mm) than those of the clinopyroxene or olivine phenocrysts. Groundmass spinel is commonly observed at the grain boundaries of other phases. Rare amphibole grains (≤0·2 mm) occur, showing curviplanar contacts against surrounding mineral grains.

Mineral major element compositions

Nearly all clinopyroxene compositions plot within the diopside field [nomenclature after Morimoto (1989)] and all orthopyroxenes lie within the enstatite field of the pyroxene quadrilateral (not shown). Upton *et al.* (2011) have calculated a hypothetical melting trend for wt % Al_2O_3 and MgO in clinopyroxene and orthopyroxene assuming a primitive mantle source [from McDonough & Sun (1995)], and pressures and temperatures within the spinel stability field, based on calculations given in Workman & Hart (2005). For the most part the Mount Morning pyroxenes follow the hypothetical melting trend, with the harzburgite data showing, in general, lower wt % Al_2O_3 and higher MgO abundances than is the case for pyroxenes from plagioclase lherzolite, and compositions similar to those of pyroxenes from spinel lherzolite (Fig. 4a and b). The Mount Morning clinopyroxene compositions vary between 0·32 and 1·47 Na_2O and 0·25 and 1·37 Cr_2O_3 (Fig. 4c). There is also a high-sodium group of clinopyroxenes from the plagioclase lherzolite xenoliths (Fig. 4c), with Na_2O contents between 1·96 and 2·13 wt %.

All spinel and olivine compositions from the peridotites and Cr-diopside series pyroxenites plot within the olivine-spinel mantle array (Fig. 5a) with olivine Mg# [100Mg/(Mg + Fe^{2+})] varying between 89·0 and 91·4 for lherzolite (spinel + plagioclase; n = 35), 90·1 and 91·9 for harzburgite (n = 50) and 90·3 and 90·6 for plagioclase-bearing olivine websterite (n = 17). One wehrlite olivine grain has Mg# 79·9 and olivine in the composite xenolith has Mg# 90·0 in the host peridotite and Mg# 71·6 in the vein. Contents of NiO and CaO are typical of those observed in mantle olivine (e.g. Putirka *et al.*, 2011). In general, olivine Mg# and spinel Cr# are similar in harzburgite and spinel lherzolite and higher in plagioclase lherzolite.

Spinel compositions (Fig. 5b) define a trend on a Mg# vs Cr# [100Cr/(Cr + Al)] plot, with plagioclase lherzolite having the highest Mg# (76·0–86·5; n = 11) and lowest Cr# (11·7–15·0) values, spinel lherzolite having the lowest Mg# (68·2–75·8; n = 22) and highest Cr# (34·0–43·1) values and harzburgite Mg# and Cr# values plotting between the two. Spinel in the plagioclase-bearing olivine websterite has low Cr# and high Mg# values relative to spinel in websterite. All the peridotite and Cr-diopside series pyroxenite spinel data overlap with values typically found in mantle spinel from continental rift settings (Fig. 5b). The websterite vein in composite xenolith OU78 711 has Mg# 23·6 and Cr# 33·3. One wehrlite analysis has Mg# 12·5, and Mg# varies between 91·9 and 96·9 (n = 4) in the phlogopite-bearing clinopyroxenite xenolith.

Feldspar compositions from plagioclase lherzolite specimens plot in a tight cluster within the andesine field of the feldspar ternary diagram ($An_{38·4–41·1}Or_{0·0}$; Fig. 5c). Feldspar data from the two specimens of plagioclase-bearing olivine websterite plot in two groups. Plagioclase from sample OU78 702 has a slightly lower An content ($An_{37·1–38·4}$) than the plagioclase from the plagioclase lherzolites whereas the feldspar in sample OU78 465 has a slightly higher An content ($An_{47·6–50·9}$), plotting in both the andesine and labradorite fields. Both pyroxenite specimens contain feldspar with a minor Or component ($Or_{>0–1·2}$).

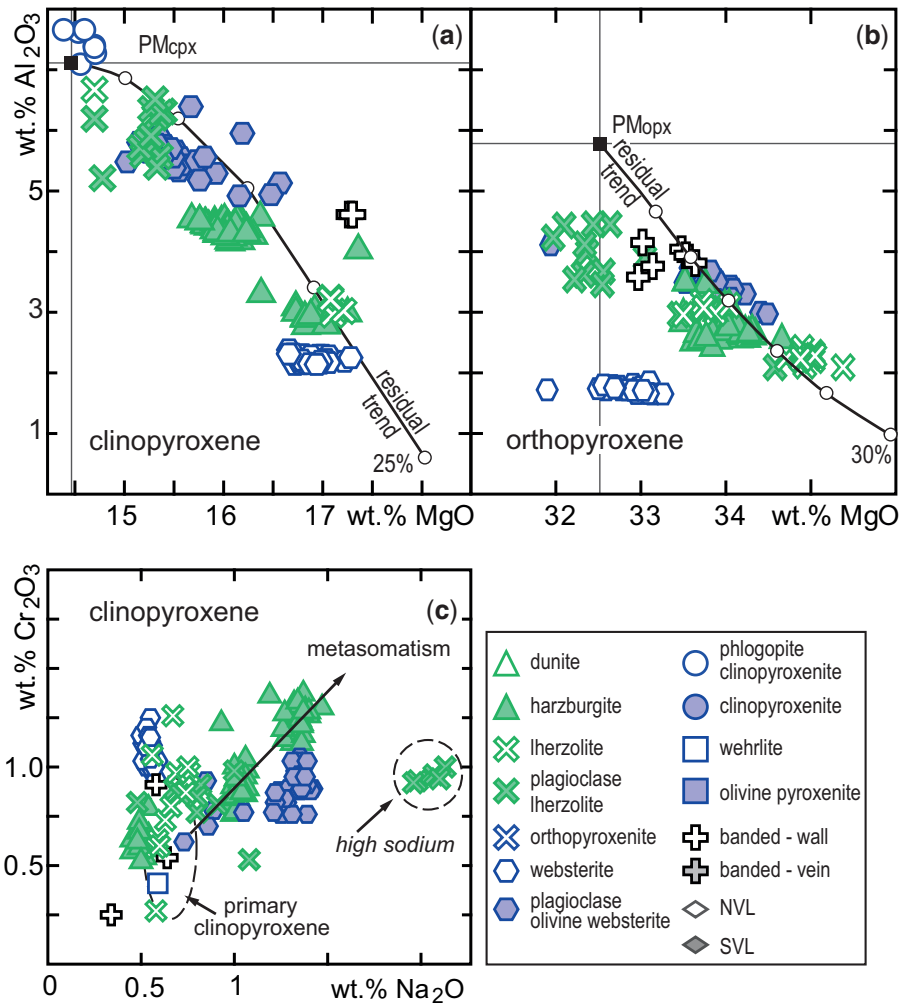

Fig. 4. Pyroxene major element chemistry of Mount Morning mantle xenoliths. (a) Wt % MgO vs Al_2O_3 in clinopyroxene. PMcpx (clinopyroxene; straight grey lines) and theoretical residual trend (curved black line) are from Upton *et al.* (2011) using the primitive mantle composition (spinel stability field) from McDonough & Sun (1995) and equations from Workman & Hart (2005). (b) Wt % MgO vs Al_2O_3 in orthopyroxene. Melting trends and primitive mantle values as in (a). (c) Wt % Na_2O vs Cr_2O_3 in clinopyroxene. Dashed line indicates the field of cpx1 (primary clinopyroxene) from Perinelli *et al.* (2008). Pyroxenes with high Cr_2O_3 and/or Na_2O plotting along the arrowed trend are inferred to have undergone some degree of melt metasomatism (Perinelli *et al.*, 2008). The group of high-sodium clinopyroxenes should be noted.

Feldspars from Northern Victoria Land plagioclase-bearing peridotite xenoliths (after Zipfel & Wörner, 1992; Perinelli *et al.*, 2011) include examples that are Or free (sample WR18–148b, $An_{78.1}$; sample RH07–217d, $An_{core\ 57.9}$) and others that contain some Or component (sample RH07–217c, $An_{core\ 80.3}Or_{core\ 0.2}$).

Geothermobarometry

The temperature and pressure of equilibration of several samples has been calculated using two-pyroxene thermobarometry (Table 5). Pressure was calculated using the temperature-independent barometer of Putirka [2008, his equation (38)]. This barometer returned geologically reasonable pressures between 11 and 4·8 kbar (and one low pressure value at 3 kbar for sample OU78 441) in agreement with other pressure estimates for mantle rocks in the region (e.g. Gamble & Kyle, 1987; Gamble *et al.*, 1988; Berg *et al.*, 1989; Zipfel & Wörner, 1992; Wysoczanski *et al.*, 1995; Martin *et al.*, 2014). Temperature was calculated using three different two-pyroxene thermometers: one from Brey & Kohler (1990; Thermometer 1) and two thermometers from Putirka (2008) that utilize the existing Brey & Kohler (1990) thermometer with a new global regression based on the partitioning of enstatite and ferrosilite between clinopyroxene and orthopyroxene (Putirka, 2008; Thermometer 2). Thermometer 2 can be further refined by considering only clinopyroxenes with Mg# >75 (Putirka, 2008; Thermometer 3). Temperatures obtained using Thermometer 3 most commonly overlap, within one standard deviation, with those temperatures derived from Thermometer 1 or 2 (Fig. 6) and these values are taken as the best estimates of temperature for each sample. Most calculated temperatures from Thermometer 3 are 925 ± 50°C, except for the vein in the composite sample (OU78 711), for which temperature is estimated at 1068°C, and spinel lherzolite sample OU78 441 (pressure 3 kbar), for which the estimated

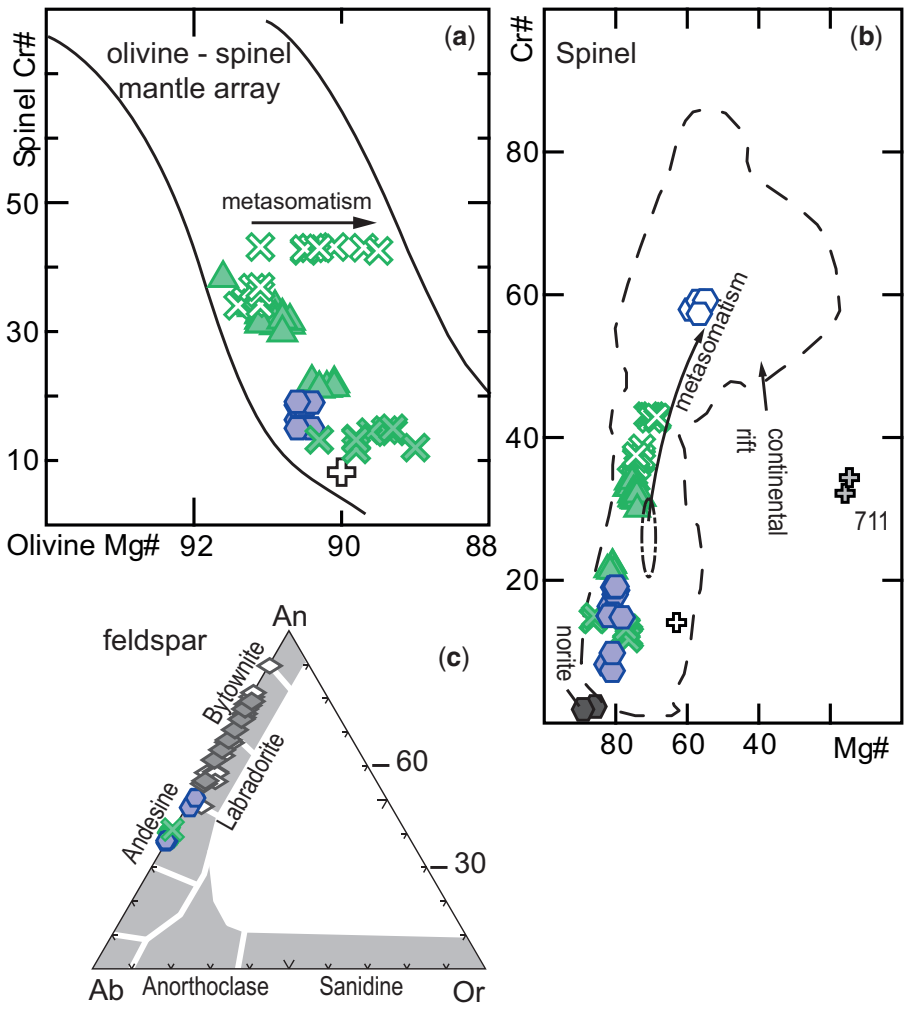

Fig. 5. Major element mineral chemistry of Mount Morning mantle xenoliths. The symbols used are the same as those used in Fig. 4. (a) Olivine Mg# [100Mg/(Mg + Fe^{2+})] vs spinel Cr# [100Cr/(Cr + Al)]. All samples plot within the olivine–spinel mantle array of Arai (1994). (b) Spinel Mg# vs spinel Cr#. The majority of the spinel data plot within the field defined for spinel-facies peridotite from continental rift settings [Martin *et al.* (2014) and references therein] except for spinel from vein material in composite specimen OU78 711. The dot–dashed line indicates the field of primary spinel and the arrow indicates the trend of composition changes induced by metasomatism (Perinelli *et al.*, 2008). (c) Feldspar ternary diagram showing the compositional variation in Mount Morning mantle specimens and selected Northern Victoria Land and Southern Victoria Land samples chosen for comparison (Zipfel & Wörner, 1992; Perinelli *et al.*, 2011; Martin *et al.*, 2014).

temperature is 796°C (Fig. 6). There is poor agreement between the various thermometers for OU78 441 and consequently temperatures estimated for this sample are considered to be less reliable. To check for consistency in temperature, we also applied the olivine–spinel thermometers of O'Neill & Wall (1987) and Ballhaus *et al.* (1991) to the six samples studied using Mössbauer spectroscopy. All temperatures were within 100°C of those listed in Table 5 with the exception of harzburgite OU78 515, for which the olivine–spinel temperature was 200–300°C higher.

Mössbauer spectroscopy

The $Fe^{3+}/\sum Fe$ contents of spinel, and clinopyroxene and orthopyroxene where sufficient material was available, were determined by Mössbauer spectroscopy, including two lherzolites (OU78 703 and 441), three harzburgites (OU78 477, 473 and 515) and one plagioclase-bearing olivine websterite (OU78 702). The $Fe^{3+}/\sum Fe$ contents and hyperfine parameters are reported in Table 6 and Mössbauer spectra are shown in Supplementary Data Fig. A4. Spinel $Fe^{3+}/\sum Fe$ contents vary in the range 0·15–0·22, whereas values for orthopyroxene and clinopyroxene are in the range 0·02–0·04 and 0·04–0·19, respectively (Table 6). The total wt % Fe_2O_3 budget was calculated from Mössbauer measurements of Fe^{3+} in single minerals multiplied by modal abundance and total iron concentration (e.g. O'Neill *et al.*, 1993). Whole-rock wt % Fe_2O_3 values for the harzburgites that were measured are smaller than values for the lherzolites and the websterite (Fig. 7a).

Oxygen fugacity

One of the most effective ways of determining fO_2 is by using oxygen barometry, which utilizes properties within minerals that cannot be easily reset during

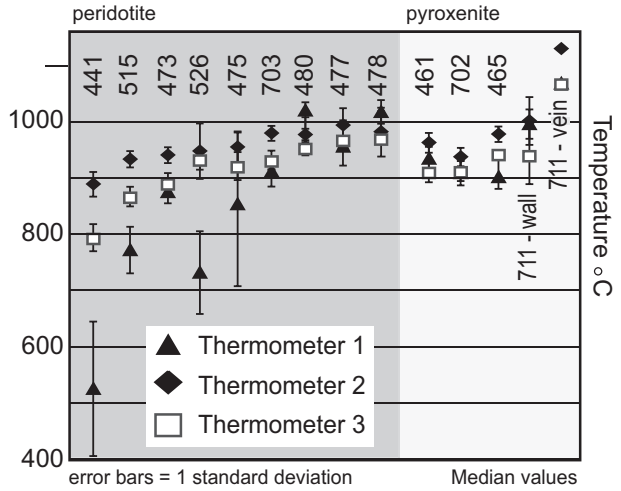

Fig. 6. Thermometry results for Mount Morning peridotite and pyroxenite xenoliths. All sample numbers (e.g. 441) are prefixed with OU78 and relate to sample numbers used in the tables and text. Temperature calculated using the thermometer of Brey & Kohler (1990; Thermometer 1), Putirka (2008; Thermometer 2) or Putirka (2008, Mg# of clinopyroxene >0·75; Thermometer 3).

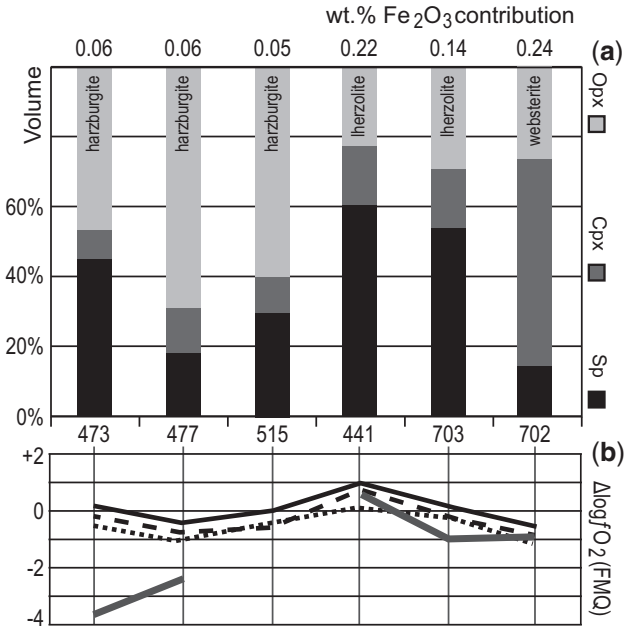

Fig. 7. (a) Relative contribution of Fe_2O_3 wt % from clinopyroxene (Cpx), orthopyroxene (Opx) and spinel (Sp) in each sample used for oxygen fugacity measurements as determined from Mössbauer spectroscopy, chemical composition and modal abundance data. All sample numbers (e.g. 441) are prefixed with OU78 and relate to sample numbers used in (b) and in the tables and text. (b) $\Delta\log fO_2$ calculated using the olivine–orthopyroxene–spinel oxybarometer of (1) Wood *et al.* (1990; continuous line) (2) Ballhaus *et al.* (1991; dashed line) and (3) O'Neill & Wall (1987; dotted line) as updated by H. S. C. O'Neill (personal communication) and the olivine–orthopyroxene–clinopyroxene oxybarometer of Luth & Canil (1993; grey line).

cooling, or disturbed by normal measuring techniques (Wood *et al.*, 1990). The olivine–orthopyroxene–spinel oxybarometer is typically used for specimens equilibrated at shallow upper mantle conditions (Wood, 1991; Woodland *et al.*, 2006; Frost & McCammon, 2008; Herd, 2008). It is controlled by the equilibrium

$$6Fe_2SiO_4 + O_2 = 2Fe^{2+}Fe^{3+}{}_2SO_4 + 6FeSiO_3 \quad (1)$$
$$\text{Ol} = \text{Sp} + \text{Opx}$$

fO_2 was calculated using the oxygen barometer of Wood *et al.* (1990), following the method outlined by Woodland *et al.* (1992), and the results are given in Table 5. The greatest potential for error in equation (1) lies in calculating the activity of magnetite in spinel, $a^{sp}_{Fe_3O_4}$ (Wood, 1991; Herd, 2008); thus the Ballhaus *et al.* (1991) calibration of equation (1) is also included in Table 5. Shown for comparison in Table 5 is the O'Neill & Wall (1987) olivine–orthopyroxene–spinel oxybarometer as updated by H. S. C. O'Neill (personal communication) The updated formulation incorporates a revised SiO_2 activity based on the reaction $Mg_2SiO_4 + SiO_2 = Mg_2Si_2O_6$ calculated from the thermodynamic data of Holland & Powell (1998), and results in a $\Delta\log fO_2$ increase of ~0·5 log units for all of our samples compared with the original formulation). The olivine–orthopyroxene–clinopyroxene oxybarometer of Luth & Canil (1993) was also applied and results are shown in Table 5. Potential errors in the calculation of oxygen fugacity arising from the estimation of pressure (and subsequently temperature) have been minimized by referencing fO_2 to the fayalite–magnetite–quartz (FMQ) buffer, hereafter referred to as $\Delta\log fO_2$.. Furthermore, the errors in the measurement of $Fe^{3+}/\sum Fe$ ratios by Mössbauer spectroscopy are calculated to be less than 0·05, and typically errors of ±0·01 are assumed (Canil & O'Neill, 1996; Woodland *et al.*, 2006). The uncertainties in the oxygen barometers when using Mössbauer spectroscopy are well understood. For example, with errors in temperature of up to 100°C and pressure of 3 kbar, the errors in $\Delta\log fO_2$ are ±0·15 and 0·9 log units, respectively. Combined with analytical uncertainties, the total error in $\Delta\log fO_2$ is ±0·5 log units (Woodland *et al.*, 1992, 2006). The relevant contribution of spinel and pyroxene to $\Delta\log fO_2$ is shown in Fig. 7a and b. Total $\Delta\log fO_2$ of the Mount Morning suite falls between –1 and +1 log units relative to the FMQ buffer as recorded by the olivine–orthopyroxene–spinel oxybarometer (Table 5). A comparison of results from the olivine–orthopyroxene–clinopyroxene oxybarometer with these values shows good correlation between oxybarometers for the lherzolites and websterite, but significantly lower values for the harzburgites (Fig. 7b).

Whole-rock chemistry

Major elements

The majority of peridotite samples follow a primitive mantle depletion trend on a wt % SiO_2 vs MgO/SiO_2 plot, with only orthopyroxenite sample OU78 474 plotting along the orthopyroxene trend and dunite samples plotting along the olivine trend (Fig. 8a). This primitive mantle trend could reflect either melt depletion or

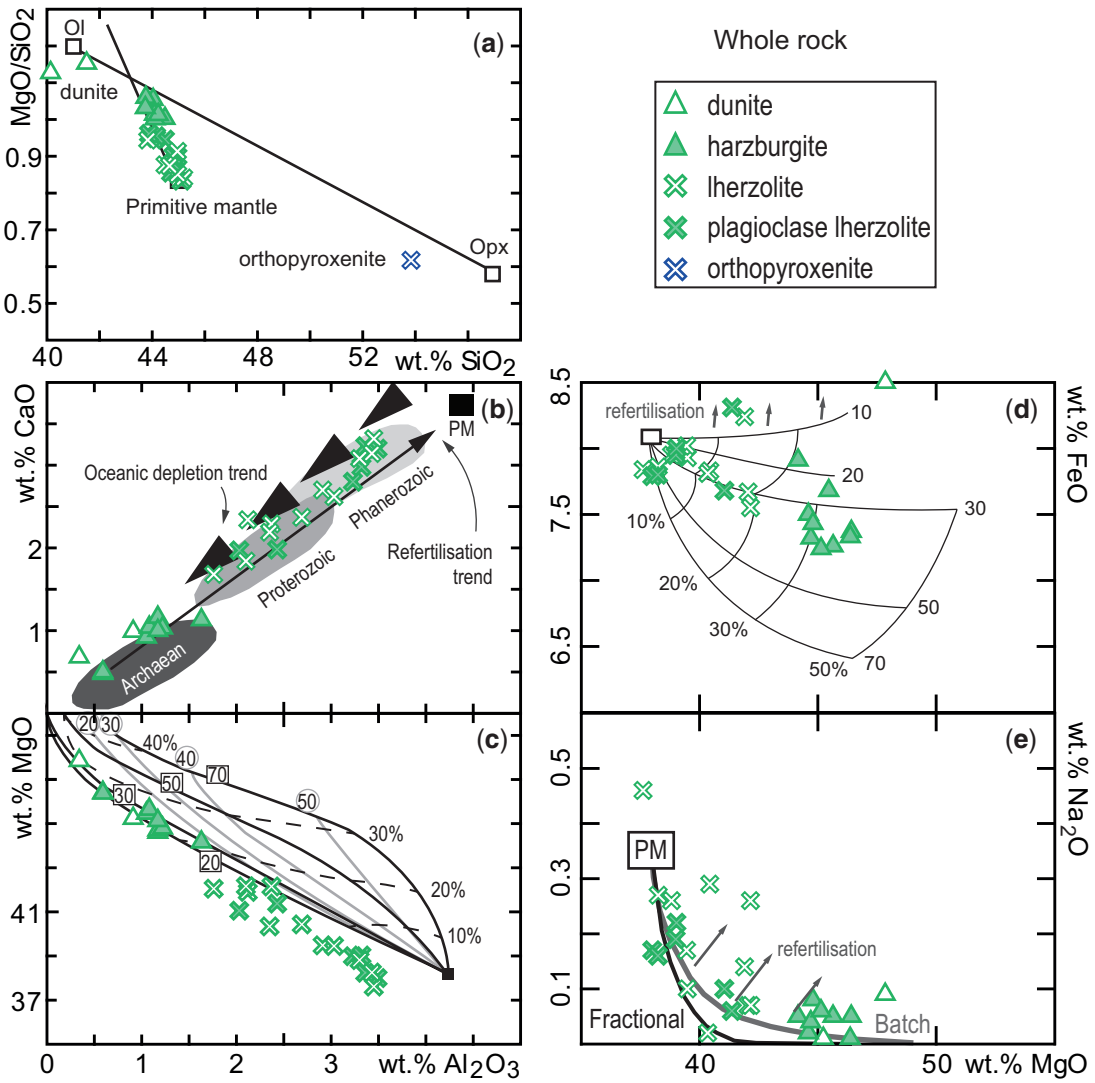

Fig. 8. Major element whole-rock data for Mount Morning peridotite xenoliths. (a) Wt % SiO_2 vs MgO/SiO_2. The residue trend for primitive mantle melting and a mixing trend between olivine (Ol) and orthopyroxene (Opx) are after Walter (1998). (b) Wt % Al_2O_3 vs CaO. The fine, long arrow depicts a refertilization trend after Tang *et al.* (2013) that runs in the opposite direction to the oceanic depletion trend of Boyd (1989). Primitive mantle (PM) is after McDonough & Sun (1995) and the mantle age fields are after O'Reilly *et al.* (2001). (c) Wt % Al_2O_3 vs MgO showing the fertile peridotite fractional melting grid of Herzberg (2004) for comparison. The bold black lines labelled with squares are for different initial melting pressures (kbar), the dashed lines represent melt fractions and the grey lines labelled with circles are final melting pressures (kbar). (d) Wt % MgO vs FeO showing the melting grid of Walter (2003) as a function of pressure (kbar) and batch melt extraction (%). (e) Wt % MgO vs Na_2O with model curves after Lee *et al.* (2011) for batch (isobaric; 20 kbar; grey line) and fractional (polybaric; 25 kbar; black line) melting. Grey arrows in (d) and (e) indicate refertilization.

refertilization. For example, the peridotite data could be interpreted to plot along both the oceanic depletion and refertilization trends (opposite directions) on a wt % Al_2O_3 vs CaO plot (Fig. 8b). In general, dunite and harzburgite samples have low values of wt % Al_2O_3 and CaO and overlap with the field of Archaean mantle [mantle age fields follow O'Reilly *et al.* (2001)], whereas the lherzolite samples have higher values of wt % Al_2O_3 and CaO and overlap with fields of younger aged mantle (Fig. 8b). The peridotite data define a linear trend on a plot of wt % Al_2O_3 vs MgO, in which the lherzolite samples tend to plot at or below the 20 kbar initial melting pressure line at melt fractions $\leq$0·2 and the dunite and harzburgite samples plot between the 20 and 30 kbar initial melting pressure lines at melt fractions between 0·2 and 0·3 (Fig. 8c). There is a degree of scatter to the data on a wt % MgO vs FeO plot, with the lherzolite data plotting at melt fractions $<$20%, harzburgite data plotting at $>$20% and most data plotting between initial melting pressures of 20 and $<$50 kbar (Fig. 8d). There is a negative and non-linear relationship to much of the data on a wt % MgO vs Na_2O plot, with some samples showing excess Na_2O (Fig. 8e); these are discussed further below.

The pyroxenite xenoliths have a wide range of wt % MgO values (13·41–33·22) that are intermediate

between peridotite xenolith values and those for primitive Mount Morning volcanic rocks (Fig. 9). The pyroxenites show a negative correlation of wt % MgO with CaO, TiO_2 and Al_2O_3 abundance (Fig. 9a, b and d) and with the modal abundance of clinopyroxene (not shown). There is a positive correlation between wt % MgO and FeO (Fig. 9c) and NiO contents (not shown).

Trace elements

In general, the whole-rock mantle-normalized multi-element pattern for dunite is characterized by decreasing enrichment, relative to primitive mantle, with increasing element compatibility (Fig. 10a). Dunite has a negative Pb anomaly, positive Nb anomaly and a pattern of incompatible trace element enrichment similar to average subcontinental lithospheric mantle (SCLM) and to typical HIMU ocean island basalt (OIB) (High-μ: enriched in ^{206}Pb and ^{208}Pb and relatively depleted in $^{87}Sr/^{86}Sr$), although at lower overall abundances [particularly the heavy rare earth elements (HREE); Fig. 10a]. The harzburgites have a positive Pb anomaly and either a positive or negative Ti anomaly (Fig. 10b), with trace element abundances depleted relative to average SCLM. The lherzolite and plagioclase lherzolite mantle-normalized multi-element plots are, in general, characterized by an increasing depletion, relative to primitive mantle, with increasing element incompatibility that is comparable with depleted MORB mantle (DMM) and normal mid-ocean ridge basalt (N-MORB), although at lower overall abundances than the latter (Fig. 10c and d). The spinel and plagioclase lherzolite trace element patterns show positive Pb anomalies and typically a weakly negative Ti anomaly (Fig. 10c and d). Uranium and Th are strongly fractionated in the harzburgites and lherzolites [mean $(U/Th)_n = 16{\cdot}2$] and Zr and Sm are moderately fractionated in many of the peridotite xenoliths [mean $(Zr/Sm)_n = 1{\cdot}7$].

The rare earth element (REE) abundance in Mount Morning xenoliths varies with their relative mineralogy. For example, mantle-normalized REE plots for the dunites (Supplementary Data Fig. A5) show enrichments of light REE (LREE) relative to middle REE (MREE) and heavy REE (HREE) [$(La/Lu)_n = 9{\cdot}73–1{\cdot}19$]. The lherzolites show depletions of LREE relative to MREE and HREE [$(La/Lu)_n = 0{\cdot}60–0{\cdot}06$; median value 0·24; excluding sample OU78 441) and harzburgites have both minor LREE enrichments and depletions intermediate between the lherzolite and dunite patterns [$(La/Lu)_n = 0{\cdot}27–1{\cdot}21$; Supplementary Data Fig. A5). A notable exception to

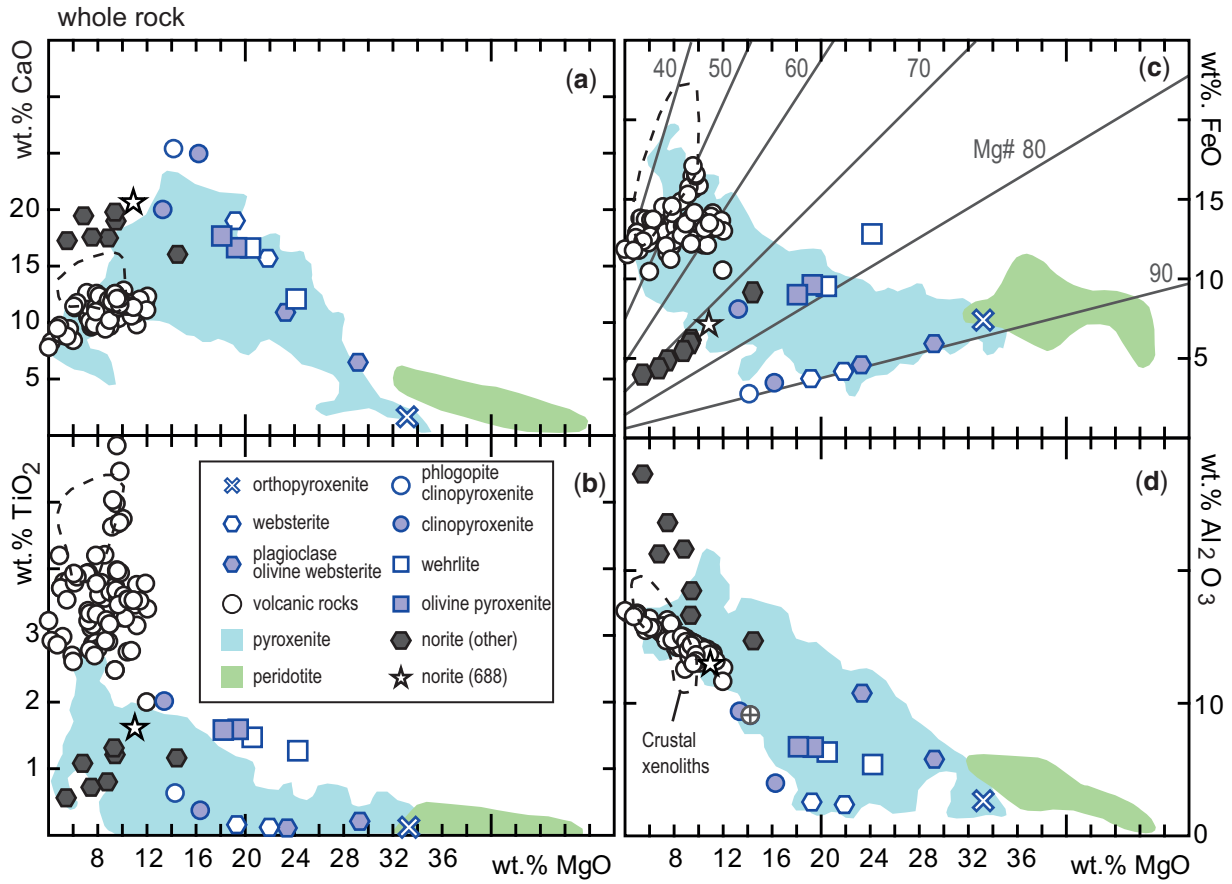

Fig. 9. Major element whole-rock data for Mount Morning pyroxenite xenoliths. Shown for comparison are fields of pyroxenites (Lambart *et al.*, 2009, 2013) and peridotites (Lambart *et al.*, 2013). The volcanic rock data are for Mount Morning from Martin *et al.* (2013). The norite data are also for Mount Morning from Martin *et al.* (2013; sample OU78 688) and Martin *et al.* (2015). The crustal xenolith field (dashed line) outlines other mafic crustal xenolith compositions from Mount Morning (Martin, 2009).

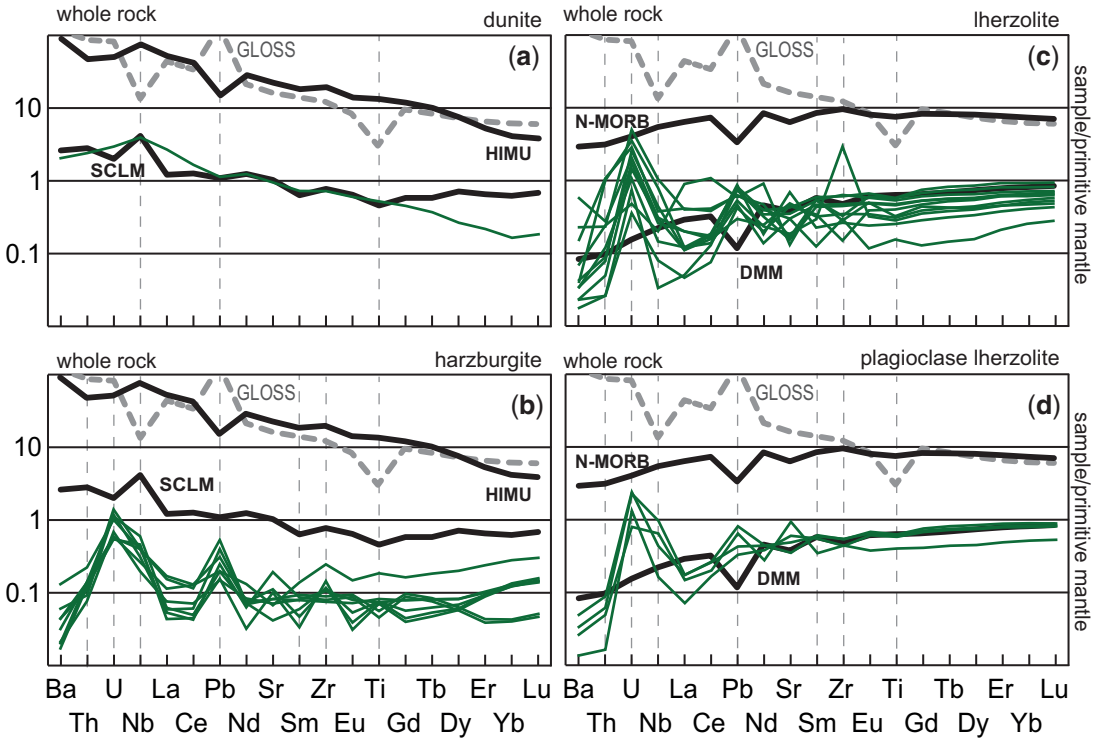

Fig. 10. Peridotite whole-rock multi-element patterns normalized to the primitive mantle values of McDonough & Sun (1995); Mount Morning data indicated by fine green lines. (a) Dunite. (b) Harzburgite. (c) Lherzolite. (d) Plagioclase lherzolite. SCLM, subcontinental lithospheric mantle (McDonough, 1990); DMM, depleted MORB-source mantle (Workman & Hart, 2005). The HIMU pattern is for Mangaia, Austral Islands [sample M-11 of Woodhead (1996)]. N-MORB, normal mid-ocean ridge basalt (Gale *et al.*, 2013); GLOSS, average subducted sediment (Plank & Langmuir, 1998).

this general trend is lherzolite specimen OU78 441, which has enriched LREE relative to the MREE and HREE [$(La/Lu)_n = 1{\cdot}86$; Fig. A5]. The majority of the Mount Morning peridotite xenoliths have REE contents that are depleted relative to primitive mantle; exceptions are dunite sample OU78 443 and lherzolite sample OU78 441.

On a primitive mantle-normalized multi-element plot the orthopyroxenite shows increasing depletion, relative to primitive mantle, with increasing element compatibility and positive Ti and Nd anomalies (Fig. 11a). In general, wehrlite, olivine clinopyroxenite and clinopyroxenite patterns are very similar to those of N-MORB (except for the HREE; Fig. 11b). The olivine clinopyroxenites and clinopyroxenites studied have negative Nb, Pb and Ti anomalies with enrichment in trace elements comparable with average subducted sediment (global subducting sediment; GLOSS) and norite (Fig. 11c). The websterites have trace element enrichment patterns similar to DMM, plus a negative Ti anomaly, and two samples have a weakly positive (Ce–)Pb anomaly (Fig. 11d).

On primitive mantle-normalized REE plots (Supplementary Data Fig. A6) the plagioclase-bearing olivine websterite patterns have LREE values that are depleted relative to the MREE and HREE [$(La/Lu)_n = 0{\cdot}46$–$0{\cdot}39$]; all other pyroxenites have LREE values elevated relative to MREE and HREE [$(La/Lu)_n = 1{\cdot}46$–$4{\cdot}71$]. One clinopyroxenite specimen (OU78 691) and the phlogopite-bearing clinopyroxenite have negative Eu anomalies ($Eu^* = 0{\cdot}57$–$0{\cdot}58$), where $Eu^* = Eu_n/10^{\chi}$, $\chi = [\log(Sm_n) + \log(Gd_n)]/2$ and subscript n indicates normalized to the primitive mantle values of McDonough & Sun (1995). There is a weak, negative Eu anomaly in the REE patterns of the websterite samples ($Eu^* = 0{\cdot}88$) and a weak, positive Eu anomaly in the plagioclase-bearing olivine websterites ($Eu^* = 1{\cdot}09$–$1{\cdot}17$; Fig. A6).

DISCUSSION

Oxygen fugacity

The $\Delta\log fO_2$ results from the three olivine–orthopyroxene–spinel oxybarometers agree with each other to within one log unit for all samples (Table 5). The oxygen fugacities of the Mount Morning xenoliths vary from FMQ – 1 to FMQ for all samples except OU78 441 (which is +0·8). This range is similar to the results of Perinelli *et al.* (2012), who also used Mössbauer spectroscopy to determine $Fe^{3+}/\sum Fe$ in spinel and thus the redox state of mantle xenoliths from Northern Victoria Land. They obtained $\Delta\log fO_2$ values between –0·2 and –1·5 for spinel peridotite specimens. Bonadiman *et al.* (2014) reported $\Delta\log fO_2$ values from anhydrous olivine–orthopyroxene–spinel equilibria of between –0·30 and –1·98, which suggests a relatively consistent oxygen fugacity for the anhydrous shallow, rifted, spinel peridotite mantle beneath Victoria Land with a median value of $-1{\cdot}0 \pm 0{\cdot}1$ $\Delta\log fO_2$ ($n = 20$; range –1·98 to –0·2;

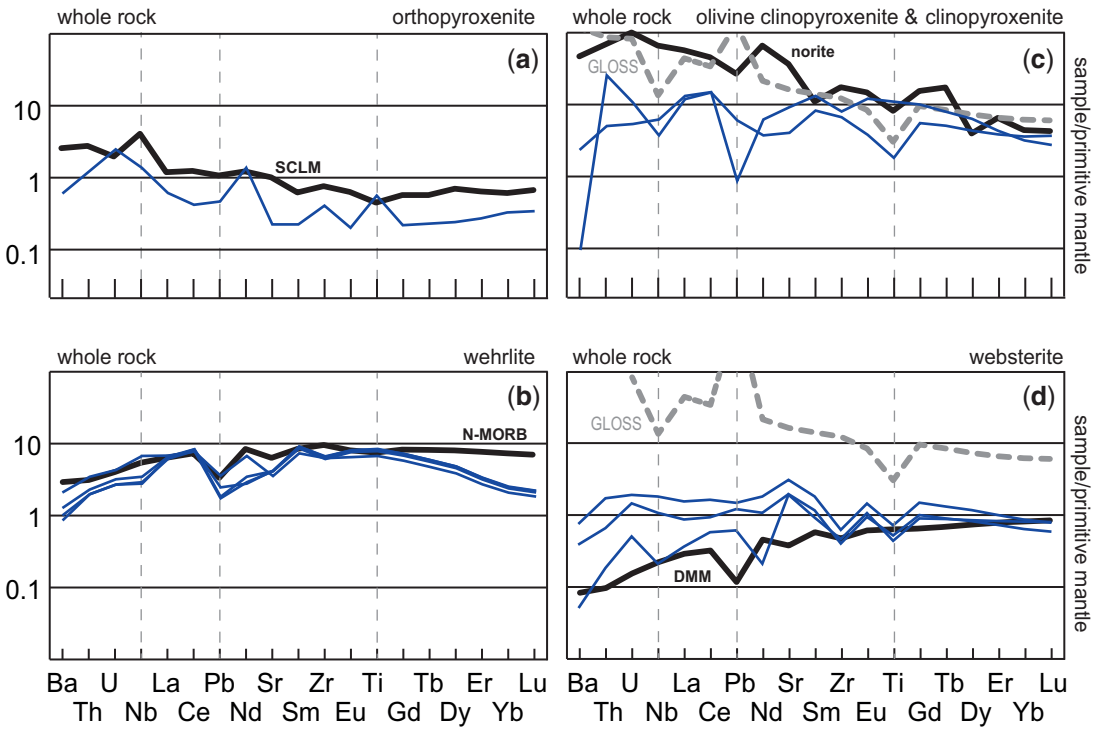

Fig. 11. Pyroxenite whole-rock multi-element patterns normalized to the primitive mantle values of McDonough & Sun (1995); Mount Morning data indicated by fine blue lines. (a) Orthopyroxenite. (b) Wehrlite. (c) Clinopyroxenite and olivine clinopyroxenite. (d) Websterite. Reference patterns are the same as in Figs 9 and 10.

error = 1σ). Bonadiman *et al.* (2014) also reported the oxygen fugacity of amphibole-bearing mantle xenoliths, based on oxy-amphibole equilibrium; these give Δlog fO_2 values between –1·32 and –2·52. Figure 12 shows fO_2 data from xenoliths in continental rifts and various tectonic settings from around the world. To facilitate direct comparison, all equilibration temperatures were re-calculated using Thermometer 3 of Putirka (2008). If $Fe^{3+}/\sum Fe$ ratios were previously calculated assuming perfect stoichiometry, then they were re-calculated using the method of Finger (1972). Finally, all Δlog fO_2 data were re-calculated using the oxybarometer of Ballhaus *et al.* (1991). The re-calculated values are very similar (±1σ) to the originally reported values, but the re-calculations ensure that all the data being compared are standardized. Whereas the range of fO_2 varies by >4 log units (–4·1 to 0·5) for the xenolith data from the rift settings, the median values are within 1·1 log units of one another (–1·6 to –0·5) and all data considered together give a global median rift value of –0·9 ± 0·1 Δlog fO_2 (Fig. 12). This value is within the range of Mount Morning fO_2 (–1 to 0) and is within 0·1 log units of the median value for Victoria Land (–1·0).

The Δlog fO_2 values calculated from the olivine–orthopyroxene–clinopyroxene oxybarometer are 2–3 log units below values from the olivine–orthopyroxene–spinel oxybarometers for the harzburgites (Fig. 7b). This discrepancy probably arises from the low modal abundance of clinopyroxene in the harzburgites in which a small degree of melt interaction could decrease the $Fe^{3+}/\Sigma Fe$ ratio substantially through preferential partitioning of Fe^{3+} into the melt. The Fe^{2+}/Mg exchange between phases was not substantially influenced, however, as seen from the consistent results obtained from the two-pyroxene and olivine–spinel thermometers.

The Δlog fO_2 of lherzolite OU78 441 is roughly one log unit higher than for other samples from the Mount Morning suite (Fig. 7b; grey star in Fig. 12), which may indicate an effect owing to metasomatism. Specimen OU78 441 is the only lherzolite sample with an equant granuloblastic texture, suggesting significant recrystallization; it has an anomalously low equilibration pressure of 3 kbar and is the only lherzolite specimen with a LREE-enriched REE pattern relative to the MREEs and HREEs (Supplementary Data Fig. A5). These observations suggest that OU78 441 has experienced a high degree of metasomatism relative to other studied specimens from Mount Morning and has probably undergone open-system behaviour, as suggested by the poor agreement between barometers for this sample. Its Δlog fO_2 value at +0·8 overlaps with the range expected for xenoliths from subduction settings (Fig. 12).

Geothermobarometry

The pressures and temperatures calculated for the Mount Morning xenolith suite are plotted in Fig. 13 and compared with geotherms calculated for a dynamic rift setting such as that of Northern Victoria and Southern Victoria Land. The majority of data are coincident with the Southern Victoria Land (SVL) geotherm calculated by Berg *et al.* (1989) using petrological data for lower

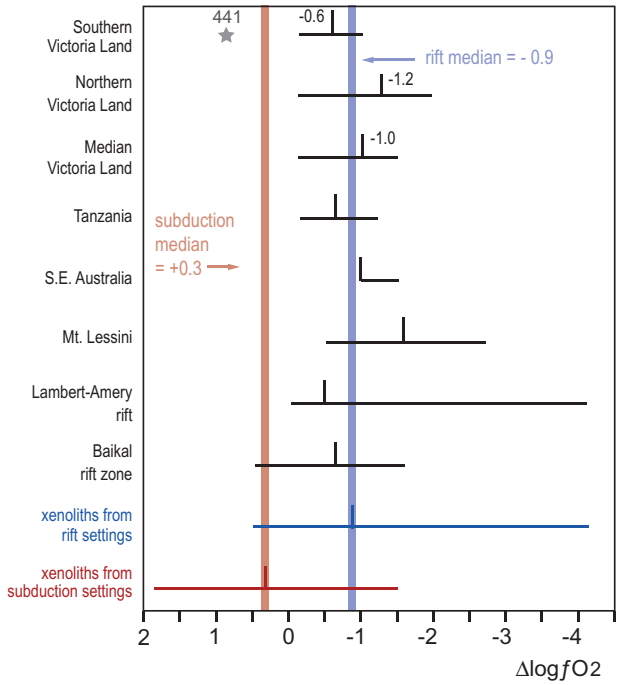

Fig. 12. Oxygen fugacity median (vertical tick) and range (horizontal line) values calculated for spinel peridotite-facies rocks from continental rift settings. The references used are as follows: xenoliths from (continental) rift settings, this study; Baikal rift zone, Russia, Ionov & Wood (1992); Lambert–Amery rift, Antarctica, Foley *et al.* (2006); Mt. Lessini, Italy, Siena & Coltorti (1993); SE Australia and Tanzania, Canil *et al.* (1994) and Canil & O'Neill (1996); Northern Victoria Land, Perinelli *et al.* (2012) and Bonadiman *et al.* (2014); Southern Victoria Land, this study. The range and median value (–0·9 Δlog fO_2) for all these localities combined is also shown (xenoliths from rift settings) and compared with xenoliths from subduction settings [Frost & McCammon (2008) and references therein]. The median value for all Victoria Land data is –1·0 Δlog fO_2.

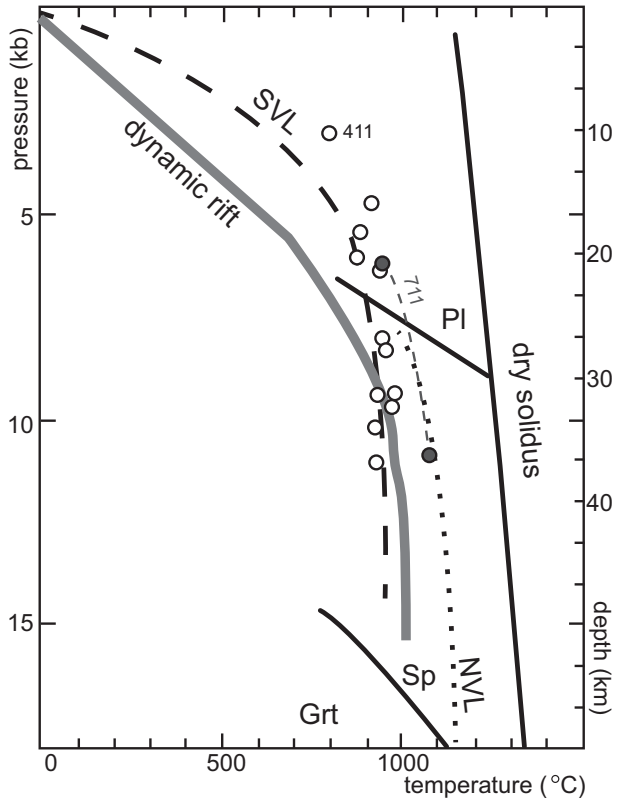

Fig. 13. Thermobarometry of Mount Morning xenoliths using the barometer of Putirka (2008) and the Mg# 75 in clinopyroxene thermometer, also of Putirka (2008; Thermometer 3). The Mount Morning data (open circles) mainly follow the Southern Victoria Land (SVL) geotherm of Berg *et al.* (1989). Values from composite xenolith OU78 711 (grey filled circles) are slightly hotter than for the other Mount Morning samples and plot along the Northern Victoria Land (NVL) geotherm of Perinelli *et al.* (2006). For comparison an idealized dynamic rift geotherm is shown (Chapman, 1986). The spinel (Sp)–garnet (Grt) transition curve, plagioclase (Pl)-out boundary and dry solidus boundary are from Borghini *et al.* (2011).

crustal granulites from the region. One exception is the vein in composite sample OU78 711 for which the calculated temperature of 1068°C is 125°C hotter than the temperature calculated for the host peridotite (Figs 6 and 13). The trend defined between the host peridotite and vein temperatures is similar to that observed for temperatures calculated for core and rim pairs in xenoliths from the Pipecleaner Glacier (Martin *et al.*, 2014), and overlaps, within error, the geotherm defined for Northern Victoria Land (NVL). Martin *et al.* (2014) attributed the high temperatures calculated for the Pipecleaner Glacier specimens to trapped, syn-rift melts, and a similar explanation is appropriate for the veined peridotite sample described here. Wörner & Zipfel (1996) have also described the superimposition of hot peridotite bodies on cold uppermost mantle in Northern Victoria Land. The high temperatures recorded in the pyroxenite vein reflect increased crystallization temperatures associated with syn-rift melts. Low-pressure and -temperature lherzolite sample OU78 411 plots off the defined Southern Victoria Land geotherm (Fig. 13); however, the poor agreement between thermometers for this sample (Fig. 6) suggests that less emphasis should be placed upon this datum. The Berg *et al.* (1989) geotherm remains the most appropriate one for Southern Victoria Land.

Origin of peridotite xenoliths

Peridotite melt depletion

Increasing olivine mode (Table 1; Fig. 2), an inverse relationship between olivine Mg# and spinel Cr# (Fig. 5a), an inverse relationship between wt % MgO and Al_2O_3 in clinopyroxene (Fig. 4a) and orthopyroxene (Fig. 4b), a positive trend on a whole-rock wt % Al_2O_3 vs CaO plot (Fig. 8b) and whole-rock LREE depletion (relative to MREE and HREE) (Fig. 10; Supplementary Data Fig. A5) are all classically interpreted as evidence for melt depletion in peridotite xenoliths (e.g. Johnson *et al.*, 1990; Niu, 2004) and this interpretation is also appropriate here. Based upon melting grids on the whole-rock plots, the degree of melt depletion is estimated to be between 20 and 30% for the harzburgites and <20% for the lherzolites (Fig. 8c–e). This is in general agreement with melt models shown on a whole-rock ppm Yb vs Dy/Yb

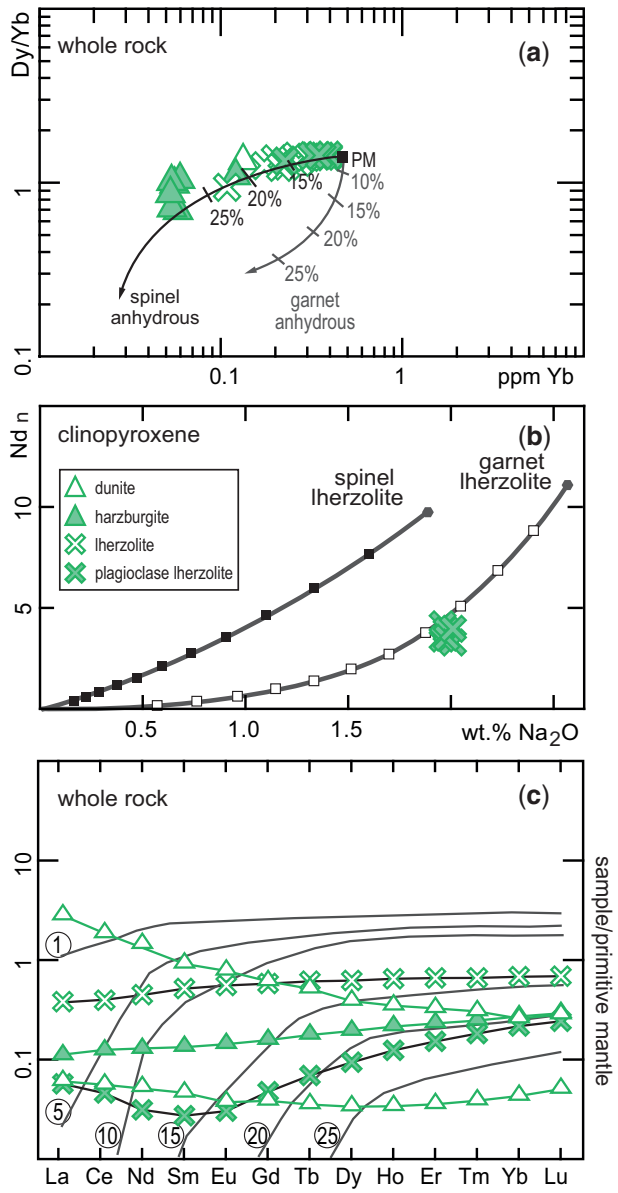

Fig. 14. Whole-rock and mineral trace element and REE melt models for peridotite xenoliths. Full model details are given in Supplementary Data Appendix 1. (a) Yb (ppm) vs Dy/Yb. Fractional melting models assume the primitive mantle (PM) starting composition of McDonough & Sun (1995) and the melting modes and partition coefficients of Johnson *et al.* (1990) for anhydrous spinel facies (black line) and anhydrous garnet facies (grey line) conditions, following the method of Riches & Rogers (2011). (b) Wt % Na_2O vs Nd_n plot showing the high-sodium group of clinopyroxene analyses within the plagioclase lherzolite xenoliths (as shown in Fig. 4c). Neodymium is normalized (n) to primitive mantle (McDonough & Sun, 1995). Two fractional melting models are calculated assuming a primitive upper mantle source (McDonough & Sun, 1995): a fertile spinel peridotite (assuming $D^{cpx/1} = 0{\cdot}3$) and a garnet peridotite (assuming $D^{cpx/1} = 0{\cdot}5$), after Müntener *et al.* (2010). The primitive mantle mineral modes are from Johnson (1998), spinel melt proportions from Kinzler (1997), garnet melt proportions from Walter (1998), and the partition coefficient for Nd ($D_{Nd}^{cpx/1}$) is 0·2. (See the Supplementary Data Appendix 1 for details.) (c) Whole-rock model REE patterns (fine lines) for the spinel facies using element distribution coefficients from Kelemen *et al.* (1993) and Liu *et al.* (2012) and melting modes from Kinzler (1997). The circled numbers indicate the percentage of melt depletion.

diagram in Fig. 14a. The Mount Morning data plot along the anhydrous, spinel-facies melting curve at melt fractions <25% for lherzolite and >20% for harzburgite (Fig. 14a). The majority of the Mount Morning samples overlap with the melting curve defined for the spinel stability field of the mantle (Fig. 14a). However, the major element mineral data suggest a slightly different story. The pyroxene (Fig. 4a and b) and olivine Mg# vs spinel Cr# (Fig. 5a) plots indicate that harzburgite and spinel lherzolite have undergone similar degrees of melt depletion and both have undergone a higher degree of melt depletion than recorded by the plagioclase lherzolite mineral data. The discrepancy between whole-rock and mineral data may be due to refertilization as discussed below.

The reasons for variable clinopyroxene Na abundances within the Mount Morning plagioclase peridotite xenoliths were investigated. In basaltic melts Na abundance is controlled by the degree of melting; a relationship that leads to significant Na variation in MORB (Langmuir *et al.*, 1993). At low pressures the compatibility of Na is similar to that of Nd (Blundy *et al.*, 1995), but the breakdown of this relationship at higher pressures leads to decreasing Nd/Na ratios in residual clinopyroxene in the garnet stability field of the mantle and relatively constant ratios in the spinel stability field (Müntener *et al.*, 2010). Relatively Na-rich and Nd-poor clinopyroxenes may thus reflect high-pressure partial melting. An alternative hypothesis is that Na-rich clinopyroxene forms by refertilization of mantle within the spinel stability field (e.g. Le Roux *et al.*, 2007). To distinguish between these two alternatives, following Müntener *et al.* (2010), melt models for spinel-facies conditions and garnet-facies conditions in the mantle were calculated and the high-sodium group of clinopyroxenes from Mount Morning were plotted for comparison (Fig. 14b). The high-sodium group of clinopyroxenes are consistent with the garnet lherzolite melting model shown in Fig. 14b. The Na contents in clinopyroxene from other Mount Morning xenoliths are lower than those of the high-sodium group of clinopyroxenes and most probably record partial melting in the spinel facies of the mantle, in agreement with the whole-rock melt models shown in Fig. 14a.

Peridotite refertilization

Lherzolite xenoliths are usually considered to be relativey fertile mantle samples, but more recent work suggests that they can be the refertilized products of previously depleted harzburgite (e.g. Griffin *et al.*, 2009; Upton *et al.*, 2011). Martin *et al.* (2014) have shown that Mount Morning plagioclase lherzolite xenoliths have undergone a degree of refertilization and, based on seven samples, Martin *et al.* (2013) also showed that some Mount Morning harzburgite xenoliths have been affected by refertilization events. The present study is based on a much more comprehensive dataset. Using the method of Larazov *et al.* (2012), the REE patterns of melt depletion have been modelled assuming

fractional, non-modal melting of primitive mantle, the distribution coefficients of Kelemen *et al.* (1998) and Lui *et al.* (2012), and the melting modes of Kinzler (1997) (see Supplementary Data Appendix 1 for model details). The results are plotted in Fig. 14c. When compared with the whole-rock REE patterns of the Mount Morning peridotites, the REE models match reasonably well the MREE to HREE values at 10–20% melt extraction for the lherzolite specimens and *c.* 20% to >25% melt extraction for the harzburgite specimens (Fig. 14c). The melt depletion models, however, fail to match the LREE contents of the Mount Morning xenoliths, a pattern that is commonly attributed to melt depletion and then subsequent re-enrichment (e.g. Müntener *et al.*, 2004; Niu, 2004). Figure 8e shows Mount Morning peridotite whole-rock data in terms of wt % Na_2O vs MgO, plotting along a non-linear trend consistent with batch (and/or fractional) melting models. There are also a number of samples that have high wt % Na_2O (Fig. 8e) that could be explained by binary mixing between a basaltic component and depleted peridotite, as Na is incompatible, and Mg compatible, in melt residues (Lee *et al.*, 2011). Some samples can also be shown to have high wt % FeO for a given MgO content (Fig. 8d). Thus there appears to have been addition of REE and major elements to a number of the Mount Morning peridotite xenoliths, consistent with refertilization. The major element mineral chemistry of the spinel lherzolites is melt-depleted to a degree comparable with that of the harzburgite, yet modelling of the spinel lherzolite whole-rock data suggests that they have undergone less melt depletion than the whole-rock harzburgites. This can be explained by refertilization of the spinel lherzolites.

The nature of the refertilizing melt can be evaluated using the chemical data and previously published isotopic constraints. The dunite and harzburgite whole-rock trace element patterns on normalized multi-element plots are, in general, comparable with those of SCLM, whereas the lherzolite patterns are comparable with DMM. Dunite specimen OU78 443 plots within the HIMU OIB field defined on a Ba/Nb vs Ba/La diagram (Supplementary Data Fig. A8) and the dunite and harzburgite xenoliths plot close to the HIMU field on a $^{87}Sr/^{86}Sr$ vs $^{143}Nd/^{144}Nd$ diagram (Fig. 15a and b), although with a radiogenic Pb isotope composition less than pure end-member HIMU (Martin *et al.*, 2013). The trace element and isotopic characteristics of dunite and harzburgite xenoliths are similar to typical SCLM (Fig. 10a and b), peridotites from Southern and Northern Victoria Land, and the mantle source characteristics proposed for Cenozoic volcanic rocks from Victoria Land and Zealandia (e.g. Timm *et al.*, 2010; Martin *et al.*, 2013; Scott *et al.*, 2014; Fig. 15a and b). These common characteristics are frequently explained by mixing between depleted mantle (DMM) and a second component that may be from the crust (e.g. Stracke, 2012) or, more commonly for the DAMP region, is interpreted as a HIMU-like component. This latter explanation is reasonable given that several eruptive

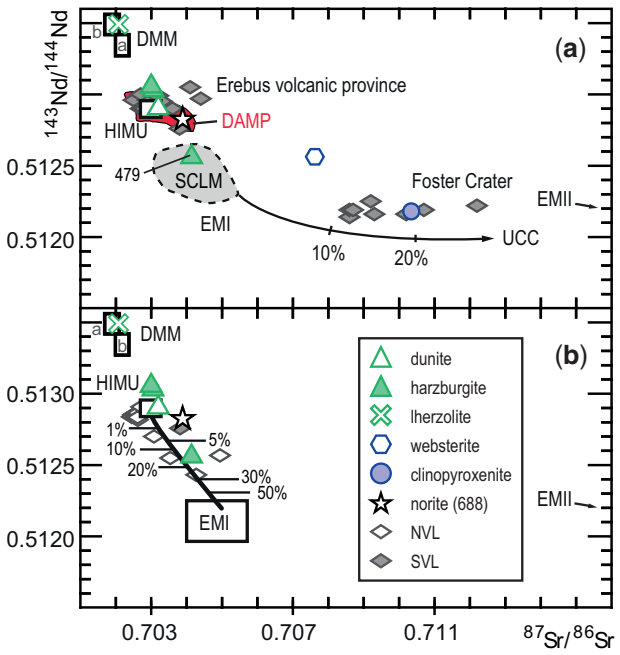

Fig. 15. Variation of $^{87}Sr/^{86}Sr$ vs $^{143}Nd/^{144}Nd$ for whole-rocks and clinopyroxene separates for various Victoria Land samples compared with the end-member mantle reservoirs of Zindler & Hart (1986). (a) Southern Victoria Land (SVL) data for Foster Crater and Erebus volcanic province from McGibbon (1991) and for Mount Morning from Martin *et al.* (2013). The diffuse alkaline magmatic province (DAMP) field is after Martin *et al.* (2013, and references therein). The dashed line shows typical SCLM values from Jourdan *et al.* (2007). The black line shows a mixing curve calculated between SCLM and upper continental crust (UCC) using the values and equations reported by Jourdan *et al.* (2007, and references therein). SCLM: ($^{87}Sr/^{86}Sr$) = 0·7043, 50 ppm Sr; ($^{142}Nd/^{144}Nd$) = 0·51244, 2 ppm Nd; UCC: ($^{87}Sr/^{86}Sr$) = 0·73847, 159 ppm Sr; ($^{142}Nd/^{144}Nd$) = 0·511800, 26 ppm Nd. The lherzolite plots in the N-MORB depleted mantle field (DMMb). Reservoir DMMa = E-MORB. (b) Northern Victoria Land (NVL) data are from Melchiorre *et al.* (2011) and Perinelli *et al.* (2011). The mixing curve between HIMU and EMI uses the end-member compositions reported by Rolland *et al.* (2009, and references therein) and the equations of Faure (1986), where the following values apply: HIMU: ($^{87}Sr/^{86}Sr$) = 0·703, 120 ppm Sr; ($^{142}Nd/^{144}Nd$) = 0·51285, 6·5 ppm Nd; EMI: ($^{87}Sr/^{86}Sr$) = 0·705, 513 ppm Sr; ($^{142}Nd/^{144}Nd$) = 0·5122, 33 ppm Nd; EMII: ($^{87}Sr/^{86}Sr$) = 0·71682, 218 ppm Sr; ($^{143}Nd/^{144}Nd$) = 051216, 34 ppm Nd.

centres in the Victoria Land and Zealandia regions, including Mount Erebus, which is <100 km distant from Mount Morning, are generally accepted to have a HIMU-like component in their mantle source (Panter *et al.*, 2006; Stracke, 2012; Scott *et al.*, 2013).

A degree of alkalic melt refertilization has been identified in plagioclase lherzolite xenoliths from White Island and Pipecleaner Glacier in Southern Victoria Land (Martin *et al.*, 2014). To date, such refertilization has not been identified in the Mount Morning plagioclase lherzolite xenoliths, but the LREE-enriched trace element characteristics of the dunite and lherzolite xenoliths described here (Fig. 10a and Supplementary Data A4) indicate that this may be a possibility. Models shown in Fig. 16a illustrate the effects of addition of an LREE-enriched (alkalic) melt to a depleted mantle

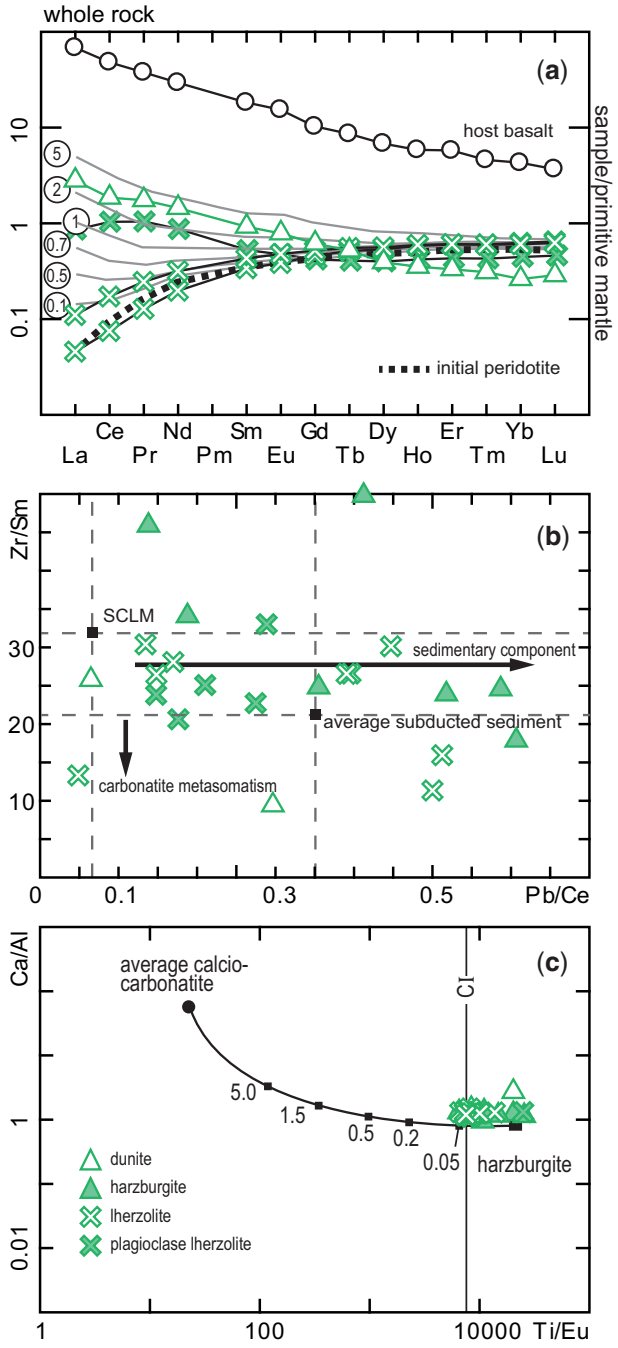

Fig. 16. Whole-rock trace element abundance patterns and ratios and major element ratios for Mount Morning peridotite xenoliths and comparisons with models for different types of melt–rock reaction. (a) Whole-rock REE patterns normalized to the primitive mantle values of McDonough & Sun (1995). The host basalt is Mount Morning volcanic rock sample OU78 540 from Martin *et al.* (2013) and the initial peridotite (bold black dotted line) is equivalent to lherzolite specimen OU78 521. The grey lines show the product of mixing the host basalt composition with the initial peridotite composition in wt % melt proportions (circled values) using the mineral–melt partition coefficients and equations of Ionov *et al.* (2002). The model details are given in Supplementary Data Appendix 1. (b) Whole-rock Pb/Ce vs Zr/Sm. The value of average subducted sediment (GLOSS) is from Plank & Langmuir (1998) and that of subcontinental lithospheric mantle (SCLM) from McDonough (1990). Values of Pb/Ce > SCLM have been argued to suggest a sedimentary component (Hofmann, 2004; Jackson *et al.*, 2007; White, 2010), and subchondritic (McDonough & Sun, 1995) Zr/Sm values have been used to suggest carbonatite metasomatism (Pfänder *et al.*, 2012). (c) Whole-rock log Ti/Eu vs log Ca/Al. The mixing curve between harzburgite and average calcio-carbonatite is from Rudnick *et al.* (1993). The subchondritic (Cl; McDonough & Sun, 1995) Ti/Eu data can be explained by the addition of <0·1 wt % carbonatite.

composition. Dunite sample OU78 443 can be explained by the addition of between 2 and 5 wt % alkalic melt and some lherzolite specimens are modelled reasonably well by up to 1 wt % addition of an alkalic melt (Fig. 16a). Martin *et al.* (2014) have shown that the trace element patterns of clinopyroxene from the plagioclase lherzolite are comparable with those of N-MORB (Supplementary Data Fig. A7), similar to the whole-rock mantle-normalized multi-element patterns shown in Fig. 10c and d, and this has been used to imply that the (spinel) lherzolite xenoliths have also undergone a degree of refertilization by N-MORB melts. Lherzolite sample OU78 703 plots in the DMMb field (N-MORB field) on the Sr vs Nd isotope diagram shown in Fig. 15. Martin *et al.* (2014) have used modelling to argue that the plagioclase lherzolite clinopyroxene multi-element pattern is consistent with up to 6 wt % addition of an N-MORB melt and a similar degree of refertilization is inferred here for all the Mount Morning lherzolite xenoliths.

Peridotite metasomatism

In Mount Morning xenoliths, rare amphibole grains in plagioclase lherzolite specimen OU78 475 and secondary clinopyroxene and oikocrysts of spinel that occur in some lherzolite specimens provide textural evidence for some degree of melt–rock reaction. Furthermore, some of the olivine, clinopyroxene and spinel mineral chemistry trends (Figs 4 and 5) can be interpreted to reflect metasomatism, as has been suggested for Northern Victoria Land mantle xenoliths (e.g. Perinelli *et al.*, 2008). Several aspects of the whole-rock mantle-normalized multi-element plots (Fig. 10), such as strongly positive Pb anomalies and negative Ti anomalies, remain difficult to reconcile by processes of melt depletion and refertilization alone. These relative Pb enrichments and Ti depletions are similar to those observed in average subducted sediments (e.g. Plank & Langmuir, 1998) and in subduction-related volcanic rocks (e.g. Pearce, 1982; McCulloch & Gamble, 1991; Price *et al.*, 1992); this could be an indication that a component of subduction-related fluid has affected the peridotite samples (Hofmann, 2004; Jackson *et al.*, 2007). Average subducted sediment (GLOSS; Plank & Langmuir, 1998), relative to mafic melt, exhibits significant enrichment in Pb and depletions in Ti and Nb. In Fig. 16b where samples have values of Pb/Ce > 0·2 this most probably reflects a sedimentary-like component metasomatizing the Mount Morning peridotites (e.g. White, 2010). On the $^{87}Sr/^{86}Sr$ vs $^{143}Nd/^{144}Nd$ plot

(Fig. 15b) one group of samples overlaps with the area defined for HIMU, with some deviation towards EMI (Enriched Mantle I = low $^{143}Nd/^{144}Nd$, low $^{87}Sr/^{86}Sr$ and high $^{207}Pb/^{206}Pb$ and $^{208}Pb/^{204}Pb$ at a given value of $^{206}Pb/^{204}Pb$). An EMI source can be explained by a degree of contamination by fluids derived from delaminated subcontinental lithosphere, ancient pelagic sediment or lower continental crust (Hofmann, 2004). To see whether the isotopic data can be explained by mixing with EMI type mantle a mixing model was calculated between HIMU and EMI and the results are plotted in Fig. 15. Harzburgite sample OU78 479, several of the Northern Victoria Land samples and one Southern Victoria Land sample can be explained by between 1 and <20% mixing between an EMI-type source and HIMU (Fig. 15b). A single Northern Victoria Land sample requires between 20 and 30% mixing (Fig. 15b). The available pyroxenite data do not plot on the HIMU–EMI mixing line.

There is evidence for Zr/Sm depletion in the peridotite xenoliths (Fig. 16b) and this type of behaviour, along with strong U/Th fractionation in the whole-rock geochemistry and the presence of rare carbonate neoblasts, has been explained by some workers as an indication of carbonatite metasomatism (e.g. Yaxley *et al.*, 1991; Pfänder *et al.*, 2012; Ackerman *et al.*, 2013). Carbonatite metasomatism has also been invoked to explain some aspects of the geochemical variation in Mount Morning volcanic rocks (Paulsen, 2008; Martin *et al.*, 2013). The effect of carbonatite metasomatism by average calcio-carbonatite on the Ti/Eu ratio of a depleted mantle source (harzburgite) has been calculated by Rudnick *et al.* (1993) and this model is shown in Fig. 16c. Comparisons of this model with the Mount Morning peridotite data indicates that the latter may have been metasomatized by the addition of ≤0·1 wt % carbonatite.

Formation of Mount Morning peridotite xenoliths

The mantle lithosphere beneath Mount Morning has probably undergone multiple depletion and melt–rock reaction events. The harzburgite xenoliths record degrees of melt depletion equal to or higher than those that have affected the lherzolite xenoliths, with mantle-normalized trace element patterns comparable with typical SCLM. The re-enrichment of major elements in some peridotite samples (Fig. 8) suggests they have been refertilized and there is evidence for refertilization by (1) N-MORB melts, (2) alkalic melts (Fig. 16a), and (3) a HIMU-like component. There is further evidence for peridotite metasomatism by (4) a sediment-like component, which could resemble EMI (Fig. 15b), and (5) a carbonatitic component (Fig. 16c). The timing of these various refertilization events will be discussed below. Many ophiolites contain dunite channels through which melt could have been transported (Kelemen *et al.*, 1995; Kohlstedt & Holtzman, 2009; Piccardo *et al.*, 2014). Dunite formation has been attributed to dissolution channelling whereby pyroxene is dissolved by olivine-saturated melt during porous flow (e.g. Daines & Kohlstedt, 1994; Kelemen *et al.*, 1995; Morgan & Liang, 2005). Two Mount Morning specimens (OU78 443 and 448) record evidence of melt depletion >20% (e.g. Fig. 14a) prior to formation of olivine-dominated dunite by dissolution channelling.

Origin of pyroxenite xenoliths

Pyroxenite xenoliths are samples of a relatively rare, yet important, part of the lithospheric mantle, making up ≤5% of peridotite massifs. It has been proposed that they play an important role during the genesis of intraplate basalts (e.g. Downes, 2007; Lambart *et al.*, 2013). There is a continuing discussion about the petrogenesis of pyroxenites (e.g. Downes, 2007; van Acken *et al.*, 2010, and references therein) and possible processes leading to their formation can include the following: (1) accumulation from asthenosphere-derived magmas passing through the lithosphere (Irving, 1980; Obata, 1980; Bodinier *et al.*, 1987; Takahashi, 1992; Perinelli *et al.*, 2011), which may be derived from subducted crust partial melting (Davies *et al.*, 1993; Pearson *et al.*, 1993); (2) some relation to eclogite, either as tectonically emplaced slices of subducted eclogite crust or as residues of *in situ* partial melting of such eclogites (Loubet & Allègre, 1982; Blichert-Toft *et al.*, 1999; Obata *et al.*, 2006); (3) a melt–rock reaction process, either between asthenospheric peridotite and subducted eclogitic oceanic crust (Yaxley & Green, 1998) or between peridotite wall-rock, existing peridotite and percolating melt (Garrido & Bodinier, 1999); (4) *in situ* processes, including crystallization of partial melts from the host peridotite (Dick & Sinton, 1979) or segregation of pyroxene from the peridotite wall-rock (Sinigoi *et al.*, 1983; Voshage *et al.*, 1988).

The role of upper continental crust in pyroxenite formation

On whole-rock mantle-normalized multi-element plots some of the websterite and clinopyroxenite patterns show Nb and Ti depletion and weak Pb enrichment (Fig. 11c and d) that could be indications of the involvement of a sediment-like component, as also seen in the peridotite data (Fig. 10). The Ti/Zr ratios in several of the Mount Morning pyroxenite xenoliths are comparable with those reported for Koettlitz Group metasediments in the adjacent Transantarctic Mountains (Allibone, 1988); on a Ti (ppm) vs Ti/Zr plot several of the samples lie along a trend between values for Koettlitz metasediment, average subducting sediment (Plank & Langmuir, 1998) and the eclogite field (Fig. 17). Several pyroxenite xenoliths from Mount Morning and Foster Crater have $^{87}Sr/^{86}Sr_i > 0{\cdot}7086$ and $^{143}Nd/^{144}Nd < 0{\cdot}51225$ plotting towards upper continental crust (UCC) and EMII (Enriched mantle II = low $^{143}Nd/^{144}Nd$, high $^{87}Sr/^{86}Sr$ and high $^{207}Pb/^{206}Pb$ and $^{208}Pb/^{204}Pb$ at a given value of $^{206}Pb/^{204}Pb$; Fig. 15a); these have been explained by a degree of mixing with an upper continental crust-like component introduced into the mantle via subduction

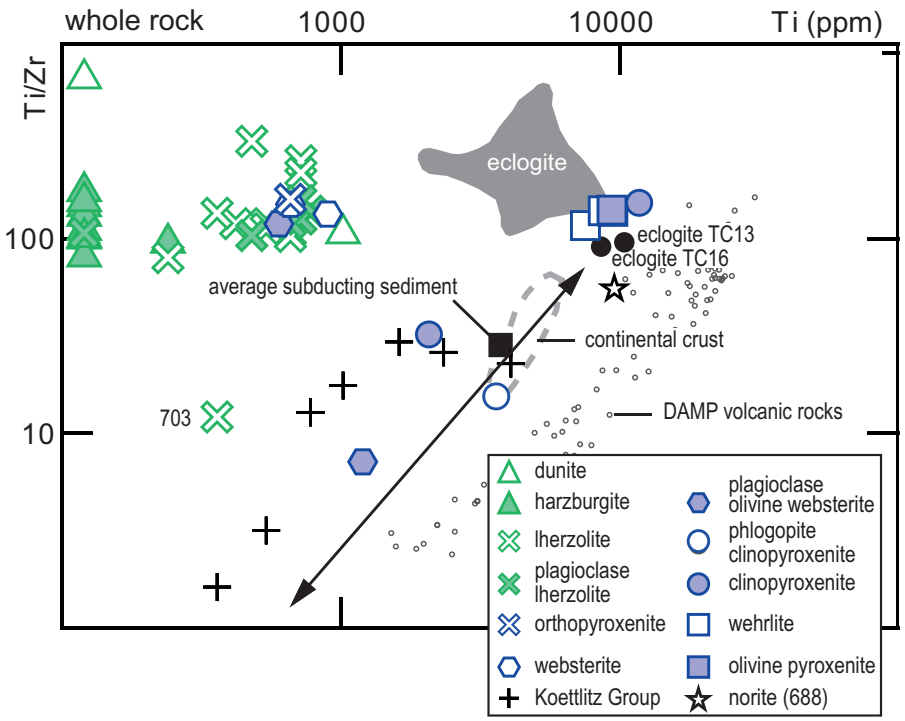

Fig. 17. Whole-rock Ti (ppm) vs Ti/Zr for Mount Morning peridotite and pyroxenite xenoliths and comparison with fields for various mantle, crustal and Antarctic basement compositions. Xenolithic eclogite field is from Rudnick *et al.* (2000). Average subducting sediment is from Plank & Langmuir (1998) and Koettlitz Group metasediment (black crosses) values are from Allibone (1988). Norite specimen OU78 688 is from Mount Morning (Martin *et al.*, 2013). The sources for DAMP are as in Fig. 15. The two eclogite samples (TC13, TC16) are 'well-preserved' eclogites from Northern Victoria Land, reported by Di Vincenzo *et al.* (1997). A general trend can be observed (arrowed black line) between the eclogite field, average subducting sediment and Koettlitz Group metasediments along which many of the Mount Morning pyroxenite xenoliths plot, as does norite specimen OU78 688 and eclogite specimens TC13 and TC16.

processes (Martin *et al.*, 2013). To further test the case for involvement of a sediment-like component in the pyroxenite xenoliths, mixing between a typical SCLM xenolith composition ($^{87}Sr/^{86}Sr = 0{\cdot}7043$, 50 ppm Sr; $^{143}Nd/^{144}Nd = 0{\cdot}51244$, 2 ppm Nd; after Erlank *et al.*, 1987) and upper continental crust ($^{87}Sr/^{86}Sr = 0{\cdot}73847$, 159 ppm Sr; $^{143}Nd/^{144}Nd = 0{\cdot}511800$, 26 ppm Nd; after Jourdan *et al.*, 2007) has been modelled following calculations given by Jourdan *et al.* (2007) and the results are shown graphically in Fig. 15a. The Mount Morning and Foster Crater pyroxenite data are consistent with between 10% and *c.* 20% mixing between SCLM and an upper crustal component (Fig. 15a). At Mount Morning a sediment-like component has played a significant role in the formation of the pyroxenite xenoliths.

The role of eclogite

Superficially, some aspects of the whole-rock major element compositions and REE patterns indicate similarities between the pyroxenites and the Mount Morning volcanic rocks. Closer inspection, however, reveals that relative to the Mount Morning volcanic rocks, the pyroxenites have relatively high wt % CaO and comparatively low TiO_2, FeO and Al_2O_3 abundances that do not fit with a simple mixing trend between the peridotite and primitive volcanic rocks (Fig. 9). The whole-rock chemistry of norite xenoliths collected from alkaline lava flows from Mount Morning, which are similar to lithologies from the nearby Transantarctic Mountain basement (Martin, 2009), do, however, form a continuum with some Mount Morning pyroxenite xenoliths. They have a similar range of major element oxide contents (at a given value of wt % MgO), and Mg# and REE patterns are comparable (Fig. 9 and Supplementary Data Fig. A6). This observation is in keeping with a small number of spinel mineral analyses on norite xenolith OU78 690 that are similar to some pyroxenite xenolith spinels (Fig. 5b; Supplementary Data Appendix 1). An interesting petrographic feature of the norite xenoliths collected from Mount Morning is the presence of spinel + orthopyroxene symplectites (Supplementary Data Fig. A9), which Shimizu *et al.* (2008) have eloquently argued form in lherzolite xenoliths from the breakdown of garnet. No garnet has been observed in any Mount Morning specimen or from the Erebus volcanic province, although it appears that the high-sodium group of clinopyroxenes record melting in the garnet peridotite stability field (Fig. 14b). A chemical fingerprint of the garnet stability field has been inferred for some Northern Victoria Land spinel peridotite xenoliths (e.g. Perinelli *et al.*, 2006).

The presence of symplectites possibly formed from the breakdown of garnet led to an investigation of whether eclogite might form part of the source of the

pyroxenite xenoliths. In Fig. 17, Mount Morning pyroxenite data are shown on a Ti (ppm) vs Ti/Zr plot with various fields shown for comparison. In general, the pyroxenites have higher Ti (ppm) and more variable Ti/Zr ratios than the peridotite xenoliths. Some pyroxenite data approach values associated with the refractory eclogite field (Rudnick *et al.*, 2000), some have compositions that plot close to that of average subducting sediment and, with the exception of the one orthopyroxenite (OU78 474) and some of the websterite data, the remaining data plot along a trend defined by the eclogite field and average subducting sediment. Highly radiogenic Os in mantle xenolith sulphides from Northern Victoria Land have been explained by mixing between eclogite and unradiogenic mantle, either during subduction associated with the Ross Orogen or during an older event (Melchiorre *et al.*, 2011). Eclogites have also been reported from the Lanterman Range in Northern Victoria Land (Fig. 1b; Di Vincenzo *et al.*, 1997) and their compositions (TC13, TC16) are plotted in Fig. 17 for comparison. The eclogite data overlap compositionally with the field of pyroxenite data from Mount Morning. The pyroxenite xenoliths at Mount Morning may be attributed to an eclogitic source mixed with a fluid whose composition is comparable with average upper continental crust; this may occur through melting of subducted, eclogitic crust and is discussed below.

Formation of Mount Morning pyroxenite xenoliths

Differences in clinopyroxene mineral chemistry between peridotite and pyroxenite xenoliths, for example on a wt % Na_2O_3 vs Cr_2O_3 plot (Fig. 4c), and between clinopyroxene chemistry in composite xenolith OU78 711 in the vein pyroxenite and host peridotite (Fig. 4), highlight that wall-rock segregation or simple host peridotite partial melt is an unlikely origin for pyroxenite. Some key observations about the Mount Morning pyroxenites are as follows. The pyroxenite xenoliths show some similarities to peridotite xenoliths on major element plots (Fig. 9) and mantle-normalized multi-element plots (Figs 10 and 11), but for the most part they plot discretely on trace element discrimination plots (e.g. Fig. 17). Eclogite is likely to have played a significant role in pyroxenite formation that is not significant in the formation of peridotite. With few exceptions there seems to be a different sediment-like component affecting pyroxenite formation at Mount Morning relative to peridotite xenoliths. Pyroxenites, in general, may be affected by a component similar to upper continental crust (resulting in EMII type signatures), with peridotite sample OU78 703 perhaps also affected by a similar component (Fig. 17). Peridotite, in general, might have been modified by a different sedimentary component from that involved in the petrogenesis of pyroxenite, resulting in mantle similar to EMI as modelled in Fig. 15b. The pyroxenites appear to have crystallized at pressures, temperatures and oxygen fugacities consistent with lithospheric mantle conditions. These observations are most consistent with pyroxenite forming from crystallization of percolating melts derived from, or modified by, fluids derived from subducted, eclogitic oceanic crust. The simplest, and our preferred, explanation for the sediment-like component modelled for the pyroxenite compositions is that it was also derived from this subducted crust.

Comparison with Northern Victoria Land and implications for DAMP volcanism

In general, Southern and Northern Victoria Land mantle xenoliths have common characteristics including modal mineralogy, the presence of rare yet distinct plagioclase lherzolite xenoliths, whole-rock and mineral chemistry and isotope compositions and possible eclogitic components, all of which suggest a similar petrogenesis. The range of $\Delta\log fO_2$ values of the spinel lherzolite lithospheric mantle overlaps between Northern and Southern Victoria Land and a median −1·0 value can be calculated for all of Victoria Land, suggesting comparable oxygen fugacity histories. There is debate as to whether chemical and isotopic source characteristics identified in DAMP Cenozoic volcanic rocks come exclusively from the asthenosphere or reflect some contribution from the lithosphere (e.g. Lanyon *et al.*, 1993; Baker *et al.*, 1994; Price *et al.*, 2003; Hoernle *et al.*, 2006; Panter *et al.*, 2006; Timm *et al.*, 2009, 2010; Scott *et al.*, 2014). In Fig. 17 the Mount Morning and DAMP volcanic rock data overlap with several of the pyroxenite samples, whose origin involves components of eclogite and upper continental crust-like fluids. One way to explain the Ti (ppm) vs Ti/Zr ratios in the DAMP volcanic rocks would be to derive them by preferential melting of pyroxenite domains with compositions similar to those of pyroxenite xenoliths from Mount Morning.

Petrogenesis of the lithospheric mantle beneath Mount Morning and timing of events

The lithospheric mantle beneath Mount Morning has undergone a complex history. Harzburgite and dunite xenolith whole-rock compositions overlap with the Archaean depleted mantle field and lherzolite compositions with Proterozoic and Phanerozoic depleted mantle fields defined by O'Reilly *et al.* (2001; Fig. 8b). These ages are in agreement with preliminary Palaeoproterozoic aluminachron stabilization ages for Mount Morning mantle lithosphere (Doherty *et al.*, 2012, 2013) and comparable with Proterozoic mantle stabilization ages determined for Marie Byrd Land SCLM (Handler *et al.*, 2003). The Mount Morning peridotite xenoliths record (probably multiple) depletion events in their whole-rock major and trace element and REE abundances. To the depleted mantle, various components have been added at various times including a HIMU-like component, a possible carbonatite component and a (possibly lower) continental crust-like component (resulting in an EMI type mantle signature). The lherzolite xenoliths have had an N-MORB component added and some xenoliths have been refertilized by an

alkalic melt component. Despite this complex history the $\Delta\log fO_2$ values of the spinel lherzolite lithospheric mantle at Mount Morning (–1 to FMQ) overlap with the global median in rifted settings (–0·9), suggesting both that oxygen fugacity measurements by Mössbauer spectroscopy are robust and that the mantle beneath continental rifts generally records complex histories of melting, metasomatism and refertilization.

Cross-cutting the peridotite host-rocks are veins of pyroxenite that share trace element and isotopic characteristics with eclogite and upper continental crust-like components, with the latter resulting in an EMII type mantle signature. Existing whole-rock isochron dates on a clinopyroxenite xenolith from Foster Crater (and the micas within it) give an age of $439{\cdot}2 \pm 14{\cdot}5$ Ma (McGibbon, 1991), which gives an indication of when the pyroxenite veins at Mount Morning may have crystallized. This age is comparable with a *c.* 500 Ma age determined on eclogite from the Lanterman Range in Northern Victoria Land (Di Vincenzo *et al.*, 1997). Di Vincenzo *et al.* (1997) determined this age from internal Sm–Nd isochrons, combining whole-rock and mineral (rutile, clinopyroxene, amphibole and garnet) data (500 ± 5 Ma) and further supported it by determining rutile–whole-rock ^{238}U–^{206}Pb ages (*c.* 500 Ma) on the same samples. It is not certain whether the peridotites were metasomatized at the same time as the pyroxenite veins were emplaced, but zircon extracted from a carbonatite only ~100 km from Mount Morning yielded an age of $531 \pm 5{\cdot}5$ Ma (Hall *et al.*, 1995) and may indicate that this was a time of general (carbonatite) metasomatism of the lithospheric mantle.

In the region where Southern Victoria Land now sits, during the Ediacaran–early Paleozoic time period covered by the above dates, the Palaeo-Pacific plate was subducting beneath the Gondwana margin (Stump, 1995; Rocchi *et al.*, 2011). Evidence that fluids derived from the subducting plate passed through the lithosphere is recorded in the chemistry and chronology of the Dry Valley suite of arc-related, early Precambrian to early Paleozoic plutons in the adjacent Transantarctic Mountains (Allibone *et al.*, 1993; Cox *et al.*, 2000, 2012) and in crustal xenoliths of similar age and composition entrained within alkalic lava flows at Mount Morning (Martin, 2009; Martin *et al.*, 2015). The simplest explanation for the timing of the formation of pyroxenite xenoliths at Mount Morning is that they originated as fluids derived from, or modified by, this subducting plate. Some of the metasomatizing components may also have affected the peridotite wall-rocks at this time; for example, sample OU78 703 with a depleted Ti/Zr composition in Fig. 17 could represent a metasomatized peridotitic wall-rock. Other peridotite samples may have been affected by more ancient events.

ACKNOWLEDGEMENTS

We thank Damian Walls, Brent Pooley, Andreas Audétat and Detlef Krauße for analytical support and useful discussion. Kurt Panter, Massimo Coltorti and an anonymous reviewer are thanked for constructive reviews, and John Gamble for editorial handling.

FUNDING

A.P.M. was supported by an Antarctica New Zealand (NZ Post) Antarctic scholarship, a University of Otago award from the Department of Geology and a Marie Curie Fellowship supported by the European Commission under the Marie Curie Action for Early Stage Training of Researchers within the 6th Framework Program (contract number MEST-CT-2005–019700). Antarctica New Zealand provided fieldwork logistical support.

SUPPLEMENTARY DATA

Supplementary data for this paper are available at *Journal of Petrology* online.

REFERENCES

Ackerman, L., Špaček, P., Magna, T., Ulrych, J., Svojtka, M., Hegner, E. & Balogh, K. (2013). Alkaline and carbonate-rich melt metasomatism and melting of subcontinental lithospheric mantle: evidence from mantle xenoliths, NE Bavaria, Bohemian Massif. *Journal of Petrology* **54**, 2597–2633.

Allibone, A. H. (1988). Koettlitz Group, Antarctica. MSc thesis, University of Otago, Dunedin.

Allibone, A. & Wysoczanski, R. (2002). Initiation of magmatism during the Cambrian–Ordovician Ross Orogeny in southern Victoria Land, Antarctica. *Geological Society of America Bulletin* **114**, 1007–1018.

Allibone, A. H., Cox, S. C., Graham, I. J., Smillie, R. W., Johnstone, R. D., Ellery, S. G. & Palmer, K. (1993). Granitoids of the Dry Valleys area, southern Victoria Land, Antarctica: plutons, field relationships, and isotopic dating. *New Zealand Journal of Geology and Geophysics* **36**, 281–297.

Arai, S. (1994). Characterization of spinel peridotites by olivine–spinel compositional relationships: Review and interpretation. *Chemical Geology* **113**, 191–204.

Armienti, P. & Perinelli, C. (2010). Cenozoic thermal evolution of lithospheric mantle in northern Victoria Land (Antarctica): Evidences from mantle xenoliths. *Tectonophysics* **486**, 28–35.

Babechuk, M. G., Kamber, B. S., Greig, A., Canil, D. & Kodolányi, J. (2010). The behaviour of tungsten during mantle melting revisited with implications for planetary differentiation time scales. *Geochimica et Cosmochimica Acta* **74**, 1448–1470.

Baker, I. A., Gamble, J. A. & Graham, I. J. (1994). The age, geology, and geochemistry of the Tapuaenuku Igneous Complex, Marlborough, New Zealand. *New Zealand Journal of Geology and Geophysics* **37**, 249–268.

Ballhaus, C., Berry, R. F. & Green, D. H. (1991). High pressure experimental calibration of the olivine–orthopyroxene–spinel oxygen geobarometer: Implications for the oxidation state of the upper mantle. *Contributions to Mineralogy and Petrology* **107**, 27–40.

Bannister, S., Yu, J., Leitner, B. & Kennett, B. L. N. (2003). Variations in crustal structure across the transition from

West to East Antarctica, Southern Victoria Land. *Geophysical Journal International* **155**, 870–884.

Berg, J. H., Moscati, R. J. & Herz, D. L. (1989). A petrologic geotherm from a continental rift in Antarctica. *Earth and Planetary Science Letters* **93**, 98–108.

Blichert-Toft, J., Albarède, F. & Kornprobst, J. (1999). Lu–Hf isotope systematics of garnet pyroxenites from Beni Bousera, Morocco: implications for basalt origin. *Science* **283**, 1303–1306.

Blundy, J. D., Falloon, T. J., Wood, B. J. & Dalton, J. A. (1995). Sodium partitioning between clinopyroxene and silicate melts. *Journal of Geophysical Research: Solid Earth* **100**, 15501–15515.

Bodinier, J. L., Guiraud, M., Fabriès, J., Dostal, J. & Dupuy, C. (1987). Petrogenesis of layered pyroxenites from the Lherz, Freychinède and Prades ultramafic bodies (Ariège, French Pyrenees). *Geochimica et Cosmochimica Acta* **51**, 279–290.

Bonadiman, C., Nazzareni, S., Coltorti, M., Comodi, P., Giuli, G. & Faccini, B. (2014). Crystal chemistry of amphiboles: implications for oxygen fugacity and water activity in lithospheric mantle beneath Victoria Land, Antarctica. *Contributions to Mineralogy and Petrology* **167**, 1–17.

Borg, S. G. & DePaolo, D. J. (1991). A tectonic model of the Antarctic Gondwana margin with implications for southeastern Australia: Isotopic and geochemical evidence. *Tectonophysics* **196**, 339–358.

Borghini, G., Fumagalli, P. & Rampone, E. (2011). The geobarometric significance of plagioclase in mantle peridotites: A link between nature and experiments. *Lithos* **126**, 42–53.

Boyd, F. R. (1989). Compositional distinction between oceanic and cratonic lithosphere. *Earth and Planetary Science Letters* **96**, 15–26.

Braun, M. G. & Kelemen, P. B. (2002). Dunite distribution in the Oman Ophiolite: Implications for melt flux through porous dunite conduits. *Geochemistry, Geophysics, Geosystems* **3**, 8603.

Brey, G. P. & Kohler, T. (1990). Geothermobarometry in four-phase lherzolites II. New thermobarometers, and practical assessment of existing thermobarometers. *Journal of Petrology* **31**, 1353–1378.

Canil, D. & O'Neill, H. S. C. (1996). Distribution of ferric iron in some upper-mantle assemblages. *Journal of Petrology* **37**, 609–635.

Canil, D., O'Neill, H. S. C., Pearson, D. G., Rudnick, R. L., McDonough, W. F. & Carswell, D. A. (1994). Ferric iron in peridotites and mantle oxidation states. *Earth and Planetary Science Letters* **123**, 205–220.

Chapman, D. S. (1986). Thermal gradients in the continental crust. In: Dawson, J. B., Carswell, D. A., Hall, J. & Wedepohl, K. H. (eds) *The Nature of the Lower Continental Crust. Geological Society, London, Special Publications* **24**, 63–70.

Coltorti, M., Beccaluva, L., Bonadiman, C., Faccini, B., Ntaflos, T. & Siena, F. (2004). Amphibole genesis via metasomatic reaction with clinopyroxene in mantle xenoliths from Victoria Land, Antarctica. *Lithos* **75**, 115–139.

Cooper, A. F., Adam, L. J., Coulter, R. F., Eby, G. N. & McIntosh, W. C. (2007). Geology, geochronology and geochemistry of a basanitic volcano, White Island, Ross Sea, Antarctica. *Journal of Volcanology and Geothermal Research* **165**, 189–216.

Cox, S. C., Parkinson, D. L., Allibone, A. H. & Cooper, A. F. (2000). Isotopic character of Cambro-Ordovician plutonism, Southern Victoria Land, Antarctica. *New Zealand Journal of Geology and Geophysics* **43**, 501–520.

Cox, S. C., Turnbull, I. M., Isaac, M. J., Townsend, D. B. & Smith Lyttle, B. (2012). *Geology of southern Victoria Land Antarctica. Institute of Geological and Nuclear Sciences 1:250 000 Geological Map 22*. GNS Science, 1 sheet + 135 pp.

Daines, M. J. & Kohlstedt, D. L. (1994). The transition from porous to channelized flow due to melt/rock reaction during melt migration. *Geophysical Research Letters* **21**, 145–148.

Davies, G. R., Nixon, P. H., Pearson, D. G. & Obata, M. (1993). Tectonic implications of graphitized diamonds from the Ronda, peridotite massif, southern Spain. *Geology* **21**, 471–474.

Dick, H. J. B. & Sinton, J. M. (1979). Compositional layering in Alpine peridotites: evidence for pressure solution creep in the mantle. *Journal of Geology* **87**, 403–416.

Di Roberto, A., Del Carlo, P., Rocchi, S. & Panter, K. S. (2012). Early Miocene volcanic activity and paleoenvironment conditions recorded in tephra layers of the AND-2A core (southern McMurdo Sound, Antarctica). *Geosphere* **8**, 1342–1355.

Di Vincenzo, G., Palmeri, R., Talarico, F., Andriessen, P. A. M. & Ricci, G. A. (1997). Petrology and Geochronology of Eclogites from the Lanterman Range, Antarctica. *Journal of Petrology* **38**, 1391–1417.

Doherty, C., Class, C., Goldstein, S. L., Shirey, S. B., Martin, A. P., Cooper, A. F., Berg, J. H. & Gamble, J. A. (2012). Constraining the dynamic response of subcontinental lithospheric mantle to rifting using Re–Os model ages in the Western Ross Sea, Antarctica. Abstract presented at 2012 Fall Meeting, AGU, San Francisco, CA.

Doherty, C., Class, C., Goldstein, S. L., Shirey, S. B., Martin, A. P., Cooper, A. F., Berg, J. H. & Gamble, J. A. (2013). Re–Os systematics of the lithospheric mantle beneath the Western Ross Sea area, Antarctica: depletion ages and dynamic response during rifting. AGU, San Francisco, CA, 9–13 December, T13A-2516.

Downes, H. (2007). Origin and significance of spinel and garnet pyroxenites in the shallow lithospheric mantle: Ultramafic massifs in orogenic belts in Western Europe and NW Africa. *Lithos* **99**, 1–24.

Eggins, S. M., Woodhead, J. D., Kinsley, L. P. J., Mortimer, G. E., Sylvester, P., McCulloch, M. T., Hergt, J. M. & Handler, M. R. (1997). A simple method for the precise determination of $\geq$40 trace elements in geological samples by ICPMS using enriched isotope internal standardisation. *Chemical Geology* **134**, 311–326.

Erlank, A. J., Hawkesworth, C. J., Haggerty, S. E., Allsopp, H. L., Rickard, R. S. & Menzies, M. A. (1987). Evidence for mantle metasomatism in peridotite nodules of the Kimberley pipes, South Africa. In: Hawkesworth, C. J. & Menzies, M. (eds) *Mantle Metasomatism*. Academic Press, pp. 221–311.

Faure, G. (1986). *Principles of Isotope Geology*, 2nd edn. New York: John Wiley.

Finger, L. W. (1972). The uncertainty in the calculated ferric iron content of a microprobe analysis. *Carnegie Institute of Washington Yearbook* **71**, 600–603.

Finn, C. A., Müller, R. D. & Panter, K. S. (2005). A Cenozoic diffuse alkaline magmatic province (DAMP) in the southwest Pacific without rift or plume origin. *Geochemistry, Geophysics, Geosystems* **6**, Q02005.

Foley, S. F., Andronikov, A. V., Jacob, D. E. & Melzer, S. (2006). Evidence from Antarctic mantle peridotite xenoliths for changes in mineralogy, geochemistry and geothermal gradients beneath a developing rift. *Geochimica et Cosmochimica Acta* **70**, 3096–3120.

Frey, F. A. & Prinz, M. (1978). Ultramafic inclusions from San Carlos, Arizona: Petrologic and geochemical data bearing on their petrogenesis. *Earth and Planetary Science Letters* **38**, 129–176.

Frost, D. J. & McCammon, C. A. (2008). The redox state of the Earth's mantle. *Annual Review of Earth and Planetary Sciences* **36**, 389–420.

Gale, A., Dalton, C. A., Langmuir, C. H., Su, Y. & Schilling, J.-G. (2013). The mean composition of ocean ridge basalts. *Geochemistry, Geophysics, Geosystems* **14**, 489–518.

Gamble, J. A. & Kyle, P. R. (1987). The origins of glass and amphibole in spinel-wehrlite xenoliths from Foster Crater, McMurdo Volcanic Group, Antarctica. *Journal of Petrology* **28**, 755–779.

Gamble, J. A., McGibbon, F., Kyle, P. R., Menzies, M. & Kirsch, I. (1988). Metasomatised xenoliths from Foster Crater, Antarctica: Implications for lithospheric structure and process beneath the Transantarctic Mountain front. *Journal of Petrology*, **Special Volume 1**, 109–138.

Garrido, C. J. & Bodinier, J. L. (1999). Diversity of mafic rocks in the Ronda peridotite: Evidence for pervasive melt–rock reaction during heating of subcontinental lithosphere by upwelling asthenosphere. *Journal of Petrology* **40**, 729–754.

Griffin, W. L., O'Reilly, S. Y., Afonso, J. C. & Begg, G. C. (2009). The composition and evolution of lithospheric mantle: a re-evaluation and its tectonic implications. *Journal of Petrology* **50**, 1185–1204.

Grindley, G. W., Oliver, P. J. & Sukroo, J. C. (1981). Lower Mesozoic position of southern New Zealand determined from paleomagnetism of the Glenham Porphyry, Murihiku Terrane, Eastern Southland. In: Cresswell, M. M. & Vella, P. (eds.) *Gondwana Five*. Rotterdam: Balkema, pp. 319–326.

Hall, C. E., Cooper, A. F. & Parkinson, D. L. (1995). Early Cambrian carbonatite in Antarctica. *Journal of the Geological Society, London* **152**, 721–728.

Handler, M. R., Wysoczanski, R. J. & Gamble, J. A. (2003). Proterozoic lithosphere in Marie Byrd Land, West Antarctica: Re–Os systematics of spinel peridotite xenoliths. *Chemical Geology* **196**, 131–145.

Harte, B. (1977). Rock nomenclature with particular relation to deformation and recrystallization textures in olivine-bearing xenoliths. *Journal of Geology* **85**, 279–288.

Herd, C. D. K. (2008). Basalts as probes of planetary interior redox state. In: MacPherson, G. J. (ed.) *Oxygen in the Solar System. Mineralogical Society of America and Geochemical Society, Reviews in Mineralogy and Geochemistry* **68**, 527–553.

Herzberg, C. (2004). Geodynamic information in peridotite petrology. *Journal of Petrology* **45**, 2507–2530.

Hoernle, K., White, J. D. L., van den Bogaard, P., Hauff, F., Coombs, D. S., Werner, R., Timm, C., Garbe-Schönberg, D., Reay, A. & Cooper, A. F. (2006). Cenozoic intraplate volcanism on New Zealand: Upwelling induced by lithospheric removal. *Earth and Planetary Science Letters* **248**, 350–367.

Hofmann, A. W. (2004). Sampling mantle heterogeneity through oceanic basalts; isotopes and trace elements. In: Carlson, R. W., Holland, H. D. & Turekian, K. K. (eds) *The Mantle and Core. Treatise on Geochemistry, Volume 2*. Oxford: Elsevier, pp. 61–102.

Holland, T. J. B. & Powell, R. (1998). An internally consistent thermodynamic data set for phases of petrological interest. *Journal of Metamorphic Geology* **16**, 309–343.

Ionov, D. A. & Wood, B. J. (1992). The oxidation state of subcontinental mantle: Oxygen thermobarometry of mantle xenoliths from central Asia. *Contributions to Mineralogy and Petrology* **111**, 179–193.

Ionov, D. A., Bodinier, J.-L., Mukasa, S. B. & Zanetti, A. (2002). Mechanisms and sources of mantle metasomatism: major and trace element compositions of peridotite xenoliths from Spitsbergen in the context of numerical modelling. *Journal of Petrology* **43**, 2219–2259.

Irving, A. J. (1980). Petrology and geochemistry of composite ultramafic xenoliths in alkalic basalts and implications for magmatic processes within the mantle. *American Journal of Science* **280**, 389–426.

Jackson, M. G., Hart, S. R., Koppers, A. A. P., Staudigel, H., Konter, J., Blusztajn, J., Kurz, M. D. & Russell, J. A. (2007). The return of subducted continental crust in Samoan lavas. *Nature* **448**, 684–697.

Johnson, K. T. M. (1998). Experimental determination of partition coefficients for rare earth and high-field-strength elements between clinopyroxene, garnet, and basaltic melt at high pressures. *Contributions to Mineralogy and Petrology* **133**, 60–68.

Johnson, K. T. M., Dick, H. J. B. & Shimizu, N. (1990). Melting in the oceanic upper mantle: An ion microprobe study of diopsides in abyssal peridotites. *Journal of Geophysical Research: Solid Earth* **95**, 2661–2678.

Jourdan, F., Bertrand, H., Schärer, U., Blichert-Toft, J., Féraud, G. & Kampunzu, A. B. (2007). Major and trace element and Sr, Nd, Hf, and Pb isotope compositions of the Karoo Large Igneous Province, Botswana–Zimbabwe: lithosphere vs mantle plume contribution. *Journal of Petrology* **48**, 1043–1077.

Kamber, B. S., Greig, A., Schoenberg, R. & Collerson, K. D. (2003). A refined solution to Earth's hidden niobium: implications for evolution of continental crust and mode of core formation. *Precambrian Research* **126**, 289–308.

Kamber, B. S., Greig, A. & Collerson, K. D. (2005). A new estimate for the composition of weathered young upper continental crust from alluvial sediments, Queensland, Australia. *Geochimica et Cosmochimica Acta* **69**, 1041–1058.

Kelemen, P. B., Shimizu, N. & Dunn, T. (1993). Relative depletion of niobium in some arc magmas and the continental crust: partitioning of K, Nb, La and Ce during melt/rock reaction in the upper mantle. *Earth and Planetary Science Letters* **120**, 111–134.

Kelemen, P. B., Shimizu, N. & Salters, V. J. M. (1995). Extraction of mid-ocean-ridge basalt from the upwelling mantle by focused flow of melt in dunite channels. *Nature* **375**, 747–753.

Kelemen, P. B., Hart, S. R. & Bernstein, S. (1998). Silica enrichment in the continental upper mantle via melt/rock reaction. *Earth and Planetary Science Letters* **164**, 387–406.

Kinzler, R. J. (1997). Melting of mantle peridotite at pressures approaching the spinel to garnet transition: Application to mid-ocean ridge basalt petrogenesis. *Journal of Geophysical Research: Solid Earth* **102**, 853–874.

Kohlstedt, D. L. & Holtzman, B. K. (2009). Shearing melt out of the Earth: An experimentalist's perspective on the influence of deformation on melt extraction. *Annual Review of Earth and Planetary Sciences* **37**, 561–593.

Kyle, P. R. (1990a). Erebus Volcanic Province summary. In: LeMasurier, W. E. & Thomson, J. W. (eds) *Volcanoes of the Antarctic Plate and Southern Oceans. American Geophysical Union, Antarctic Research Series* **48**, 81–88.

Kyle, P. R. (1990b). McMurdo Volcanic Group—western Ross Embayment: Introduction. In: LeMasurier, W. E. & Thompson, J. (eds) *Volcanoes of the Antarctic Plate and Southern Oceans. American Geophysical Union, Antarctic Research Series* **48**, 18–25.

Kyle, P. R., Wright, A. C. & Kirsch, I. (1987). Ultramafic xenoliths in the late Cenozoic McMurdo Volcanic Group, western Ross Sea embayment, Antarctica. In: Nixon, P. H. (ed.) *Mantle Xenoliths*. John Wiley, pp. 287–293.

Lambart, S., Laporte, D. & Schiano, P. (2009). An experimental study of pyroxenite partial melts at 1 and 1·5 GPa: Implications for the major-element composition of mid-ocean ridge basalts. *Earth and Planetary Science Letters* **288**, 335–347.

Lambart, S., Laporte, D. & Schiano, P. (2013). Markers of the pyroxenite contribution in the major-element compositions

of oceanic basalts: Review of the experimental constraints. *Lithos* **160–161**, 14–36.

Langmuir, C. H., Klein, E. M. & Plank, T. (1993). Petrological systematics of mid-ocean ridge basalts: constraints on melt generation beneath ocean ridges. In: Phipps Morgan, J., Blackman, D. K. & Sinton, J. M. (eds) *Mantle Flow and Melt Generation at Mid-Ocean Ridges. Geophysical Monograph, American Geophysical Union* **71**, 183–280.

Lanyon, R., Varne, R. & Crawford, A. J. (1993). Tasmanian Tertiary basalts, the Balleny plume, and opening of the Tasman Sea (southwest Pacific Ocean). *Geology* **21**, 555–558.

Lazarov, M., Brey, G. P. & Weyer, S. (2012). Evolution of the South African mantle—a case study of garnet peridotites from the Finsch diamond mine (Kaapvaal craton); Part 2: Multiple depletion and re-enrichment processes. *Lithos* **154**, 210–223.

Le Roux, V., Bodinier, J. L., Tommasi, A., Alard, O., Dautria, J. M., Vauchez, A. & Riches, A. J. V. (2007). The Lherz spinel lherzolite: Refertilized rather than pristine mantle. *Earth and Planetary Science Letters* **259**, 599–612.

Lee, C.-T. A., Luffi, P. & Chin, E. J. (2011). Building and destroying continental mantle. *Annual Review of Earth and Planetary Sciences* **39**, 59–90.

Liu, J., Carlson, R. W., Rudnick, R. L., Walker, R. J., Gao, S. & Wu, F. (2012). Comparative Sr–Nd–Hf–Os–Pb isotope systematics of xenolithic peridotites from Yangyuan, North China Craton: Additional evidence for a Paleoproterozoic age. *Chemical Geology* **332**, 1–14.

Loubet, M. & Allègre, C. J. (1982). Trace elements in orogenic lherzolites reveal the complex history of the upper mantle. *Nature* **298**, 809–814.

Luth, R. W. & Canil, D. (1993). Ferric iron in mantle-derived pyroxenes and a new oxybarometer for the mantle. *Contributions to Mineralogy and Petrology* **113**, 236–248.

Martin, A. P. (2009). Mount Morning, Antarctica: Geochemistry, geochronology, petrology, volcanology, and oxygen fugacity of the rifted Antarctic lithosphere. PhD thesis, University of Otago, Dunedin, 264 pp.

Martin, A. P. & Cooper, A. F. (2010). Post 3·9 Ma fault activity within the West Antarctic rift system: onshore evidence from Gandalf Ridge, Mount Morning eruptive centre, southern Victoria Land, Antarctica. *Antarctic Science* **22**, 513–521.

Martin, A. P., Cooper, A. F. & Dunlap, W. J. (2010). Geochronology of Mount Morning, Antarctica: Two-phase evolution of a long-lived trachyte–basanite–phonolite eruptive center. *Bulletin of Volcanology* **72**, 357–371, doi:10.1007/s00445–009–0319–1.

Martin, A. P., Cooper, A. F. & Price, R. C. (2013). Petrogenesis of Cenozoic, alkalic volcanic lineages at Mount Morning, West Antarctica and their entrained lithospheric mantle xenoliths: Lithospheric versus asthenospheric mantle sources. *Geochimica et Cosmochimica Acta* **122**, 127–152.

Martin, A. P., Cooper, A. F. & Price, R. C. (2014). Increased mantle heat flow with on-going rifting of the West Antarctic rift system inferred from characterisation of plagioclase peridotite in the shallow Antarctic mantle. *Lithos* **190–191**, 173–190.

Martin, A. P., Cooper, A. F., Price, R. C., Turnbull, R.E. & Roberts, N. M. W. (2015). The petrology, geochronology and significance of Granite Harbour Intrusive Complex xenoliths and outcrop sampled in western McMurdo Sound, Southern Victoria Land, Antarctica. *New Zealand Journal of Geology and Geophysics* **58**, doi:10.1080/00288306.2014.982660.

McCammon, C. (1994). A Mössbauer milliprobe: Practical considerations. *Hyperfine Interactions* **92**, 1235–1239.

McCammon, C. A., Chaskar, V. & Richards, G. G. (1991). A technique for spatially resolved Mössbauer spectroscopy applied to quenched metallurgical slags. *Measurement Science Technology* **2**, 657–662.

McCulloch, M. T. & Gamble, J. A. (1991). Geochemical and geodynamical constraints on subduction zone magmatism. *Earth and Planetary Science Letters* **102**, 358–374.

McDonough, W. F. (1990). Constraints on the composition of the continental lithospheric mantle. *Earth and Planetary Science Letters* **101**, 1–18.

McDonough, W. F. & Sun, S.-S. (1995). The composition of the Earth. *Chemical Geology* **120**, 223–253.

McGibbon, F. M. (1991). Geochemistry and petrology of ultramafic xenoliths of the Erebus Volcanic Province. In: Thomson, M. R. A., Crame, J. A. & Thomson, J. W. (eds) *Geological Evolution of Antarctica—Proceedings of the 5th International Symposium on Antarctic Earth Sciences*. Cambridge University Press, pp. 317–321.

McGuiness, L. D., Bowen, R. H., Erickson, J. M., Alfred, B. J. & Kreamer, J. L. (1985). East–West Antarctic boundary in McMurdo Sound. *Tectonophysics* **114**, 341–356.

Melchiorre, M., Coltorti, M., Bonadiman, C., Faccini, B., O'Reilly, S. Y. & Pearson, N. J. (2011). The role of eclogite in the rift-related metasomatism and Cenozoic magmatism of Northern Victoria Land, Antarctica. *Lithos* **124**, 319–330.

Morgan, Z. & Liang, Y. (2005). An experimental study of the kinetics of lherzolite reactive dissolution with applications to melt channel formation. *Contributions to Mineralogy and Petrology* **150**, 369–385.

Morimoto, N. (1989). Nomenclature of pyroxenes. *Canadian Mineralogist* **27**, 143–156.

Müntener, O., Pettke, T., Desmurs, L., Meier, M. & Schaltegger, U. (2004). Refertilization of mantle peridotite in embryonic ocean basins: Trace element and Nd isotopic evidence and implications for crust–mantle relationships. *Earth and Planetary Science Letters* **221**, 293–308.

Müntener, O., Manatschal, G., Desmurs, L. & Pettke, T. (2010). Plagioclase peridotites in ocean–continent transitions: refertilized mantle domains generated by melt stagnation in the shallow mantle lithosphere. *Journal of Petrology* **51**, 255–294.

Nardini, I., Armienti, P., Rocchi, S., Dallai, L. & Harrison, D. (2009). Sr–Nd–Pb–He–O isotope and geochemical constraints on the genesis of Cenozoic magmas from the West Antarctic Rift. *Journal of Petrology* **50**, 1359–1375.

Nielson, J. E. & Wilshire, H. G. (1993). Magma transport and metasomatism in the mantle; a critical review of current geochemical models. *American Mineralogist* **78**, 1117–1134.

Niu, Y. (2004). Bulk-rock major and trace element compositions of abyssal peridotites: Implications for mantle melting, melt extraction and post-melting processes beneath mid-ocean ridges. *Journal of Petrology* **45**, 2423–2458.

Norrish, K. & Chappell, B. W. (1977). X-ray fluorescence spectrometry. In: Zussman, J. (ed.) *Physical Methods in Determinative Mineralogy*, 2nd edn. Academic Press, pp. 207–272.

Nyland, R. E., Panter, K. S., Rocchi, S., Di Vincenzo, G., Del Carlo, P., Tiepolo, M., Field, B. & Gorsevski, P. (2013). Volcanic activity and its link to glaciation cycles: Single-grain age and geochemistry of Early to Middle Miocene volcanic glass from ANDRILL AND-2A core, Antarctica. *Journal of Volcanology and Geothermal Research* **250**, 106–128.

Obata, M. (1980). The Ronda peridotite: garnet-, spinel-, and plagioclase-lherzolite facies and the *P–T* trajectories of a high-temprature mantle intrusion. *Journal of Petrology* **21**, 533–572.

Obata, M., Hirajima, T. & Svojtka, M. (2006). Origin of eclogite and garnet pyroxenite from the Moldanubian Zone of the

Bohemian Massif, Czech Republic and its implication to other mafic layers embedded in orogenic peridotites. *Mineralogy and Petrology* **88**, 321–340.

O'Neill, H. S. C., Rubie, D. C., Canil, D., Geiger, C. A., Ross, C. R., Seifert, F., & Woodland, A. B. (1993). Ferric iron in the upper mantle and in transition zone assemblages: Implications for relative oxygen fugacities in the mantle. In: Takahashi, E., Jeanloz, R. & Rubie, D. (eds.) *Evolution of the Earth and Planets*. American Geophysical Union, 73–88.

O'Neill, H. S. C. & Wall, V. J. (1987). The olivine–orthopyroxene–spinel oxygen geobarometer, the nickel precipitation curve, and the oxygen fugacity of the Earth's upper mantle. *Journal of Petrology* **28**, 1169–1191.

O'Reilly, S. Y., Griffin, W. L., Poudjom, Y. H. & Morgan, P. (2001). Are lithospheres forever? Tracking changes in subcontinental lithospheric mantle through time. *GSA Today* **11**, 4–10.

Panter, K. S., Blusztajn, J., Hart, S. R., Kyle, P. R., Esser, R. & McIntosh, W. C. (2006). The origin of HIMU in the SW Pacific: evidence from intraplate volcanism in southern New Zealand and subantarctic islands. *Journal of Petrology* **47**, 1673–1704.

Paulsen, H.-K. (2008). A lithological cross section through Mount Morning, Antarctica: A story told from xenolithic assemblages in a pyroclastic deposit. MSc thesis, University of Otago, Dunedin, p. 179.

Pearce, J. A. (1982). Trace element characteristics of lavas from destructive plate boundaries. In: Thorpe, R. S. (ed.) *Andesites: Orogenic Andesites and Related Rocks*. John Wiley, pp. 526–547.

Pearson, D. G., Davies, G. R. & Nixon, P. H. (1993). Geochemical constraints on the petrogenesis of diamond facies pyroxenites from the Beni Bousera Peridotite Massif, North Morocco. *Journal of Petrology* **34**, 125–172.

Perinelli, C., Armienti, P. & Dallai, L. (2006). Geochemical and O-isotope constraints on the evolution of lithospheric mantle in the Ross Sea rift area (Antarctica). *Contributions to Mineralogy and Petrology* **151**, 245–266.

Perinelli, C., Orlando, A., Conte, A. M., Armienti, P., Borrini, D., Faccini, B. & Misiti, V. (2008). Metasomatism induced by alkaline magma in the upper mantle of northern Victoria Land (Antarctica): an experimental approach. In: Coltorti, M. & Grégoire, M. (eds) *Metasomatism in Oceanic and Continental Lithospheric Mantle. Geological Society, London, Special Publications* **293**, 279–302.

Perinelli, C., Armienti, P. & Dallai, L. (2011). Thermal evolution of the lithosphere in a rift environment as inferred from the geochemistry of mantle cumulates, northern Victoria Land, Antarctica. *Journal of Petrology* **52**, 665–690.

Perinelli, C., Andreozzi, G., Conte, A., Oberti, R. & Armienti, P. (2012). Redox state of subcontinental lithospheric mantle and relationships with metasomatism: insights from spinel peridotites from northern Victoria Land (Antarctica). *Contributions to Mineralogy and Petrology* **164**, 1053–1067.

Pfänder, J. A., Jung, S., Münker, C., Stracke, A. & Mezger, K. (2012). A possible high Nb/Ta reservoir in the continental lithospheric mantle and consequences on the global Nb budget—Evidence from continental basalts from Central Germany. *Geochimica et Cosmochimica Acta* **77**, 232–251.

Piccardo, G. B., Padovano, M. & Guarnieri, L. (2014). The Ligurian Tethys: Mantle processes and geodynamics. *Earth-Science Reviews* **138**, 409–434.

Pike, J. E. N. & Schwarzman, E. C. (1977). Classification of textures in ultramafic xenoliths. *Journal of Geology* **85**, 49–61.

Plank, T. & Langmuir, C. H. (1998). The chemical composition of subducting sediment and its consequence for the crust and mantle. *Chemical Geology* **145**, 325–394.

Price, R. C., McCulloch, M. T., Smith, I. E. M. & Stewart, R. B. (1992). Pb–Nd–Sr isotopic compositions and trace element characteristics of young volcanic rocks from Egmont Volcano and comparisons with basalts and andesites from the Taupo Volcanic Zone, New Zealand. *Geochimica et Cosmochimica Acta* **56**, 941–953.

Price, R. C., Cooper, A. F., Woodhead, J. D. & Cartwright, I. A. N. (2003). Phonolitic diatremes within the Dunedin Volcano, South Island, New Zealand. *Journal of Petrology* **44**, 2053–2080.

Prior, G. T. (1902). *Report on the rock specimens collected by the Southern Cross Antarctic Expedition*. British Museum.

Prior, G. T. (1907). *Report on the rock specimens collected during the 'Discovery' Antarctic Expedition, 1901–1904. Natural History 1*. British Museum, pp. 101–160.

Putirka, K., Ryerson, F. J., Perfit, M. & Ridley, W. I. (2011). Mineralogy and composition of the oceanic mantle. *Journal of Petrology* **52**, 279–313.

Putirka, K. D. (2008). Thermometers and barometers for volcanic systems. In: Putirka, K. D. & Tepley, F. J., III (eds) *Minerals, Inclusions and Volcanic Processes. Mineralogical Society of America and Geochemical Society, Reviews in Mineralogy and Geochemistry* **69**, 61–120.

Riches, A. J. V. & Rogers, N. W. (2011). Mineralogical and geochemical constraints on the shallow origin, ancient veining, and multi-stage modification of the Lherz peridotite. *Geochimica et Cosmochimica Acta* **75**, 6160–6182.

Ritzwoller, M. H., Shapiro, N. M., Levshin, A. L. & Leahy, G. M. (2001). Crustal and upper mantle structure beneath Antarctica and surrounding oceans. *Journal of Geophysical Research* **106**, 30645–30670.

Rocchi, S., Bracciali, L., Di Vincenzo, G., Gemelli, M. & Ghezzo, C. (2011). Arc accretion to the early Paleozoic Antarctic margin of Gondwana in Victoria Land. *Gondwana Research* **19**, 594–607.

Rolland, Y., Galoyan, G., Bosch, D., Sosson, M., Corsini, M., Fornari, M. & Verati, C. (2009). Jurassic back-arc and Cretaceous hot-spot series in the Armenian ophiolites—Implications for the obduction process. *Lithos* **112**, 163–187.

Rudnick, R. L., McDonough, W. F. & Chappell, B. W. (1993). Carbonatite metasomatism in the northern Tanzanian mantle: petrographic and geochemical characteristics. *Earth and Planetary Science Letters* **114**, 463–475.

Rudnick, R. L., Barth, M., Horn, I. & McDonough, W. F. (2000). Rutile-bearing refractory eclogites: missing link between continents and depleted mantle. *Science* **287**, 278–281.

Scott, J. M., Turnbull, I. M., Auer, A. & Palin, J. M. (2013). The sub-Antarctic Antipodes Volcano: a $<0{\cdot}5$ Ma HIMU-like Surtseyan volcanic outpost on the edge of the Campbell Plateau, New Zealand. *New Zealand Journal of Geology and Geophysics* **56**, 134–153.

Scott, J. M., Waight, T. E., van der Meer, Q. H. A., Palin, J. M., Cooper, A. F. & Münker, C. (2014). Metasomatized ancient lithospheric mantle beneath the young Zealandia microcontinent and its role in HIMU-like intraplate magmatism. *Geochemistry, Geophysics, Geosystems* **15**, doi:10.1002/2014gc005300.

Shimizu, Y., Arai, S., Morishita, T. & Ishida, Y. (2008). Origin and significance of spinel–pyroxene symplectite in lherzolite xenoliths from Tallante, SE Spain. *Mineralogy and Petrology* **94**, 27–43.

Siena, F. & Coltorti, M. (1993). Thermobarometric evolution and metasomatic processes of upper mantle in different tectonic settings: Evidence from spinel peridotite xenoliths. *European Journal of Mineralogy* **5**, 1073–1090.

Sims, K. W. W., Blichert-Toft, J., Kyle, P. R., Pichat, S., Gauthier, P.-J., Blusztajn, J., Kelly, P., Ball, L. & Layne, G. (2008). A Sr,

Nd, Hf, and Pb isotope perspective on the genesis and long-term evolution of alkaline magmas from Erebus volcano, Antarctica. *Journal of Volcanology and Geothermal Research* **177**, 606–618.

Sinigoi, S., Comin-Chiaramonti, P., Demarchi, G. & Siena, F. (1983). Differentiation of partial melts in the mantle: Evidence from the Balmuccia peridotite, Italy. *Contributions to Mineralogy and Petrology* **82**, 351–359.

Smith, W. C. (1954). The volcanic rocks of the Ross archipelago. *Natural History Reports of the British Antarctic (Terra Nova) Expedition, 1910. Geology*. British Museum, pp. 1–107.

Stracke, A. (2012). Earth's heterogeneous mantle: A product of convection-driven interaction between crust and mantle. *Chemical Geology* **330–331**, 274–299.

Stump, E. (1995). *The Ross Orogen of the Transantarctic Mountains*. Cambridge University Press.

Sullivan, R. J. (2006). The geology and geochemistry of Seal Crater, Hurricane Ridge, Mount Morning, Antarctica. University of Otago, Dunedin, 138 pp.

Takahashi, N. (1992). Evidence for melt segregation towards fractures in the Horoman mantle peridotite complex. *Nature* **359**, 52–55.

Tang, Y.-J., Zhang, H.-F., Ying, J.-F. & Su, B.-X. (2013). Widespread refertilization of cratonic and circum-cratonic lithospheric mantle. *Earth-Science Reviews* **118**, 45–68.

Thomson, J. A. (1916). Report on the inclusions of the volcanic rocks of the Ross Archipelago (with Appendix by F. Cohen). In: *Report of the British Antarctic Expedition 1907–1909. Geology Report*. Heinemann, pp. 129–151.

Timm, C., Hoernle, K., van den Bogaard, P., Bindeman, I. & Weaver, S. (2009). Geochemical evolution of intraplate volcanism at Banks Peninsula, New Zealand: interaction between asthenospheric and lithospheric melts. *Journal of Petrology* **50**, 989–1023.

Timm, C., Hoernle, K., Werner, R., Hauff, F., van den Bogaard, P., White, J., Mortimer, N. & Garbe-Schönberg, D. (2010). Temporal and geochemical evolution of the Cenozoic intraplate volcanism of Zealandia. *Earth-Science Reviews* **98**, 38–64.

Upton, B. G. J., Downes, H., Kirstein, L. A., Bonadiman, C., Hill, P. G. & Ntaflos, T. (2011). The lithospheric mantle and lower crust–mantle relationships under Scotland: a xenolithic perspective. *Journal of the Geological Society, London* **168**, 873–886.

van Acken, D., Becker, H., Walker, R. J., McDonough, W. F., Wombacher, F., Ash, R. D. & Piccoli, P. M. (2010). Formation of pyroxenite layers in the Totalp ultramafic massif (Swiss Alps)—Insights from highly siderophile elements and Os isotopes. *Geochimica et Cosmochimica Acta* **74**, 661–683.

Voshage, H., Sinigoi, S., Mazzucchelli, M., Demarchi, G., Rivalenti, G. & Hofmann, A. W. (1988). Isotopic constraints on the origin of ultramafic and mafic dikes in the Balmuccia peridotite (Ivrea Zone). *Contributions to Mineralogy and Petrology* **100**, 261–267.

Walter, M. J. (1998). Melting of garnet peridotite and the origin of komatiite and depleted lithosphere. *Journal of Petrology* **39**, 29–60.

Walter, M. J. (2003). Melt extraction and compositional variability in mantle lithosphere. In: Holland, H. D. & Turekian, K. K. (eds.) *Treatise on Geochemistry*. Vol. 2, Pergamon, pp. 363–394.

Warner, R. D. & Wasilewski, P. J. (1995). Magnetic petrology of lower crust and upper mantle xenoliths from McMurdo Sound, Antarctica. *Tectonophysics* **249**, 69–92.

White, W. M. (2010). Oceanic island basalts and mantle plumes: the geochemical perspective. *Annual Review of Earth and Planetary Sciences* **38**, 133–160.

Wilshire, H. G. & Shervais, J. W. (1975). Al-augite and Cr-diopside ultramafic xenoliths in basaltic rocks from western United States. *Physics and Chemistry of the Earth* **9**, 257–272.

Wood, B. J. (1991). Oxygen barometry of spinel peridotites. In: Lindsley, D. H. (ed.) *Oxide Minerals: Petrologic and Magnetic Significance. Mineralogical Society of America, Reviews in Mineralogy* **25**, 417–432.

Wood, B. J., Bryndzia, L. T. & Johnson, K. E. (1990). Mantle oxidation state and its relationship to tectonic environment and fluid speciation. *Science* **248**, 337–345.

Woodhead, J. D. (1996). Extreme HIMU in an oceanic setting: the geochemistry of Mangaia Island (Polynesia), and temporal evolution of the Cook–Austral hotspot. *Journal of Volcanology and Geothermal Research* **72**, 1–19.

Woodland, A. B., Kornprobst, J. & Wood, B. J. (1992). Oxygen thermobarometry of orogenic lherzolite massifs. *Journal of Petrology* **33**, 203–230.

Woodland, A. B., Kornprobst, J. & Tabit, A. (2006). Ferric iron in orogenic lherzolite massifs and controls of oxygen fugacity in the upper mantle. *Lithos* **89**, 222–241.

Workman, R. K. & Hart, S. R. (2005). Major and trace element composition of the depleted MORB mantle (DMM). *Earth and Planetary Science Letters* **231**, 53–72.

Wörner, G. (1999). Lithospheric dynamics and mantle sources of alkaline magmatism of the Cenozoic West Antarctic Rift System. *Global and Planetary Change* **23**, 61–77.

Wörner, G. & Zipfel, J. (1996). A mantle *P–T* path for the Ross Sea Rift margin (Antarctica) derived from Ca-in-olivine zonation patterns in peridotites xenoliths of the Plio-Pleistocene Mt. Melbourne Volcanic Field. *Geologisches Jahrbuch* **B89**, 157–167.

Wörner, G., Viereck, L., Hertogen, J. & Niephaus, H. (1989). The Mt. Melbourne Volcanic Field (Victoria Land, Antarctica) II. Geochemistry and magma genesis. *Geologisches Jahrbuch* **E38**, 395–433.

Wysoczanski, R. E., Gamble, J. A., Kyle, P. R. & Thirlwall, M. F. (1995). The petrology of lower crustal xenoliths from the Executive Committee Range, Marie Byrd Land Volcanic Province, West Antarctica. *Lithos* **36**, 185–201.

Yaxley, G. M. & Green, D. H. (1998). Reactions between eclogite and peridotite: mantle refertilisation by subduction of oceanic crust. *Schweizerische Mineralogische und Petrographische Mitteilungen* **78**, 243–255.

Yaxley, G. M., Crawford, A. J. & Green, D. H. (1991). Evidence for carbonatite metasomatism in spinel peridotite xenoliths from western Victoria, Australia. *Earth and Planetary Science Letters* **107**, 305–317.

Zindler, A. & Hart, S. (1986). Chemical geodynamics. *Annual Review of Earth and Planetary Sciences* **14**, 493–571.

Zipfel, J. & Wörner, G. (1992). Four- and five-phase peridotites from a continental rift system: Evidence for upper mantle uplift and cooling at the Ross Sea margin (Antarctica). *Contributions to Mineralogy and Petrology* **111**, 24–36.